INFORMATION TO USERS

This manuscript has been reproduced from the microfilm master. UMI films the text directly from the original or copy submitted. Thus, some thesis and dissertation copies are in typewriter face, while others may be from any type of computer printer.

The quality of this reproduction is dependent upon the quality of the copy submitted. Broken or indistinct print, colored or poor quality illustrations and photographs, print bleedthrough, substandard margins, and improper alignment can adversely affect reproduction.

In the unlikely event that the author did not send UMI a complete manuscript and there are missing pages, these will be noted. Also, if unauthorized copyright material had to be removed, a note will indicate the deletion.

Oversize materials (e.g., maps, drawings, charts) are reproduced by sectioning the original, beginning at the upper left-hand corner and continuing from left to right in equal sections with small overlaps. Each original is also photographed in one exposure and is included in reduced form at the back of the book.

Photographs included in the original manuscript have been reproduced xerographically in this copy. Higher quality 6" x 9" black and white photographic prints are available for any photographs or illustrations appearing in this copy for an additional charge. Contact UMI directly to order.

UMI

A Bell & Howell Information Company
300 North Zeeb Road, Ann Arbor MI 48106-1346 USA
313/761-4700 800/521-0600

Thermally Driven Surface Winds in the Tropics

by

Zhaohua Wu

A dissertation submitted in partial fulfillment
of the requirements for the degree of

Doctor of Philosophy

University of Washington

1998

Approved by 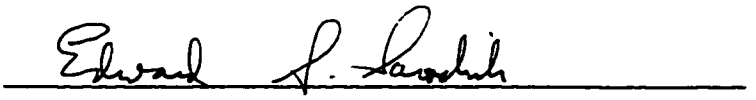

(Co-Chairperson of Supervisory Committee)

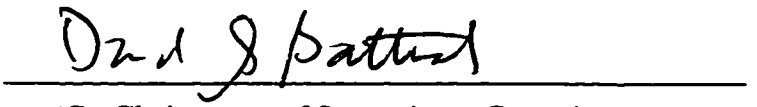

(Co-Chairperson of Supervisory Committee)

Program Authorized
to Offer Degree Atmospheric Sciences

Date November 20, 1998

Doctoral Dissertation

In presenting this dissertation in partial fulfillment of the requirements for the Doctoral degree at the University of Washington, I agree that the Library shall make its copies freely available for inspection. I further agree that extensive copying of this dissertation is allowable only for scholarly purposes, consistent with "fair use" as prescribed in the U.S. Copyright Law. Requests for copying or reproduction of this dissertation may be referred to University Microfilms, 1490 Eisenhower Place, P.O. Box 975, Ann Arbor, MI 48106, to whom the author has granted "the right to reproduce and sell (a) copies of the manuscript in microform and/or (b) printed copies of the manuscript made from microform."

Signature 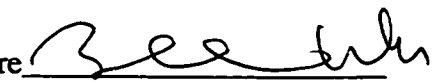

Date 12/15/98

University of Washington

Abstract

Thermally Driven Surface Winds in the Tropics

by Zhaohua Wu

Chairpersons of the Supervisory Committee: Professors E. S. Sarachik and D. S. Battisti
Department of Atmospheric Sciences

An integrated study is performed to examine the response of the atmosphere to a large-scale, elevated heat source in the tropics. Special emphasis is placed on the surface winds in response to the heating.

The vertical structure of the low-level atmospheric response to an elevated large-scale, low-frequency heat source in the tropics is first explored using the tidal approach. The projections of heating onto the meridional eigenfunctions on an equatorial beta-plane show that, at low frequencies, the forced response is mainly supported by the continuous modes with moderate large negative equivalent depth. The total response is vertically uniform below the heating in an atmosphere with only Newtonian cooling.

To further investigate the thermally forced response in the presence of both thermal and momentum damping, the linearized equations are decomposed into a set of shallow water equations using the vertical eigenfunctions in a vertically semi-infinite domain. The results show that the three-dimensional structure of the forced response is closely tied to the vertical structure of the heating, and the forced signals driven by deep heating propagate faster in the horizontal than those driven by shallow heating.

The zonal decay scale in a shallow water system is proportional to the inverse of the square root of the product of the Rayleigh friction rate and the Newtonian cooling rate. Hence, in both the Rayleigh-friction-dominant case and the Newtonian-cooling-dominant case, the solutions are essentially zonally uniform in a zonally cyclic domain. However, since the characteristic meridional scale, which is the equatorial radius of deformation multiplied by the fourth root of the Prandtl number, is very large for the Rayleigh-friction-dominant case, the forced response can extend far outside the heating latitudes. Contrast to that, in the Newtonian-cooling-dominant case, the characteristic meridional scale is very small and the forced response is confined to the heating latitudes.

The vertical structure of thermally driven circulation is significantly affected by the nature of dissipation. Newtonian cooling homogenizes the atmospheric motion in the vertical, and a strong vertically uniform wind is found below the heating. When Rayleigh friction dominates, the circulation driven by the heat source is confined to the layer where the heat source is located.

Finally, the numerical solutions from a primitive-equation model confirm the previous analytical results.

TABLE OF CONTENTS

Page

LIST OF FIGURES

Figure *Page*

Chapter 3

Chapter 4

Chapter 5

Chapter 6

Appendix B

LIST OF TABLES

Table *page*

ACKNOWLEDGEMENTS

It had been a mystery to me for seven years why my advisors admitted me, among other applicants, in the Spring of 1991. My transcripts didn't prove that I was one of the very top students, neither did My GRE and TOEFL scores. I later repeatedly asked my advisors about that and Prof. Sarachik finally gave me an answer after I took my defense: "Intuition." I am more puzzled than ever.

I always feel that I am lucky to spend seven years as a graduate student in the Department of Atmospheric Sciences, University of Washington. In these years of study, I faced the barriers of a foreign culture, a challenging discipline, and unexpected frustration. I owe a debt of gratitude to many persons who have helped me surmount those barriers.

First, thanks are due my advisors, Prof. Ed Sarachik and Prof. David Battisti, who have expressed more confidence in me than I expected. Ed has been providing me a great atmosphere to do research and have never pushed me hard. I have been extremely enjoying his style of guiding my research. My discussions with Ed about my research were often very short. However, when I digested his concise suggestions (often one sentence in length) after sacrificing numerous brain cells and hairs, I found myself standing at a much higher point to look forward. I am appreciative of David, who is enthusiastic in a broad spectrum of sciences and other fields. To me, David is a perfectionist: he spent an great amount of time in discussions with me and thorough proof-reading of my manuscripts. He is so energetic that sometimes I even thought he did never go to bed for sleeping.

Many thanks to Prof. Mike Wallace, Prof. Ka-Kit Tung, and Prof. Dennis Hartmann not only for their long-time serving on my committee, but also for their years of encouragement and support. These intangibles are easy to take for granted when one has them, but almost impossible to get along with when one does not have. Special thanks to Prof. Charlie Eriksen for his serving as a graduate school representative and Prof. Halstead Har-

rison for helping me out in scheduling of my Final Exam.

I express my special gratitude to Prof. Dennis Moore of NOAA/PMEL. I am happy that I had a chance to witness his great effort to obtain the spectral representation of the meridional structure equation. I should also acknowledge that some of my later results were inspired by discussions with him. In addition to these, I extremely enjoyed his telling anecdotes that happened in the tropical dynamical field in the last three decades.

I am thankful for Paul Goodman and Scot Johnson who proof-read my manuscripts. I am thankful for Bin Yu, Cheng-Ku Yu, Michela Biasutti who offered helpful advise at my practice talks. I am appreciate the friendship from everyone in JISAO. I am very thankful for Margaret-the-Black-Lab, our former lovely lunch-room friend, for her wondering around my office and giving me special fun. She must be at somewhere in heaven staring our lunch-room.

Many thank to my friends, Xinyou Lu, Xuri Yu, Weimin Wang, and Xinyu Wang. Without them, my life would have been lack of fun.

I am deeply obliged to my father Zaibang Wu, my brothers Kuancun Wu and Kuanshao Wu, and my sisters Yaxiu Wu and Yaya Wu, for their unconditional love and concern, and their constant encouragement and spiritual support from China.

Finally, I express my special thanks to my wife, Jinqi Zhang for her constant supporting me working in scientific field and regarding me as a good husband.

Dedication

I dedicate this dessertation

to my mother

Mrs. Chen, Ruixiang,

who passed away in the summer of 1981

Chapter 1
INTRODUCTION

A key component in the coupling between atmosphere and ocean is the surface winds. However, there is still no satisfactory theory for the origin of surface wind anomalies during ENSO. In general, there are two candidates to drive changes in the surface winds: 1) the pressure gradients induced by hydrostatic adjustment associated with changes in the sea surface temperature (SST) gradients, and 2) latent heating released in the tropical troposphere above the planetary boundary layer. The former directly drives the motion in the boundary layer (Lindzen and Nigam 1987) and may also drive the upper level circulation in the tropical and extratropical regions (Schneider and Lindzen 1977, Schneider 1977). The latter may produce low level convergence below the heating source and indirectly induce surface wind (e.g., Geisler 1981, Wang et al. 1996), which, of course, is related to the theory of the Conditional Instability of the Second Kind (CISK) (Charney and Eliassen 1964, Kuo 1965, Ooyama 1969). In recent years, however, some investigators have argued that the potential for the feedback between the convection and surface circulation may be possible without the need for instability.

The role of SST gradients in driving surface wind was examined by Lindzen and Nigam (1987), who proposed that SST anomalies produce sensible heat and evaporative fluxes which, in turn, produce virtual temperature anomalies. The virtual temperature anomalies are well-mixed into the boundary layer, producing surface pressure gradients that drive a surface circulation. In the Lindzen and Nigam model, the surface convergence is everywhere rapidly vented by convection in the presence of the strong thermal damping. In effect, the boundary layer anchors the location of convection to the underlying SST anomalies and the upper-level acts primarily as a reservoir for venting the lower atmosphere heat and perturbations.

Although the Lindzen and Nigam model simulates the surface wind anomalies in the tropical eastern Pacific with some success, the model is incapable of explaining the strong surface wind anomalies observed in some regions where the SST gradients are very small. Observational results from Deser and Wallace (1987), Deser and Wallace (1990), and Mitchell and Wallace (1996) showed that the July-November outgoing longwave radiation (OLR), a proxy for regions of persistent precipitation, and the surface wind are well correlated, especially in the western tropical Pacific where the sea surface temperature gradient is very small whereas the monthly climatological surface wind is strong (Rasmusson and Carpenter 1982).

An important contribution to the theory of the tropical circulations driven by large-scale cumulus convection is the work of Gill (1980). Gill argued that at low frequency the observed heating resulting from large-scale cumulus convection in the tropics could be grossly represented by one vertical mode, with the forced response taking the shape (or its derivative) of this mode as well. The horizontal structure of the analytical solutions of Gill are very similar to the numerical results from a two layer model designed by Webster (1972), and Webster also interpreted his external forcing as the simplification of large-scale cumulus heating. However, there are some fundamental problems with Gill's model, one of which is that by considering a single vertical mode, the heating is artificially brought right to the surface—the question of the propagation of signals from the bottom of the heat source to the surface therefore cannot be considered. To overcome these problems, Zebiak (1986) modified the Gill model's heating to include a CISK-like component based on the surface mass convergence, and noted that the convergence feedback term improved the amplitude and the pattern of the simulated surface wind response. Geisler (1981), using a linearized multi-layer atmospheric GCM, showed that a strong surface wind develops in response to a prescribed, elevated heat source. These studies imply that the large-scale cumulus heating may drive significant surface winds.

The current ideas of the impact of a large-scale elevated heat source on the surface circulation are mainly based on the propagation of energy away from the forcing by free waves in a viscous medium. The linear wave theory for the tropics can be found in the seminal paper by Lindzen (1967). Lindzen solved the three-dimensional linearized equations for an inviscid atmosphere on an equatorial beta plane in a vertically semi-infinite domain, and derived some of the propagation properties of the free and the forced waves. From Lindzen's formulae, it can easily be shown that the vertical group velocity for these equatorial trapped waves is proportional to the third power of the frequency for large-scale motion at low frequencies. Later, Cane and Sarachik (1993) presented a group velocity argument that suggested that under low frequency forcing and moderate dissipation, the vertical energy propagation is so slow that the signal is damped before reaching far from the heat source (the propagating distance is characterized by the product of the group velocity and the inverse of the damping rate).

This argument, however, is not very convincing. The solutions in Lindzen (1967) include only the contributions by the meridional eigenfunctions with discrete, positive equivalent depth[1]. Holl (1970) gave a detailed proof that the eigenfunctions (Hough functions) defined by Laplace's tidal equation over a sphere are complete. It was also shown that the complete set of Hough functions include the eigenfunctions of the first type with discrete positive equivalent depth, the eigenfunctions of the second type with discrete positive equivalent depth, and the eigenfunctions with discrete negative equivalent depth (Lindzen 1966, Kato 1966, Louguet-Higgins 1968). Although the eigenfunctions with negative equivalent depth are often trapped in the high latitudes at high frequencies, Flattery (1967) showed that, at low frequencies, these eigenfunctions with negative equivalent

1. We here follow the definition of the equivalent depth often used in the studies of tidal waves (e.g., Lindzen 1967). In these studies, the equivalent depth is actually the eigenvalue of a meridional eigen-mode, which is determined by the meridional structure equation of the meridional velocity and its corresponding boundary conditions. We will further clarify the concept of the equivalent depth in Chapter 4.

depth often have relatively significant amplitude in the tropical region, and some of them are even trapped in the tropics. By comparing the solutions in Lindzen (1967) on an equatorial beta-plane with the eigenfunctions of Laplace's tidal equations over a sphere, it is easy to conclude that, at low frequencies, the meridional eigenfunctions on an equatorial beta-plane correspond to the eigenfunctions of the first type of Laplace's tidal equations over a sphere. Since an equatorial beta-plane well approximates the spherical domain in the tropical region, it is reasonable to believe that the solutions on an equatorial beta-plane at low frequencies should also have significant contributions by the eigenfunctions with negative equivalent depth.

The purpose of this dissertation is to investigate the response of tropical atmosphere to a large-scale, elevated heat source. Special emphasis is placed on the surface winds driven by the elevated heating. To accomplish this goal, we will start with the earlier theory of thermally forced waves proposed by Lindzen (1967). By applying the principle of analytic continuation (Friedman 1956), we will confirm the completeness of the meridional eigenfunctions defined by the meridional eigenvalue-eigenfunction problem on an equatorial beta-plane. The method of spectral representation of a differential operator (Friedman 1956) will then be used to obtain all the meridional eigenfunctions on an equatorial beta-plane. The key question to answer in this part of the study is what is the vertical structure of the response of the atmosphere to the prescribed forcing by a large-scale low-frequency elevated heat source. Hence, the projection of heating onto different meridional eigenfunctions (modes) will be calculated. By obtaining the solutions to the non-homogeneous vertical structure equation in an inviscid atmosphere and in an atmosphere with only Newtonian cooling, we will present a linear wave theory of the thermally forced atmosphere in the tropics, emphasizing the surface winds driven by an elevated heat source. To our surprise, the structure of forced signals is highly dependent on the nature of the damping.

Although the above tidal approach provides some perspective on the vertical propagation of energy due to the forcing, the tidal approach *does* have serious problems at low frequencies, especially in the presence of both momentum damping and thermal damping. Therefore, we will tackle the problem of thermally driven tropical atmosphere by an elevated large-scale heat source using a shallow-water approach (see Chapter 4 for details). The complete set of the vertical eigenfunctions on a vertically semi-infinite atmosphere will be found. The solution to a prescribed steady heating is then found by projecting the heating onto the vertical eigenfunctions and using the solution to a steadily forced shallow water system (Gill 1980). The three dimensional structure of the forced circulation in the tropics will be examined. The different roles of momentum damping and thermal damping to the solutions will be examined in detail.

One important question is whether guidance developed from the linear theory is transferable to the real atmosphere. Since it is virtually impossible to clearly distinguish from observations the thermally forced circulation from the circulations driven by other types of forcing, we will carry out numerical experiments using a dry primitive-equation general circulation model (GCM) to test the results obtained using linear theory. We will also examine shortly in this dissertation whether the thermally forced circulation provides enough moisture convergence to maintain the prescribed heating.

The dissertation is arranged as follows. Chapter 2 provides a discussion of the tools by which the whole study is carried out: we lay out the governing linearized equations and discuss some of their mathematical and physical properties. Chapter 2 also contains a description of the dry primitive-equation model used in Chapters 4 to 6. Chapter 3 presents a linear wave theory of the thermally driven surface winds using the tidal approach. The problems associated with the tidal approach will be discussed in Chapter 4 and the shallow-water approach will be used to reveal the relationships between the verti-

cal structure of the heating and the three dimensional structure of the forced response. In Chapter 5, the different roles of Rayleigh friction and Newtonian cooling in a shallow water system will be investigated. Chapter 6 presents a three-dimensional view of the thermally forced tropical circulations, in the presence of different combinations of Rayleigh friction and Newtonian cooling using both simple analytical arguments and a primitive-equation model. The conclusions will be presented in Chapter 7[1].

1. Some of our results have already appeared in conference, proceedings and have been submitted for publication. (Wu et al. 1997a; Wu et al. 1997b; Wu et al. 1998a; Wu et al. 1998b).

Chapter 2

A LINEAR SYSTEM AND A PRIMITIVE-EQUATION ATMOSHERIC MODEL

2.1. Introduction

To accomplish this study, we will seek solutions to the linearized equations on an equatorial beta-plane, and evaluate the reliability of the linear solutions when nonlinear terms are present.

In the last four decades, many studies demonstrated that linear theories can offer fairly successful explanations for the large-scale phenomena in the tropics such as free waves, the waves excited by the tropical disturbance, diurnal tides, and the horizontal structures of the thermally driven atmospheric circulations (e.g., Matusno 1966; Lindzen 1967; Gill 1980; and etc.). There are two major advantages in using linear theory: physically, the linear theory provides clear dynamic pictures and direct reasoning using simple concepts such as Kelvin signal, Rossby signals, equatorial wave guides, etc.; mathematically, it is relatively easy to solve and the solutions can be clearly interpreted.

However, recent studies have shown the importance of nonlinearity to the momentum and vorticity balance in the tropics (e.g., Sardeshmukh and Held 1984, Battisti and Ovens 1995). For this reason, any solutions obtained using a linearized set of equations for the tropical atmosphere must be further scrutinized by evaluating, a posteriori, the importance of the neglected nonlinear terms.

In this chapter, we will discuss the tools by which we tackle the scientific problems mentioned in last chapter. In the next section, a linear model of thermally forced tropical atmosphere is outlined: the model equations, the energetics, and the uniqueness of the

solutions are derived and discussed. A dry primitive-equation model is introduced in section 2.3.

2.2. The Linearized Equations for the Tropical Atmosphere

The governing equations are the linearized equations for the tropical atmosphere on an equatorial beta-plane. Instead of using altitude above the surface as vertical ordinate, log pressure coordinates $z^* \equiv -H\ln(p/p_s)$ (Holton 1992) is used, where p_s is a standard reference pressure (usually taken to be 1000 mb) and H is a standard scale height, $H \equiv RT_s/g$, with T_s a globally averaged temperature, R gas constant for dry air, and g acceleration by gravity. The governing equations are

$$\frac{\partial u^*}{\partial t} - \beta y v^* = -\frac{\partial \Phi^*}{\partial x} - \alpha u^*, \tag{2.1a}$$

$$\frac{\partial v^*}{\partial t} + \beta y u^* = -\frac{\partial \Phi^*}{\partial y} - \alpha v^*, \tag{2.1b}$$

$$\frac{\partial u^*}{\partial x} + \frac{\partial v^*}{\partial y} + \frac{1}{\rho_0}\frac{\partial(\rho_0 w^*)}{\partial z^*} = 0, \tag{2.1c}$$

$$\frac{\partial}{\partial t}\frac{\partial \Phi^*}{\partial z^*} + N^2 w^* = \frac{\kappa J}{H} - \gamma\frac{\partial \Phi^*}{\partial z^*}. \tag{2.1d}$$

where u^* (v^*) is the eastward (northward) velocity; w^* the vertical velocity in log-pressure coordinates; Φ^* the geopotential; ρ_0 the basic density; κ the gas constant R divided by the heat capacity c_p; J the external heating rate per unit mass per unit time; N^2 the

buoyancy frequency squared; H is a scale height; $\beta = 2\Omega/a$, where Ω and a are the Earth's rotation rate and radius, respectively.

In the above model, the simplest forms of dissipation are included to study the forced response: Rayleigh friction and Newtonian cooling. Both the Rayleigh friction rate α and the Newtonian cooling rate γ are assumed constants.

Although consideration of a non-isothermal atmosphere is straightforward, we will assume an isothermal atmosphere with temperature T_s. The basic state is taken to be motionless and dependent only on z^*. Then, the basic density ρ_0 is

$$\rho_0(z^*) = \rho_0(0)e^{-z^*/H} . \tag{2.2}$$

Introducing the mass-weighted variables $u = \rho_0^{1/2}u^*$, $v = \rho_0^{1/2}v^*$, $w = \rho_0^{1/2}w^*$, and $\Phi = \rho_0^{1/2}\Phi^*$, substituting into equations (2.1a-d) and using equation (2.2) yields

$$\frac{\partial u}{\partial t} - \beta y v = -\frac{\partial \Phi}{\partial x} - \alpha u , \tag{2.3a}$$

$$\frac{\partial v}{\partial t} + \beta y u = -\frac{\partial \Phi}{\partial y} - \alpha v , \tag{2.3b}$$

$$\frac{\partial u}{\partial x} + \frac{\partial v}{\partial y} + \left(\frac{\partial}{\partial z} - \frac{1}{2H}\right)w = 0 , \tag{2.3c}$$

$$\frac{\partial}{\partial t}\left(\frac{\partial}{\partial z} + \frac{1}{2H}\right)\Phi + N^2 w = Q - \gamma\left(\frac{\partial}{\partial z} + \frac{1}{2H}\right)\Phi . \tag{2.3d}$$

where the superscript ' * ' of z^* has been omitted, and $Q = \rho_0^{1/2}\kappa J/H$.

We will consider two zonal domains in this dissertation: a zonally cyclic domain and a zonally infinite domain. In a zonally infinite domain, the boundary conditions are that the physical fields vanish at infinities. In the meridional direction, the boundary conditions are the "radiation conditions", which states that the forced signals are out going as $y \to \pm\infty$. (In Appendix B, we will show that the solutions satisfying these meridional boundary conditions also satisfy the boundary conditions that the physical fields vanish as $y \to \pm\infty$.) The boundary conditions in the vertical direction are

$$w = 0 \quad \text{at} \quad z = 0, \tag{2.4a}$$

and

$$\textit{either } w \to 0 \textit{ or outgoing radiation condition,} \quad \text{as } z \to \infty. \tag{2.4b}$$

Eliminating u and w from equations (2.3a-d), one obtains

$$(\beta^2 y^2 + \mathcal{A}^2)v = \left(\beta y \frac{\partial}{\partial x} - \mathcal{A}\frac{\partial}{\partial y}\right)\Phi, \tag{2.5}$$

and

$$\left(\beta y \frac{\partial}{\partial x} + \mathcal{A}\frac{\partial}{\partial y}\right)v + \frac{\mathcal{A}}{N^2}\left(\frac{\partial}{\partial z} - \frac{1}{2H}\right)Q = \left[\frac{\partial^2}{\partial x^2} + \frac{\mathcal{A}\Gamma}{N^2}\left(\frac{\partial^2}{\partial z^2} - \frac{1}{4H^2}\right)\right]\Phi, \tag{2.6}$$

where $\mathcal{A} = \partial/\partial t + \alpha$ and $\Gamma = \partial/\partial t + \gamma$.

Eliminating Φ in equations (2.5) and (2.6) yields the governing equation for the mass weighted meridional velocity v:

$$\frac{\mathcal{A}\Gamma}{N^2}\left(\frac{\partial^2}{\partial z^2}-\frac{1}{4H^2}\right)(\beta^2 y^2+\mathcal{A}^2)v+\left[\mathcal{A}^2\left(\frac{\partial^2}{\partial x^2}+\frac{\partial^2}{\partial y^2}\right)+\beta\mathcal{A}\frac{\partial}{\partial x}\right]v=$$

$$\left(\beta y\frac{\partial}{\partial x}-\mathcal{A}\frac{\partial}{\partial y}\right)\frac{\mathcal{A}}{N^2}\left(\frac{\partial}{\partial z}-\frac{1}{2H}\right)Q\,. \tag{2.7}$$

2.2.1. Energetics

Multiplying equation (2.3a) by u, equation (2.3b) by v, to equation (2.3c) by Φ, and equation (2.3d) by $\frac{1}{N^2}\left(\frac{\partial}{\partial z}+\frac{1}{2H}\right)\Phi$ yields

$$\frac{\partial}{\partial t}\left(\frac{1}{2}u^2\right)-\beta yuv=-u\frac{\partial\Phi}{\partial x}-\alpha u^2\,, \tag{2.8a}$$

$$\frac{\partial}{\partial t}\left(\frac{1}{2}v^2\right)+\beta yuv=-v\frac{\partial\Phi}{\partial y}-\alpha v^2\,, \tag{2.8b}$$

$$\Phi\frac{\partial u}{\partial x}+\Phi\frac{\partial v}{\partial y}+\Phi\left(\frac{\partial}{\partial z}-\frac{1}{2H}\right)w=0\,, \tag{2.8c}$$

$$\frac{\partial}{\partial t}\left[\frac{1}{2N^2}\left(\frac{\partial\Phi}{\partial z}+\frac{\Phi}{2H}\right)^2\right]+w\left(\frac{\partial}{\partial z}+\frac{1}{2H}\right)\Phi=\frac{Q}{N^2}\left(\frac{\partial}{\partial z}+\frac{1}{2H}\right)\Phi-\frac{\gamma}{N^2}\left(\frac{\partial\Phi}{\partial z}+\frac{\Phi}{2H}\right)^2\,. \tag{2.8d}$$

Combining equations (2.8a-d) leads to

$$\frac{\partial \mathcal{E}}{\partial t} = \mathcal{F} + C - \mathcal{D}, \tag{2.9}$$

where

$$\mathcal{E} = \iiint_{z\,y\,x}\left[\frac{1}{2}(u^2+v^2) + \frac{1}{2N^2}\left(\frac{\partial \Phi}{\partial z} + \frac{\Phi}{2H}\right)^2\right]dxdydz\,,$$

$$\mathcal{F} = \iiint_{z\,y\,x}\left[\frac{Q}{N^2}\left(\frac{\partial}{\partial z} + \frac{1}{2H}\right)\Phi\right]dxdydz\,,$$

$$C = -\iiint_{z\,y\,x}\left(\frac{\partial u\Phi}{\partial x} + \frac{\partial v\Phi}{\partial y} + \frac{\partial w\Phi}{\partial z}\right)dxdydz$$

and

$$\mathcal{D} = \iiint_{z\,y\,x}\left[\alpha(u^2+v^2) + \frac{\gamma}{N^2}\left(\frac{\partial \Phi}{\partial z} + \frac{\Phi}{2H}\right)^2\right]dxdydz\,.$$

The physical meaning of $\mathcal{E}$, $\mathcal{F}$, C and $\mathcal{D}$ are quite clear. $\mathcal{E}$ is the total energy, $\mathcal{F}$ is the energy provided by the heating, C is the net convergence of the energy, and $\mathcal{D}$ is the energy dissipated by the Rayleigh friction and Newtonian cooling. From equation (2.9), it can be inferred that when the atmosphere has only Newtonian cooling, there exist a free solution

$$\frac{\partial \Phi}{\partial z} + \frac{\Phi}{2H} = 0. \tag{2.10}$$

This solution corresponds to the Lamb mode.

2.2.2. The Uniqueness of the Solution

In the steady case, equation (2.7) becomes

$$\frac{\gamma}{N^2\alpha}\left(\frac{\partial^2}{\partial z^2}-\frac{1}{4H^2}\right)(\beta^2y^2+\alpha^2)v+\left[\left(\frac{\partial^2}{\partial x^2}+\frac{\partial^2}{\partial y^2}\right)+\frac{\beta}{\alpha}\frac{\partial}{\partial x}\right]v=$$

$$\left(\beta y\frac{\partial}{\partial x}-\alpha\frac{\partial}{\partial y}\right)\frac{1}{N^2\alpha}\left(\frac{\partial}{\partial z}-\frac{1}{2H}\right)Q\,. \tag{2.11}$$

The solution for equation (2.11) is unique, which can be shown as follows: Suppose v_1 and v_2 are two solutions satisfying equation (2.11) with the previously discussed boundary conditions, then $v' = v_1 - v_2$ satisfies:

$$\frac{\gamma}{N^2\alpha}\left(\frac{\partial^2}{\partial z^2}-\frac{1}{4H^2}\right)(\beta^2y^2+\alpha^2)v'+\left[\left(\frac{\partial^2}{\partial x^2}+\frac{\partial^2}{\partial y^2}\right)+\frac{\beta}{\alpha}\frac{\partial}{\partial x}\right]v'=0\,. \tag{2.12}$$

Multiplying v' on the both sides of equation (2.12) and integrating over the domain yields

$$\int_x\int_y\int_z\left[\frac{\gamma}{N^2\alpha}(\beta^2y^2+\alpha^2)\left(\frac{\partial v'}{\partial z}+\frac{v'}{2H}\right)^2+\left(\frac{\partial v'}{\partial x}\right)^2+\left(\frac{\partial v'}{\partial y}\right)^2\right]dxdydz = 0\,. \tag{2.13}$$

Since each term enclosed in the blanket in equation (2.13) is positive semidefinite, v' must be zero everywhere since v' vanishes at infinities in the meridional direction, i.e., v_2 and v_1 are identical.

2.3. A Dry Primitive-Equation Atmosphere Model

To verify the analytical results obtained from the above linear model and to assess the importance of nonlinearity we will perform numerical simulations using the dry primitive-equation model developed by Saravana and McWilliams (1995).

2.3.1. Model Description

The model is designed for mechanistic modeling of isolated phenomena, and for studying idealized planetary atmosphere rather than for performing "realistic" simulations of the Earth's climate. Some key features of the model are listed as following:

1. The numerical model is a three-dimensional primitive-equation model using pressure coordinates and assuming a flat lower boundary;

2. The vertical velocity at the surface and at the top of the model atmosphere is assumed to be zero. Therefore, the vertically integrated divergence over the whole atmosphere is identically zero, and divergent modes with barotropic vertical structure are excluded;

3. The model incorporates virtually no physical parameterizations of any kind. However, simple forms of scale-selective damping, Newtonian cooling, and Rayleigh friction are provided to facilitate mechanistic simulations;

4. The model equations are solved using spherical harmonics. The spectral transform is carried out all the latitudes simultaneously and triangular truncation is used. In the vertical, the centered-difference method is used to discretize the forcing term and the independent variables. The number of pressure levels and level thicknesses is flexible. In this study, the vertical resolution is set to be 60 layers of the equal thickness (in pressure). That high vertical resolution makes it possible to examine the low-level circulations driven by an elevated heat source. The horizontal resolution is T21, which corre-

sponds to 64 grid points zonally and 33 grid points meridionally. The leap-flog time-stepping scheme is used to integrate the model equations; therefore, the potential temperature is decomposed into a reference vertical profile and the deviations to it at any given location. A Robert time-filter (Robert 1966, Haltiner and Williams 1980) is also used to damp out the spurious computational mode.

2.3.2. Design of Model Experiment and the Model Parameter Setting

The most notable precipitation features in equatorial latitudes are the organized high rainfall regions that are characterized by strong deep convection (e.g., Peixoto and Oort 1992). Especially noteworthy is the very high values of precipitation over the equatorial regions in South America, Africa, and Indonesia and in the equatorial Pacific Ocean, implying substantial thermal forcing of the atmosphere in these regions. These high rainfall regions around the maritime continent region have very large horizontal scales. Observational studies (e.g., Frank and McBride 1989; Mapes and Houze 1995) show that the time-averaged heating associated with large-scale cumulus convection has a vertical structure that is approximately sinusoidal, starting from somewhere between 600 and 1000 meters above the surface and stopping at the tropopause; the maximum heating occurs in the middle to upper troposphere.

In this study, we prescribe the heating of the atmosphere and examine the three-dimensional response. The heating is assumed to be isolated with a three dimensional structure similar in spatial scale and amplitude to major centers of convection (e.g., Frank and McBride 1989; Mapes and Houze 1995). For simplicity, we assume that the heating can be expressed as a product of a horizontal structure $Q(x, y)$ and a vertical structure $P(z)$. Therefore, the numerical model results can be easily compared to the analytical solutions to the linear model previously discussed.

The reference state of the atmosphere is taken to be $300°K$ isothermal and static. Only Rayleigh friction and Newtonian cooling serve as the energy sinks. Since the analytic result suggests different roles of momentum and thermal damping for understanding the surface winds, we will examine the response using a variety of damping rates.

Chapter 3
THERMALLY DRIVEN SURFACE WINDS: A LINEAR WAVE THEORY

3.1. Introduction

Surface wind anomalies are the main determinant of sea surface temperature anomalies in the tropics. There have been two mechanisms suggested for generating such surface wind anomalies: 1) forcing by the hydrostatic pressure anomalies in the boundary layer induced by the SST anomalies themselves (Lindzen and Nigam 1987) and 2) thermal forcing from cloud base to the tropopause by anomalies of deep persistent precipitation. Because these mechanisms are highly interrelated (anomalous convergence of low level moisture leads to anomalies of persistent precipitation and therefore to anomalies of thermal forcing) it has not been clear how much of each mechanism contributes to the surface winds. Indeed, for some simple models of surface winds, in particular the Gill (1980) model, the two mechanisms are mathematically indistinguishable (Neelin 1989).

The way to cleanly separate the two mechanisms for generating surface winds is to consider each acting in the absence of the other—indeed this is what Lindzen and Nigam (1987) have done in examining the first mechanism. To examine the second mechanism, we consider the thermal forcing by a *specified* large-scale precipitation anomaly in the tropics in a horizontally homogeneous region with no SST anomalies. Any surface wind anomalies forced under these circumstances must have been thermally forced. In order to do the problem correctly, the propagation characteristics of the heat source anomaly from cloud base to the surface has to be considered and since the problem involves propagation, the results must be shown to exist independent of the existence of an artificial lid imposed at the top, since lids are known to induce artificial standing modes which can induce artificial results throughout a vertical column (Lindzen et al. 1968).

The thermal heat anomaly will be assumed to have a vertical structure similar to those diagnosed from tropical budget analyses, i.e. to begin at cloud base and end near the tropopause with a maximum somewhere in mid-troposphere. It will also be assumed to be large-scale (order 1000km) and change slowly, with assumed periods much longer than a day. It is recognized that propagation problems are significantly influenced by damping so that the effects of various types of damping must be considered.

There is a modest body of literature on this problem considered this way. The simple Gill model cited above is not suitable for looking at this problem because by considering a single vertical mode, the heating is artificially brought right to the surface—the question of the propagation of signals from the bottom of the heat source to the surface therefore cannot be considered. Schneider and Lindzen (1977) considered the zonally averaged (Hadley) circulation induced by a zonally averaged thermal heat source and found that the surface winds were basically determined by boundary layer convergence and were hardly modified by the thermal forcing. Indeed it was on the basis of just such arguments that Lindzen and Nigam decided to look at the boundary layer convergence in the absence of thermal forcing. Geisler (1981) considered a single large-scale steady heat source in a linearized atmospheric GCM and looked at the large-scale wind response. He included cumulus friction and full radiative damping and found that the heat source did indeed generate surface winds. He did not indicate whether or not the surface convergence of moisture generated by the heat source was large enough to sustain the heat source.

The questions therefore that need to be answered are: 1. Under what circumstances do thermal sources force surface winds in the absence of boundary forced convergence? 2. Under what circumstances is the anomalous moisture convergence forced by the thermal sources adequate to maintain the thermal source?

We will use a dry spectral primitive equation model and perform a numerical study of

these two questions in simplified situations using simplified damping mechanisms in later chapters. However, it will be the purpose of this chapter to give a linear wave theory for why thermal damping allows the forced response to reach the surface.

The analysis is performed *only* on an equatorial beta plane using separation of variable methods very similar to those of the classic paper of Lindzen (1967). As it will be discussed in the next section, the meridional eigenvalue-eigenfunction problem *does* define a complete set of meridional eigenfunctions. Hence, it is not necessary to use both the equatorial beta-plane and the mid-latitude beta-plane to match the complete solutions on a sphere as was done in Lindzen (1967).

A decomposition including thermal damping leads to equation (3.33) below. In the presence of the thermal damping, as the forcing becomes steady (the frequency approaches zero) the response from the base of the forcing to the surface becomes vertically uniform and the solutions in regions is determined by modes with non-zero equivalent depths. Thus the proof that thermal forcing can drive surface winds leads to a discussion of the behavior of the equivalent depths as the forcing frequency goes to zero. To our surprise, this discussion is not straightforward and leads to some continuum modes on the equatorial beta plane that, to our knowledge, have not previously been noted. In section 3.2, the equivalent depths and corresponding eigenfunctions are discussed, the completeness of the eigenfunctions are also discussed. Section 3.3 examines the projection problem in detail. Section 3.4 section describes how the major result of this chapter is obtained, that thermal damping allows the response to reach the surface. Section 3.5 discusses the implications of the main results obtained in this chapter and summarizes the chapter.

3.2. The Equivalent Depths and the Eigenfunctions

In an atmosphere free of dissipation, if the time-longitude dependence of the mass weighted meridional velocity v is assumed to be of the form $e^{i(kx-\omega t)}$, $\mathcal{A}$, Γ, and $\partial/\partial x$ in equation (2.7) are replaced by $-i\omega$, $-i\omega$, and ik, respectively. Then equation (2.7) becomes

$$\frac{1}{N^2}\left(\frac{\partial^2}{\partial z^2}-\frac{1}{4H^2}\right)(\beta^2 y^2-\omega^2)v+\left(-k^2-\beta\frac{k}{\omega}+\frac{\partial^2}{\partial y^2}\right)v=$$

$$\frac{-1}{N^2}\left(\frac{k}{\omega}\beta y+\frac{\partial}{\partial y}\right)\left(\frac{\partial}{\partial z}-\frac{1}{2H}\right)Q\,. \tag{3.1}$$

Now, for a given ω and k consider the set of functions $\{\Psi_{n,k,\omega}\}$ resulting from the following eigenvalue-eigenfunction equation

$$\frac{d^2\Psi_{n,k,\omega}}{dy^2}-\left(\beta\frac{k}{\omega}+k^2\right)\Psi_{n,k,\omega}-\frac{(\beta^2y^2-\omega^2)}{gh_{n,k,\omega}}\Psi_{n,k,\omega}=0\,. \tag{3.2}$$

Equation (3.2) has a similar form to the meridional structure equation which defines the free solutions in a shallow water system. However, the eigenvalue in equation (3.2) is no longer either the zonal wave number k or the wave frequency ω, but is $h_{n,k,\omega}$, which is historically called "the equivalent depth".

3.2.1. The Completeness and the Orthogonality of the Meridional Eigenfunctions

Since equation (3.2) is considered over a meridionally infinite domain, the boundary conditions associated with this equation are either the outgoing "radiation condition" or $\Psi_{n,k,\omega}\to 0$ as $y\to\pm\infty$. For the thermally forced atmosphere, the equivalent depth

$h_{n,k,\omega}$ is the eigenvalue and $(\beta^2 y^2 - \omega^2)$ is the corresponding weighting function. Although the weighting function $(\beta^2 y^2 - \omega^2)$ in equation (3.2) is not positive definite in the domain, the singularities at $y = \pm\omega/\beta$ are only apparent since the solutions to equation (3.2) for any given ω, k, and $h_{n,k,\omega}$ are differentiable at these singularities (see Appendix B).

Usually, the completeness of the eigenfunctions of an differential operator is discussed in a finite domain over which the eigenfunctions are all Lebesgue integrable. When the eigenfunctions are defined in an infinite domain, the principle of analytic continuation should be applied (cf. Friedman 1956). From Appendix B, we know that a negative equivalent depth renders a solution that is not Lebesgue square integrable in an interval containing infinity. In such a case, the differential operator in equation (3.2) is said to be in the *limit-point* case at infinity. The principle of analytic continuation requires that in such a case the corresponding Green's function is defined by implicitly requiring the Green's function to vanish for large values of y if $\lambda = -1/gh_n$ is complex and $Im\sqrt{\lambda} > 0$. For real values of λ, the Green's function is defined as the limit of the Green's function for complex values of λ as λ approaches the real axis. Hence, the differential operator in an infinite domain with a radiation boundary condition can be treated in the same way as when it is defined in a finite domain with regular (e.g., homogeneous, linear, outgoing waves, etc.) boundary conditions.

One can apply the theorem of the completeness of the eigenfunctions of an self-adjoint differential operator with only apparent singularities in the interior of an infinite domain in the same way as one can apply it in a finite domain. The completeness theorem that can be applied to equation (3.2) and its boundary conditions can be found in Holl

(1970). Hence, equation (3.2) and its boundary conditions result in a complete set of eigenfunctions for any given ω, k.

All the eigenvalues and eigenfunctions can be obtained by finding the Green's function and spectrally representing the differential operator (Friedman 1956). In Appendix A and Appendix B, such a method is used to obtain all the eigenvalues and eigenfunctions defined by equation (3.2) and its boundary conditions. The equivalent depths resulting from equation (3.2) and its boundary conditions consist of two types: an infinite number of discrete values of positive equivalent depths (the so called discrete spectrum) and a continuous spectrum of negative equivalent depth lying on the whole negative real axis. The eigenfunctions $\Psi_{n,k,\omega}$ of different n are mutually orthogonal under the principle of analytic continuation and their orthogonality can be expressed as

$$\int_{-\infty}^{\infty} (\beta^2 y^2 - \omega^2)\Psi_{n,k,\omega}\Psi_{m,k,\omega}dy = \begin{cases} 0 & m \neq n \\ C_{n,k,\omega} & m = n \end{cases}, \tag{3.3}$$

where $C_{n,k,\omega}$ is a function of ω, k, and n.

3.2.2. The Discrete Spectrum

The eigenfunctions corresponding to the discrete spectrum of positive equivalent depth are of the form

$$\Psi_{n,k,\omega} = \exp\left(-\frac{y^2}{2L_{n,k,\omega}^2}\right) H_n\left(\frac{y}{L_{n,k,\omega}}\right), \tag{3.4}$$

where $H_n(y/L_{n,k,\omega})$ is the Hermite Polynomial of order n (which is a non-negative integer), $L_{n,k,\omega} = \sqrt{\sqrt{gh_{n,k,\omega}}/\beta}$ is the characteristic meridional scale corresponding to equivalent depth $h_{n,k,\omega}$. The relationship between $h_{n,k,\omega}$ and n is

$$\left(\frac{\omega^2}{gh_{n,k,\omega}} - k^2 - \beta\frac{k}{\omega}\right)\frac{\sqrt{gh_{n,k,\omega}}}{\beta} = 2n+1\,. \tag{3.5}$$

For the eigenfunctions corresponding to the discrete spectrum, the $C_{n,k,\omega}$ in equation (3.3) can be expressed as

$$C_{n,k,\omega} = L_{n,k,\omega}2^{n-1}n!\sqrt{\pi}[(2n+1)\beta^2 L_{n,k,\omega}^2 - 2\omega^2]\,. \tag{3.6}$$

For the forced waves of low-frequency, i.e., $\omega \ll \Omega$, one can solve equation (3.5) and obtain the equivalent depth $h_{n,k,\omega}$ in terms of the known parameters for those eigenfunctions corresponding to the discrete spectrum:

$$(gh^{-}_{n,k,\omega})^{1/2} \approx \frac{\omega^2}{\beta(2n+1)} \tag{3.7a}$$

and

$$(gh^{+}_{n,k,\omega})^{1/2} \approx -(2n+1)\frac{\omega}{k}, \tag{3.7b}$$

which corresponds to the "-" sign solution and the "+" sign solution of equation (36) in Lindzen (1967), respectively. It should be noted that the eigenfunctions corresponding to the eigenvalues expressed by (3.7b) exist only for westward propagating waves.

At low frequencies, the equivalent depths given by equation (3.7a) are the counterpart of the equivalent depths of the first type of Laplace's solutions (Longuet-Higgins 1968); the equivalent depths given by equation (3.7b) correspond to the equivalent depths of the second type of Laplace's solution (see Figures 1–6 in Longuet-Higgins 1968). As frequencies go to zero, more and more beta-plane modes corresponding to equation (3.7b) are equatorially trapped and they become good approximations to the eigenfunctions on a sphere.

3.2.3. The Continuous Spectrum

The equivalent depths resulting from (3.2) and its boundary conditions are continuous when their value are negative. As the frequency goes to zero, equation (3.2) can be approximated by

$$\frac{d^2\Psi_{n,k,\omega}}{dy^2} + \left(-\beta\frac{k}{\omega} + \frac{\beta^2 y^2}{g\hat{h}_{n,k,\omega}}\right)\Psi_{n,k,\omega} = 0, \tag{3.8}$$

where $\hat{h}_{n,k,\omega} = -h_{n,k,\omega}$ is positive. Equation (3.8) can be transformed into the standard Weber equation that defines the Weber parabolic cylinder functions:

$$\frac{d^2\Psi_{n,k,\omega}}{d\eta^2} + \left(\frac{1}{4}\eta^2 - a\right)\Psi_{n,k,\omega} = 0, \tag{3.9}$$

where $\eta = y\sqrt{2\beta/\sqrt{g\hat{h}_{n,k,\omega}}}$, and $a = k\sqrt{g\hat{h}_{n,k,\omega}}/\omega$. Fig. 3.1 plots some solutions (Weber parabolic cylinder functions) for selected values of the parameter a. When $a \le 0$ (standing or westward propagating waves), the solutions are oscillatory and asymptotically decaying as η increases. When $a > 0$ (eastward propagating waves), the

solutions exponentially increase before they reach their turning points ($\eta = \pm 2\sqrt{a}$) and become oscillatory and asymptotically decaying afterward. For large positive a, the symmetric and antisymmetric solutions are almost identical everywhere and trivial for small η. When $|\eta| \gg |a|$, all the solutions have their asymptotic envelopes that are proportional to $\sqrt{1/|\eta|}$. More details about the solutions to equation (3.9) and their asymptotic properties can be found in Abramowitz and Stegun (1965).

The modes of negative equivalent depths are not artificially induced by approximating a spherical domain with an equatorial beta-plane. From Flattery (1967), we know that at low frequencies ($\omega \ll \Omega$), the spherical modes with negative equivalent depth are not trapped in the high latitudes, rather, they have very significant components in the tropics.

It should be pointed out that the discrete modes with large $h_{n,k,\omega}$ and the continuous modes with negative equivalent depth are not only mathematically necessary to form a complete set of eigenfunctions on an equatorial beta-plane but also physically account for the forcing energy leaked to high latitudes in an atmosphere free of dissipation.

3.3. Projection of Forcing onto the Meridional Eigenfunctions

Since $\{\Psi_{n,k,\omega}\}$ constitute a complete set, it can be used to expand v and the forcing term as the following:

$$v = \sum_{n} V_{n,k,\omega}(z)\Psi_{n,k,\omega}(y), \tag{3.10}$$

and

$$\left(\frac{k}{\omega}\beta y+\frac{\partial}{\partial y}\right)\frac{1}{N^2}\left(\frac{\partial}{\partial z}-\frac{1}{2H}\right)Q = (\beta^2y^2-\omega^2)\sum_n S_{n,k,\omega}(z)\Psi_{n,k,\omega}(y) \quad , \qquad (3.11)$$

where the summation represents a sum over the discrete spectrum and integration over the continuum.

To investigate how the overall forced solution behaves, it is important to know the projection of the forcing onto each meridional eigenfunctions. For simplicity, we now assume that the external forcing has the form

$$\tilde{Q} = \frac{\left(\frac{k}{\omega}\beta y+\frac{\partial}{\partial y}\right)\left(\frac{\partial}{\partial z}-\frac{1}{2H}\right)\frac{Q}{N^2}}{\beta^2y^2-\omega^2} \approx q_m(z)\chi_m(y)\,, \qquad (3.12)$$

where $q_m(z)$ is the vertical structure of the heating, and $\chi_m(y)$ is defined as

$$\chi_m(y) = \exp\left(-\frac{y^2}{2L_f^2}\right)H_m\left(\frac{y}{L_f}\right). \qquad (3.13)$$

$\chi_m(y)$ is the parabolic cylinder function that satisfies

$$\frac{d^2\chi_m}{dy^2}+\left[\frac{2m+1}{L_f^2}-\frac{y^2}{L_f^4}\right]\chi_m = 0\,. \qquad (3.14)$$

The general properties of the parabolic cylinder function $\chi_m(y)$ can be found in Abramowitz and Stegun (1964). The set $\{\chi_m(y)\}$ is complete and is used to expand any meridionally localized function, and L_f is the characteristic meridional scale of the exter-

nal forcing. If $\tilde{Q}$ meridionally has the shape of a Gaussian distribution (i.e., $m = 0$ in equation (3.13)), $\sqrt{2}L_f$ is the e-folding scale. For the forced problem we are dealing with, the shape of external forcing is prescribed so that L_f is assumed a known constant.

3.3.1. Projection of Forcing onto the Discrete Modes

For the discrete modes, the eigenvalue-eigenfunction equation (3.2) can be written as

$$\frac{d^2\Psi_{n,k,\omega}}{dy^2} + \left[\frac{2n+1}{L^2_{n,k,\omega}} - \frac{y^2}{L^4_{n,k,\omega}}\right]\Psi_{n,k,\omega} = 0, \tag{3.15}$$

where $L_{n,k,\omega} = \sqrt{\sqrt{gh_{n,k,\omega}}/\beta}$ for any positive $h_{n,k,\omega}$.

We rewrite

$$\tilde{Q} = \sum_n S_{n,k,\omega}(z)\Psi_{n,k,\omega}(y), \tag{3.16}$$

where the summation represents a sum over the discrete spectrum and integration over the continuum.

Multiplying equation (3.15) by χ_m and multiplying equation (3.14) by $\Psi_{n,k,\omega}$ yields

$$\chi_m\frac{d^2\Psi_{n,k,\omega}}{dy^2} + \left[\frac{2n+1}{L^2_{n,k,\omega}} - \frac{y^2}{L^4_{n,k,\omega}}\right]\Psi_{n,k,\omega}\chi_m = 0, \tag{3.17}$$

and

$$\Psi_{n,k,\omega}\frac{d^2\chi_m}{dy^2}+\left[\frac{2m+1}{L_f^2}-\frac{y^2}{L_f^4}\right]\chi_m\Psi_{n,k,\omega}=0, \tag{3.18}$$

respectively.

Subtracting equation (3.18) from equation (3.17) and using the relationship

$$\int_{-\infty}^{\infty}\left[\frac{d}{dy}\left(\Psi_{n,k,\omega}\frac{d\chi_m}{dy}\right)-\frac{d}{dy}\left(\chi_m\frac{d\Psi_{n,k,\omega}}{dy}\right)\right]dy=0 \tag{3.19}$$

yields

$$\int_{-\infty}^{\infty}y^2\Psi_{n,k,\omega}\chi_m dy=b\int_{-\infty}^{\infty}\Psi_{n,k,\omega}\chi_m dy, \tag{3.20}$$

where

$$b=\frac{\dfrac{2m+1}{L_f^2}-\dfrac{2n+1}{L_{n,k,\omega}^2}}{\dfrac{1}{L_f^4}-\dfrac{1}{L_{n,k,\omega}^4}}. \tag{3.21}$$

Multiplying equation (3.20) by $\beta^2 q_m(z)$ and using equation (3.12) yields

$$\int_{-\infty}^{\infty}\beta^2 y^2\Psi_{n,k,\omega}\tilde{Q}dy=\beta^2 b\int_{-\infty}^{\infty}\Psi_{n,k,\omega}\tilde{Q}dy. \tag{3.22}$$

Subtracting $\omega^2\int_{-\infty}^{\infty}\Psi_{n,k,\omega}\tilde{Q}dy$ from both sides of equation (3.22) and using equation (3.16), we find

$$\int_{-\infty}^{\infty}(\beta^2 y^2-\omega^2)\Psi_{n,k,\omega}\left(\sum_n S_{n,k,\omega}(z)\Psi_{n,k,\omega}(y)\right)dy = (\beta^2 b-\omega^2)\int_{-\infty}^{\infty}\Psi_{n,k,\omega}\tilde{Q}dy\,. \tag{3.23}$$

Finally, using the orthogonality relationship of equation (3.3) for $\Psi_{n,k,\omega}(y)$, equation (3.23) yields the projection of the forcing onto the discrete modes:

$$S_{n,k,\omega}(z) = \frac{(\beta^2 b-\omega^2)q_m(z)}{C_{n,k,\omega}}\int_{-\infty}^{\infty}\Psi_{n,k,\omega}(y)\chi_m(y)dy\,. \tag{3.24}$$

a. The Minus Sign Discrete Modes

For a given external forcing, b in equation (3.20) is a function of wave frequency ω, zonal wave number k, and order n. For large-scale, low-frequency forced waves, one obtains $L^-_{n,k,\omega}$ as:

$$(L^-_{n,k,\omega})^2 = \frac{\sqrt{gh^-_{n,k,\omega}}}{\beta} = \frac{\omega^2}{(2n+1)\beta^2}. \tag{3.25}$$

Equation (3.25) shows that $L^-_{n,k,\omega}\to 0$ as $\omega\to 0$. So, we have $L^-_{n,k,\omega} \ll L_f$. When m is not extremely large compared to n,

$$b \approx (2n+1)(L^-_{n,k,\omega})^2 = \frac{\omega^2}{\beta^2}. \tag{3.26}$$

Substitution of equation (3.26) into equation (3.24) gives

$$S^{-}_{n,k,\omega}(z) \to 0. \tag{3.27}$$

Equation (3.27) states that for a prescribed low-frequency external forcing, the projection onto the minus sign discrete modes approaches zero.

To find the hidden physics in equation (3.27), we examine the turning point $y^{-}_{d,n,k,\omega}$ for the mode $\Psi^{-}_{n,k,\omega}$:

$$\left(y^{-}_{d,n,k,\omega}\right)^2 = (2n+1)\frac{\sqrt{gh^{-}_{n,k,\omega}}}{\beta}. \tag{3.28}$$

$\Psi^{-}_{n,k,\omega}$ decays for $|y| > y^{-}_{d,n,k,\omega}$, so $\left|y^{-}_{d,n,k,\omega}\right|$ can be regarded as the poleward extent of the mode $\Psi^{-}_{n,k,\omega}$. For these minus sign discrete solutions, $\left(y^{-}_{d,n,k,\omega}\right)^2 = \omega^2/\beta^2$. Hence, $y^{-}_{d,n,k,\omega}$ is very small and is independent of n; and these modes by themselves can not account for any response to the external forcing outside the turning points. As $\omega \to 0$, the turning points approach the equator and these minus sign solutions are clearly more and more incomplete.

b. The Plus Sign Discrete Modes

As the frequency goes to zero, more and more eigenfunctions with positive equivalent depth corresponding to equation (3.7b) on an equatorial beta-plane have their counterparts on the spherical Earth. Hence, the projections of the external forcing onto these modes must be considered. The turning points for these modes can be expressed as $y^{+}_{d,n,k,\omega} = (2n+1)\sqrt{\omega/(-\beta k)}$. So, at the low frequency end, when n is not very large,

$y^{+}_{d,n,k,\omega}$ is not very large, and the corresponding eigenfunction $\Psi^{+}_{n,k,\omega}$ is still equatorially trapped. However, these modes can not contribute significantly to the response to a specified external forcing. When n is large and y is limited, $\Psi^{+}_{n,k,\omega}$ can be approximated by

$$\Psi^{+}_{n,k,\omega} \approx D_n \cdot \cos\left(\sqrt{2n+1}\frac{y}{L^{+}_{n,k,\omega}} - \frac{n\pi}{2}\right) = D_n \cdot \cos\left(\sqrt{-\frac{\beta k}{\omega}}y - \frac{n\pi}{2}\right), \qquad (3.29)$$

where $D_n = 2^{(n+1)/2}(n/e)^{n/2}$, and $L^{+}_{n,k,\omega} = \sqrt{(2n+1)\omega/(-\beta k)}$. By considering equations (3.6) and (3.24), one can expect that the projections of external forcing onto these modes go to zero very fast as n increases when n is large since the $\Psi^{+}_{n,k,\omega}$ for different n have the same sinusoidal shape in the tropics. Hence, only $\Psi^{+}_{n,k,\omega}$ of relatively small n contribute to the response to the external forcing. Since the distance of consecutive zero's of $\Psi^{+}_{n,k,\omega}$ is independent of n for large n, we can also infer that the plus sign modes with discrete positive eigenvalues do not resolve scales smaller than $\pi\sqrt{\omega/(-\beta k)}$. Hence the discrete modes can never constitute a complete set.

The dependence of the projections $P_{n,k,\omega}$ of the external forcing onto the modes of discrete positive equivalent depths as a function of the characteristic scale of the external forcing L_f is shown in Fig. 3.2, where $P_{n,k,\omega} = S_{n,k,\omega}/q_m(z)$. The heat source $\bar{Q}$ has a Gaussian shape with Gaussian scale L_f and is of unit amplitude. It is clear that for a large range of the characteristic meridional scale of the external forcing L_f, only the $n = 0$ modes are significant. When L_f is large enough, however, the contributions from the plus

sign discrete modes with larger characteristic meridional scale $L_{n,k,\omega}$ (larger n) become non-trivial. This is especially clear in panel (d) of Fig. 3.2, where the ratio $P^{+}_{2,k,\omega}/P^{+}_{0,k,\omega}$ increases as the characteristic scale of the external forcing L_f becomes larger. When L_f is very small, we see that the projections of the external forcing onto the minus sign discrete modes increase as L_f decreases. (The discontinuity at L_f = 450 km in panel c is due to the change of sign of $P^{-}_{0,k,\omega}$ at that point.)

3.3.2. Projection of Forcing onto the Continuous Spectrum of Modes with Negative Equivalent Depth

The incompleteness of the discrete modes is demonstrated in Fig. 3.3 where a Gaussian profile is separated into two parts: 1) the part accounted for by an infinite set of the discrete modes, and 2) the part accounted for by the continuous modes (which is the difference between the Gaussian profile and the part accounted for by the discrete modes). It is obvious that the continuous eigenfunctions of negative equivalent depth must be included to form a complete set that can be used to decompose the heating and the variables. But so far it is almost impossible to analytically calculate the projections of a heat source onto these eigenfunctions of negative equivalent depth since the solutions to equation (3.9) can be expressed only as infinite power series or complex integrals and these solutions are not Lebesgue square integrable in the infinite domain. Thus, instead of a quantitative calculation, a qualitative discussion of the projections onto those modes is presented by considering the properties of the asymptotic solutions.

At a given frequency, $\Psi_{n,k,\omega}$ is an oscillatory function of y for westward propagating waves (negative k). When the absolute value of the equivalent depth is very small, a is

very small, and the absolute value of η is very large for any non-zero y. Since the solution of $\Psi_{n,k,\omega}$ in such a case asymptotically decays as $\sqrt{1/|\eta|}$, we can infer that $\Psi_{n,k,\omega}$ is equatorially trapped when $\hat{h}_{n,k,\omega}$ is small. Such a eigenfunction can hardly account for the external forcing with a large characteristic meridional scale L_f. When the absolute value of the equivalent depth is very large, from equation (3.8) we can infer that $\Psi_{n,k,\omega}$ is asymptotically proportional to $e^{i\sqrt{-k\beta/\omega}y}$ for any y that is not very large when $\hat{h}_{n,k,\omega}$ is very large, and therefore, $\Psi_{n,k,\omega}$ is too wavy at very low frequency to account for the external forcing. Hence, the eigenfunctions with negative equivalent depths that carry the significant information from the forcing must have moderate value of $\hat{h}_{n,k,\omega}$. A similar argument holds for the eastward propagating waves.

3.4. Solutions to the Vertical Structure Equation

Substituting equations (3.10), (3.11), and (3.2) into equation (3.1), one obtains

$$\left(\frac{d^2}{dz^2} - \frac{1}{4H^2} + \frac{N^2}{g\hat{h}_{n,k,\omega}}\right) V_{n,k,\omega}(z) = -S_{n,k,\omega}(z) . \tag{3.30}$$

Equation (3.30) is the so-called vertical structure equation.

For the discrete spectrum, the eigenfunctions that are the valid approximations to the spherical modes generally satisfy $0 < \hat{h}_{n,k,\omega} < H$. Hence, the signals excited by the external forcing propagate vertically with vertical wave number m which is approximated by

$$m^2 \approx \frac{\kappa}{Hh_{n,k,\omega}}. \tag{3.31}$$

The modes corresponding to the continuous spectrum have negative equivalent depths; and thus, they decay away from the heating level. The solutions to equation (3.30) are vertically evanescent for these modes.

In the presence of dissipation, how the signals propagate depends on the form of the damping. It is often stated that the distance a forced signal can propagate is characterized by the product of the group velocity of the free wave and damping time scale. At low frequencies, the vertical group velocities for the modes defined by equation (3.7a) and (3.7b) are

$$\left(\frac{d\omega}{dm}\right)^- = C_{gz}^- = \sqrt{\frac{H}{\kappa g}}\frac{\omega^3}{2(2n+1)\beta}, \tag{3.32a}$$

and

$$\left(\frac{d\omega}{dm}\right)^+ = C_{gz}^+ = \sqrt{\frac{H}{\kappa g}}\frac{(2n+1)\omega^2}{k}, \tag{3.32b}$$

respectively. The vertical group velocity of zonal wavenumber one waves are calculated for an isothermal atmosphere with scale height 8 kilometers and presented in Fig. 3.4. It is clear that for the waves of period about 40 days, the plus sign discrete modes can propagate a few hundred meters per day, while the minus sign discrete modes propagate less than 1 meter per day. At high frequencies, the vertical group velocities of all the modes with discrete positive equivalent depth are large. However, at low frequencies the large-scale heat source does not project significantly onto the low order plus sign discrete modes. This implies that the continuous modes with negative equivalent depths (which

account for the most of the vertically standing response) may be the key to explain the significant response below the forcing level.

To what extent the above argument can approximate the dissipative system is difficult to determine. Since the equations are analytically intractable if both thermal damping and momentum damping are added, here we deal with the simplest case in which only Newtonian cooling is included as the only damping. Lindzen (1968) first considered a case in which Newtonian cooling is inversely proportional to the density of the atmosphere in his study of the vertically propagating waves. His results showed that at very high level (where Newtonian cooling rate is very large) the amplitude of the horizontal divergence is vertically uniform. When we added a Newtonian cooling term to the thermodynamic equation in Lindzen (1967), and use the same method that he used to separate the equations, the eigenvalue-eigenfunction equation is identical to equation (3.2) and the vertical structure equation becomes

$$\frac{d^2 V_{n,k,\omega}}{dz^2} + \left(\frac{N^2 \omega}{(\omega - i\gamma) g h_{n,k,\omega}} - \frac{1}{4H^2} \right) V_{n,k,\omega} = -S_{n,k,\omega}, \tag{3.33}$$

where, $i = \sqrt{-1}$, and γ is the Newtonian cooling rate. When $\omega \to 0$, we know that the projection of the forcing goes mainly to the modes whose $h_{n,k,\omega}$ are not zero. Hence, when thermal damping time scale is around two weeks or shorter, we have $|i\gamma| \gg \omega$, and then we obtain

$$\left| \frac{1}{4H^2} \right| \gg \left| \frac{\omega \kappa}{(\omega - i\gamma) H h_{n,k,\omega}} \right| \tag{3.34}$$

for the waves that are excited by the external forcing. Then, the vertical equation (3.33)

simplifies to

$$\frac{d^2 V_{n,k,\omega}}{dz^2} - \frac{V_{n,k,\omega}}{4H^2} = -\frac{\kappa}{H} S_{n,k,\omega}. \tag{3.35}$$

Equation (3.35) states that the response to the forcing decays exponentially in the vertical outside of the heating with a decay scale $1/2H$. Recalling that the variable $V_{n,k,\omega}$ has already been mass-weighted, we conclude that the meridional wind itself must be vertically uniform above and below the heating—in particular, under the convective heating region.

3.5. Discussion and Summary

In this chapter, we discussed both the latitudinal structure equation and the vertical structure equation of the linear inviscid tropical atmosphere. Our emphasis is on the low level responses to a large-scale low-frequency elevated heat source in the tropics.

By analyzing the projections of the external forcing onto different modes, we find that all the eigenfunctions corresponding to equation (3.7a) shrink to the equator as frequency goes to zero. Hence, the modes of discrete positive equivalent depth are in general not capable of describing the bulk solution of the atmosphere that is forced by a prescribed large meridional scale.

Among the plus sign modes of discrete positive equivalent depth, modes of large n may not be applied to the spherical domain. It can be shown, however, that the projections of an external forcing onto large n modes are vanishingly small. Hence, the plus sign discrete modes with large n do not contribute to the solution and we need not worry that the

equatorial beta-plane modes are not appropriate to the spherical Earth. Practically, how many modes of relatively small n should be retained is determined by both the frequency and the characteristic meridional scale of the external forcing.

The complete solution to a meridionally localized heat source in the tropics includes the modes from a continuous spectrum of negative equivalent depths that have not previously been discussed in the literatures. As the frequencies go to zero, the external forcing projects mainly onto these large negative equivalent depth modes. Physically, these modes also account for the linear response at higher latitudes to the imposed tropical heating.

The application of the group velocity argument to a dissipative system is questionable. In general, it is necessary to examine the details of the dissipating processes. It is clear from section 3.4, however, that adding thermal damping fundamentally changes the vertical structure of the response. Nonetheless, from the vertical structure equation, we can infer that a significant surface wind can be driven by an elevated, large-scale diabatic heating if thermal damping is operating.

To more completely assess the roles of Rayleigh friction and Newtonian cooling in producing surface wind, we have performed numerical experiments with a dry global spectral atmosphere model. Consistent with the argument in section 3.4, we find that in the presence of Newtonian cooling, the solutions are characterized by winds that extend vertically away from the heating in a uniform fashion. Hence, the Newtonian cooling does allow for a significant surface wind response to a vertically elevated heating. In contrast, when Rayleigh friction dominates, the circulation driven by the elevated heat source is vertically confined to the layer where the heat sources is located. The detailed description of this modeling study will be presented in Chapter 6.

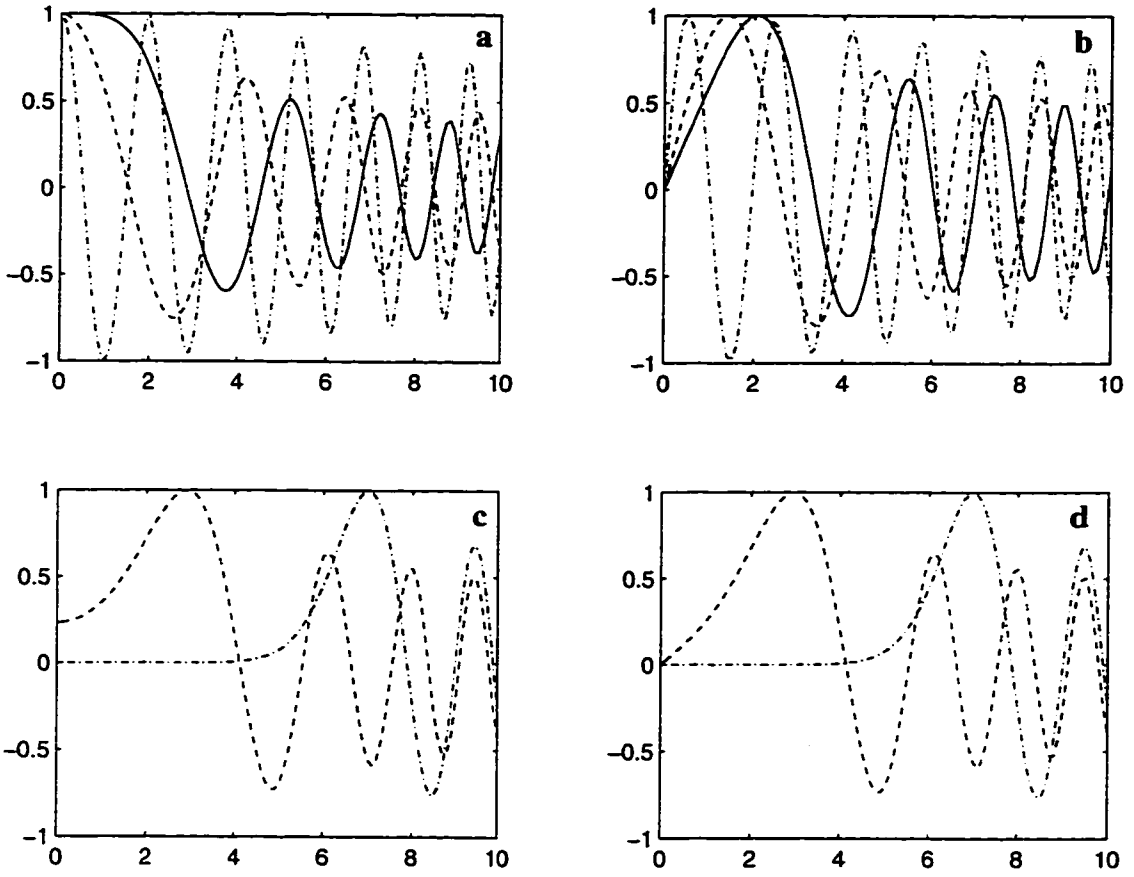

Figure 3.1: The normalized Weber parabolic cylinder functions defined by equation (3.9) for selected values of the parameter a. The meridionally symmetric Weber parabolic cylinder functions are plotted in panels *a* and *c*, and the meridionally asymmetric Weber parabolic cylinder functions are plotted in panel *b* and *d*. The horizontal axis represents the value of η. In panels *a* and *b*, solid line is for a=0; dashed line is for a=-1.0; and dash-dotted line is for a=-10.0. In panels *c* and *d*, dashed line is for a=1.0; and dash-dotted line is for a=10.0.

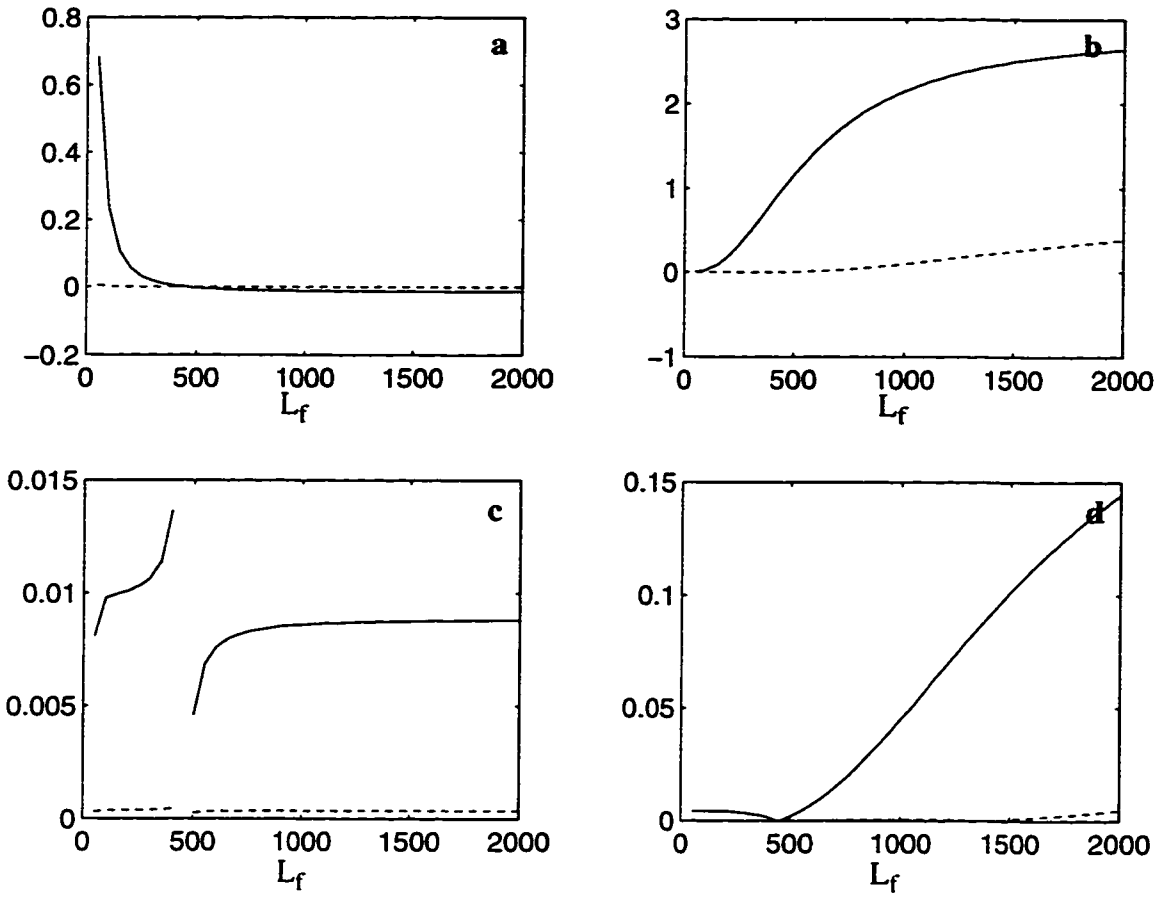

Figure 3.2. The relationship between the characteristic meridional scale of external forcing L_f and the projections of the external forcing onto the discrete modes of zonal wave number one and 100-day period. (a) The projection coefficients $P^-_{0,k,\omega}$ (solid line) and $P^-_{2,k,\omega}$ (dashed line); (b) The projection coefficients $P^+_{0,k,\omega}$ (solid line) and $P^+_{2,k,\omega}$ (dashed line); (c) The ratios $\left|P^-_{2,k,\omega}/P^-_{0,k,\omega}\right|$ (solid line) and $\left|P^-_{4,k,\omega}/P^-_{0,k,\omega}\right|$ (dashed line); (d) The ratios $\left|P^+_{2,k,\omega}/P^+_{0,k,\omega}\right|$ (solid line) and $\left|P^+_{4,k,\omega}/P^+_{0,k,\omega}\right|$ (dashed line). In each panel, the horizontal axis represents the characteristic meridional scale of external forcing L_f in kilometers.

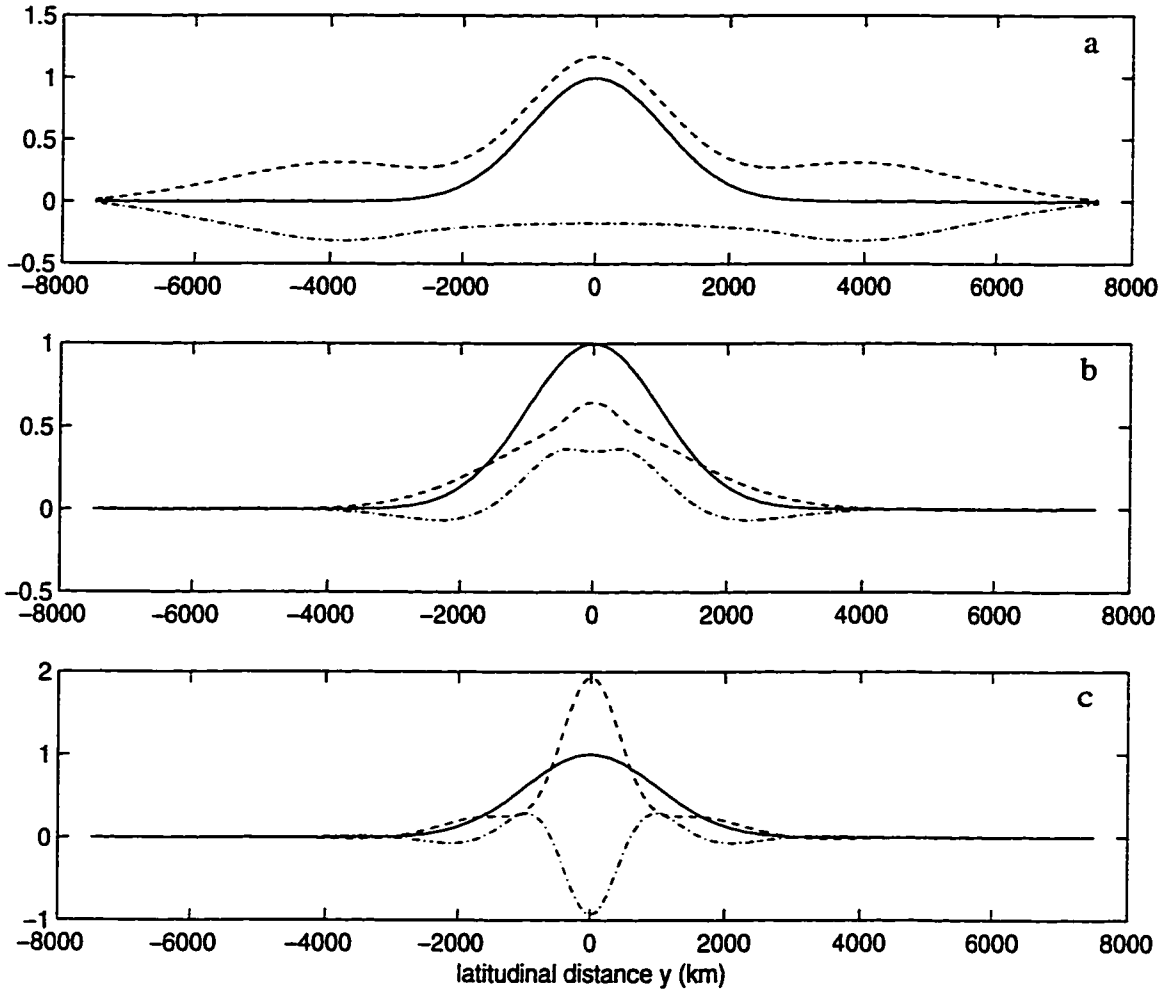

Figure 3.3: The projection of a Gaussian profile (with scale 1000 km) onto the meridional eigenfunctions. Zonal wave number one is used in the meridional structure equation. Panels *a*, *b*, and *c* correspond to waves of 1-day, 10-day, and 100-day period, respectively. In each panel, the solid line is the Gaussian profile, the dashed line is the part of the Gaussian profile that is accounted for by all the discrete modes. The difference between these curves is shown by the dash-dotted line, and represents the part must be resolved by the continuous modes.

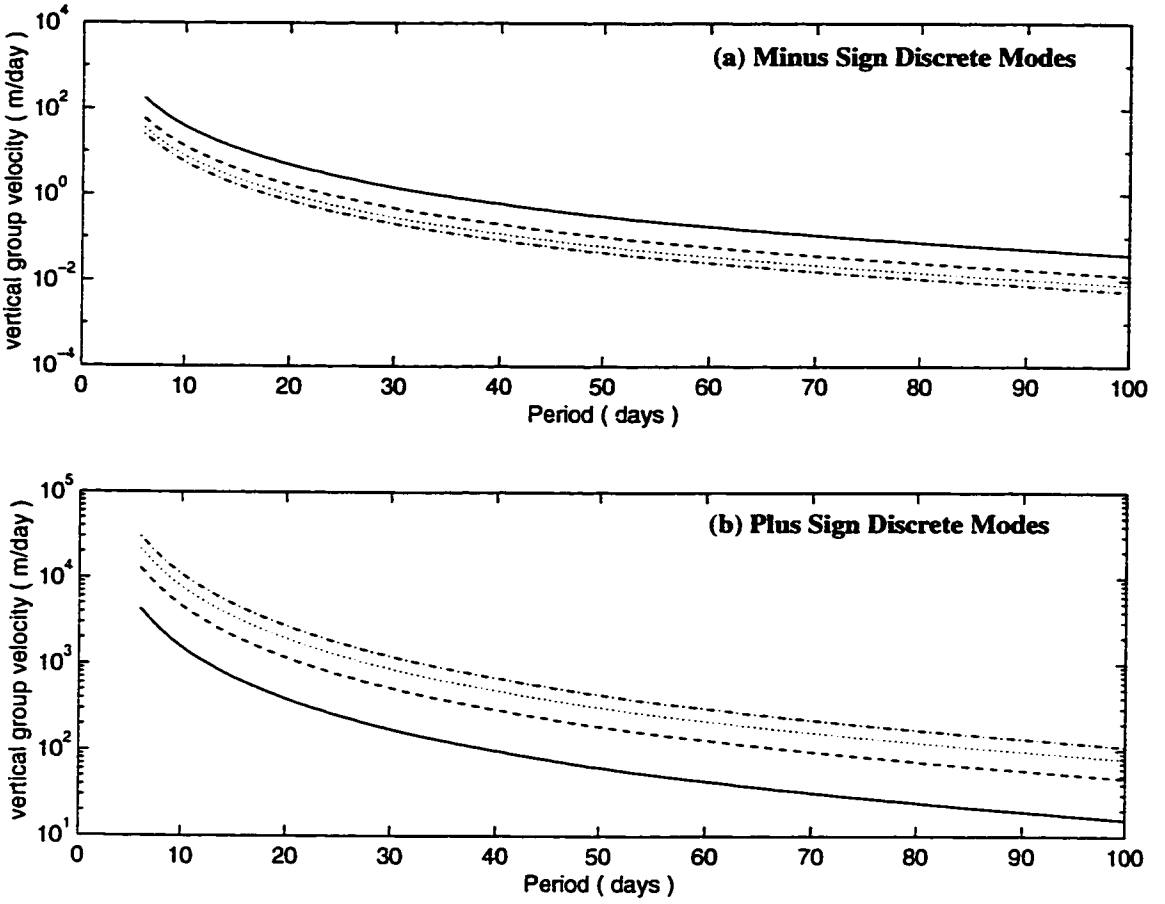

Figure 3.4: The vertical group velocity corresponding to minus sign discrete modes (panel a) and plus sign discrete modes (panel b) of zonal wave number one as a function of wave period. Solid lines correspond to $n = 0$, dashed lines $n = 1$, dotted lines $n = 2$, and dash-dotted lines $n = 3$. The value of the buoyancy frequency N used in this calculation is corresponds to an isothermal atmosphere with scale height H of 8 km; the vertical group velocity is plotted in meters per day.

Chapter 4

VERTICAL STRUCTURE OF HEATING AND THE THREE-DIMENSIONAL STRUCTURE OF THE FORCED CIRCULATIONS IN THE TROPICS

4.1. Introduction

In last chapter, the linearized equations of motion on an equatorial beta-plane were solved, assuming wave forms of solution in a zonally cyclic domain and using separation of variables. This procedure yields a homogeneous equation (the meridional structure equation) that defines meridional eigenfunctions and a non-homogenous vertical structure equation. Such a method is often called "the tidal approach" since it has long been used in the study of tides (Lindzen 1966, Lindzen 1967). In the last four decades, another theoretical method was also developed to account for the response of the tropical atmosphere to thermal forcing. That method is called the "the shallow water approach" in which one decomposes all the physical fields and forcing in terms of a set of vertical eigenfunctions and then solves a set of shallow water equations. In this section, we will first discuss both methods and their drawbacks and then outline our strategy to examine the relationships between vertical structure of heating and the three-dimensional structure of the forced circulations in the tropics.

4.1.1. The Tidal Approach

In the tidal approach, by solving the homogeneous meridional structure equation with appropriate boundary conditions at the infinities, one obtains the separation constants (which are the eigenvalues, historically called "the equivalent depths" in this context) and their corresponding meridional eigenfunctions. The non-homogeneous vertical structure equation is then solved to obtain the vertical structure of the forced response for each

meridional mode. The details of this approach can be found in the classic paper of Lindzen (1967). Lindzen (1968) further used this approach to explore the forced waves in the presence of Newtonian cooling. Dickinson and Geller (1968) showed that this approach can also be extended to the case in which the thermal damping has more complicated vertical structure.

A bothersome problem associated with the tidal approach is the completeness of the meridional eigenfunctions on an meridionally infinite equatorial β-plane. The completeness of these meridional eigenfunctions has long been assumed (Lindzen 1967) and has now been shown in Chapter 3 using a method similar to that of Holl (1970), who showed the completeness of the Hough functions. However, the equivalent depths and the corresponding eigenfunctions were not fully discovered until recently. The complete set of the eigenfunctions on a meridionally infinite equatorial β-plane includes three types: 1) the eigenfunctions of discrete positive equivalent depth which shrink to the equator as frequency goes to zero; 2) the eigenfunctions of discrete positive equivalent depth which approach to either of two sinusoidal functions (with one symmetric and the other antisymmetric about the equator) before they reach their turning points; and 3) the eigenfunctions of continuous negative equivalent depth. The first two types of eigenfunctions were discussed in Lindzen (1967), Lindzen and Matsuno (1968), Philander (1990), and Wu et al. (1997a). The third type of eigenfunctions were discovered by Moore (personal communication, 1997) and discussed in chapter 3 and appendix B. It was also shown in chapter 3 that the prescribed large-scale low-frequency heat source mainly projects onto the eigenfunctions of continuous negative equivalent depth. However, methods still need to be developed to quantitatively express the projection of the forcing onto these eigenfunctions.

The tidal approach has been quite successful in studying diurnal tides (Lindzen 1967), but it has not been widely used to understand the forced response to a large-scale low-fre-

quency heat source. The stumbling block is that at low frequencies, momentum damping can not be neglected. To obtain a non-homogeneous vertical structure equation and a homogeneous meridional structure equation, one must first perform a Fourier Transform in the zonal direction. In the presence of momentum damping, however, this means that the mass-weighted meridional velocity equation separates into a non-homogeneous vertical structure equation and a homogeneous meridional structure equation that has complex coefficients. For such a meridional structure equation, the completeness of the eigenfunction is not guaranteed. Hence, the variable separation method in the presence of momentum damping is again questionable and it is not clear that the tidal approach is capable of studying the forced large-scale low-frequency viscous response in the tropical atmosphere. The shallow water approach has been one of the most popular alternative approaches.

4.1.2. The Shallow-Water Approach

In the shallow-water approach, one separates the solution into a height-dependent part and a part that depends on the horizontal coordinates and time. The height-dependent part of the solution is expressed in terms of the vertical eigenfunctions (the vertical modes) which are obtained through the solution of the vertical structure equation under appropriate boundary conditions. For each of these vertical modes, variations in horizontal position and time are governed by the forced "shallow water" equations but with a different "equivalent depth" of homogeneous fluid. The overall solution is the summation of the contributions from each vertical mode.

The inviscid linear shallow water system on an equatorial β-plane was first solved by Matsuno (1966) in his study of free and forced waves in the tropics. Since then, many studies have used the shallow water system with a prescribed equivalent depth and linear damping (usually Rayleigh friction and Newtonian cooling) to describe the low-frequency

responses in both the tropics and extratropics to tropical thermal sources. Among them, Lau and Lim (1983) discussed the Hadley and Walker circulations associated with the East Asia winter monsoon; Lim and Chang (1983) focused on the dynamics of teleconnections and the Walker circulations forced by equatorial heating; and Zhang and Krishnamurti (1996) calculated the circulations driven by the global tropical thermal sources and sinks, which are inferred from a satellite-based field of the outgoing longwave radiation.

The most influential, albeit simple, study using such an approach is the Gill (1980) model. In his model, Gill assumed that the important contributions to the solution come only from modes with inverse vertical wavenumber that are of the same order as the scale of the forcing function. In his paper, he selected only one vertical mode, which was an idealized heat source having the structure of a single sinusoid from the surface to the tropopause with maximum heating in the mid troposphere, and concentrated on the horizontal structure of the response to thermal forcing. To obtain this normal mode representation, Gill implicitly imposed a lid at the top of the heating. Hence, the vertical structure of the solution is the same as the vertical structure of a vertically standing free mode that is generated by the artificial lid (Lindzen et al. 1968). The solutions to his model are essentially similar to the circulations simulated by Webster (1972) using a two layer numerical model.

Although Gill's solution is sometimes recognized as a good approximation to the horizontal structure of the response to an isolated large-scale heat source in the tropics, there are several problems associated with this model. One of them is that the heating is artificially brought down to the surface whereas the actual heating due to release of latent heat of condensation occurs above cloud base. Hence, the vertical transfer of heating from cloud base to the surface, which is extremely important in understanding the thermally forced surface winds in the tropics, can not be explored by a single mode system. To over-

come this drawback, Geisler and Stevens (1982) introduced the multi-mode method by imposing a rigid lid somewhere well-above the top of the heating and used the sum of all the (discrete) vertical normal modes to cancel the artificial heating induced by the Gill model outside of the heating layers. Similar multi-mode methods were later widely used (e.g., Silva Dias et al. 1983, Kasahara 1984, DeMaria 1985, Mapes and Houze 1995, and Mizzi et al. 1995). Hayashi (1976) and Silva Dias (1986) also examined the sensitivity of the vertical mode expansion to the location of the upper boundary of the model atmosphere and to the vertical resolution.

4.1.3. Problems to Solve

Although the multi-mode method improves the overall solution, this method also has drawbacks. The real atmosphere is semi-infinite in the vertical, and to what extent the imposed lid effects the response requires further investigation. Machenhauer and Daley (1974) and Eliassen and Machenhauer (1974) showed that changing the upper boundary condition not only affects the model results but also effects the computational stability associated with the model integration. Mapes and Houze (1995) demonstrated that the truncation of the vertical modes greatly affects the amplitude of the simulated surface winds. DeMaria (1985) and Mizzi et al. (1995) used similar vertical structure equations with corresponding lids at different heights to define the vertical eigenfunctions. Their results showed that the structure of the eigenfunctions are sensitively dependent on the height of the lid and that to diminish the effect of the lid many vertical modes must be retained to obtain an accurate solution.

It should be noted that in both the tidal approach and the shallow water approach, the separation constant is called the equivalent depth. However, the meaning of the equivalent depth (the separation constant) is different in these two different approaches. Mathematically, the equivalent depth is uniquely determined by the eigenvalue-eigenfunction

problem. Since the eigenvalue-eigenfunction problems are different in the tidal approach and in the shallow water approach, it is anticipated that the resulting sets of equivalent depths are different. Physically, most of the positive equivalent depth modes in the tidal approach represent the vertically propagating waves, and all the negative equivalent depth modes represent vertically trapped solutions (Philander 1990). However, in the shallow water approach, a positive equivalent depth of a vertical mode represents the depth of a hypothetical homogeneous fluid which describes the horizontal structure of the horizontal velocities and the geopotential perturbation of that particular vertical mode. Hence, *only in the shallow water approach can the equivalent depth represent the depth of a homogeneous fluid; and the equivalent depth in the tidal approach is only a mathematically symbol for the eigenvalue that only looks like the equivalent depth.*

In this chapter, we will develop a vertical decomposition method that is free of the previously mentioned drawbacks (i.e., the imposition of an artificial lid) in order to investigate the thermally forced tropical atmosphere. Geisler (1981) and Hartmann et al. (1984) showed that the vertical structure of the thermally forced response is significantly affected by the vertical structure of the heating. Lau and Peng (1987) and Sui and Lau (1989) showed that zonal propagation speed of the forced signal is sensitive to the vertical structure of the prescribed heating. However, a complete theoretical argument to answer why and how such relations exist has not yet been given. By calculating the projections of a prescribed vertical heating profile onto the vertical eigenfunctions, we will examine the contribution of different modes to the overall solution, and then further clarify how the vertical structure of the heating affects the three-dimensional (especially horizontal) structure of the response. In section 4.2, we separate the linear equations into a vertical structure equation and a set of shallow water equations. In section 4.3, we solve the vertical eigenvalue-eigenfunction problem in a semi-bounded atmosphere with a radiation condition at the top of the atmosphere. We project two thermal sources onto the vertical eigen-

functions in section 4.4 and discuss how the horizontal structure of the response to the convective plume heating (CP hereafter) is different from that of the response to the mature cloud cluster heating (MC hereafter). To verify the analytical results, we also carry out a series of numerical experiments in a dry primitive-equation general circulation model in section 4.5. The summary and conclusions are presented in section 4.6.

4.2. Separation of Variables

Eliminating w between equations (2.3c) and (2.3d) leads to

$$\frac{\gamma - i\omega}{N^2}\left(\frac{\partial^2}{\partial z^2} - \frac{1}{4H^2}\right)\Phi - \left(\frac{\partial u}{\partial x} + \frac{\partial v}{\partial y}\right) = \left(\frac{\partial}{\partial z} - \frac{1}{2H}\right)\frac{Q}{N^2}\,. \tag{4.1}$$

We define the vertical eigenfunctions by the equation

$$\frac{d^2 V_m}{dz^2} + \left(\frac{N^2}{gh_m} - \frac{1}{4H^2}\right)V_m = 0\,, \tag{4.2}$$

with the boundary conditions

$$\frac{dV_m}{dz} + \frac{V_m}{2H} = 0\,, \text{ at } z = 0\,, \tag{4.3a}$$

and

$$\textit{either } V_m \to 0 \textit{ or outgoing radiation condition,} \quad \text{as } z \to \infty\,. \tag{4.3b}$$

The boundary conditions (4.3a,b) are essential the same as the boundary conditions (2.4a,b), respectively.

Since equation (4.2) is defined in a semi-infinite domain, a relatively small positive equivalent depth renders a solution that is not Lebesgue square integrable in an interval containing infinity. In such a case, the differential operator in equation (4.2) is said to be in the *limit-point* case at infinity. The principle of analytic continuation requires that in such a case the corresponding Green's function (see also section 4.3) is defined by implicitly requiring the Green's function to vanish for large values of z if $\lambda = (N^2/gh_m - 1/4H^2)$ is complex and $Im\sqrt{\lambda} > 0$. For real values of λ, the Green's function is defined as the limit of the Green's function for complex values of λ as λ approaches the real axis. Hence, the differential operator in an infinite domain with a radiation boundary condition at infinity can be treated in the same way as when it is defined in a finite domain with regular (e.g., homogeneous, linear, incoming waves, outgoing waves, etc.) boundary conditions. (Details about that argument can be found in the sections about the continuous spectrum in chapter 4 of Friedman (1956).) Hence, the equation (4.2) and its boundary conditions (4.3a,b) define a complete set of eigenfunctions in the vertical under the concept of analytical continuation.

By expanding the variables in equations (2.3a), (2.3b), and (4.1) in terms of the vertical eigenfunctions V_m, i.e.,

$$\begin{bmatrix} u \\ v \\ \Phi \end{bmatrix} = \sum_m \begin{bmatrix} u_m(x, y) \\ v_m(x, y) \\ \Phi_m(x, y) \end{bmatrix} V_m(z), \tag{4.4}$$

one obtains

$$(\alpha - i\omega)u_m - \beta y v_m = -\frac{\partial \Phi_m}{\partial x}, \tag{4.5a}$$

$$(\alpha - i\omega)v_m + \beta y u_m = -\frac{\partial \Phi_m}{\partial y}, \tag{4.5b}$$

$$\frac{(\gamma - i\omega)}{gh_m}\Phi_m + \left(\frac{\partial u_m}{\partial x} + \frac{\partial v_m}{\partial y}\right) = -F_m, \tag{4.5c}$$

where F_m satisfies

$$\tilde{Q} = \left(\frac{\partial}{\partial z} - \frac{1}{2H}\right)\frac{Q}{N^2} = \sum_m F_m(x, y)V_m(z), \tag{4.6}$$

and the summation represents a sum over the discrete spectrum and an integration over the continuum.

4.3. The Vertical Eigenvalue-Eigenfunction Problem

We rewrite equation (4.2) as

$$\frac{d^2 V_m}{dz^2} + \lambda_m V_m = 0, \tag{4.7}$$

where

$$\lambda_m = \left(\frac{N^2}{gh_m} - \frac{1}{4H^2}\right). \tag{4.8}$$

The boundary conditions are given by equations (4.3a,b).

As described in Holton (1975), the eigenfunctions defined by the equation (4.7) and its boundary conditions include a continuous spectrum of modes that vary sinusoidally with height and one additional mode (the Lamb mode) for which the vertical displacement is zero but the pressure perturbation decays exponentially with height. Holton (1975) did not give the explicit expressions of these eigenfunctions. To obtain these eigenfunctions, we will use the method of the spectral representation of an differential operator, that is, we will construct the Green's function and integrate it around a large circle in the complex λ-domain to represent a δ-function. The details of the method of the spectral representation of an differential operator can be found in Appendix A and in Friedman (1956).

4.3.1. The Green's Function

The Green's function $G(z, \xi, \lambda)$ is a solution of the equation

$$\frac{d^2G}{dz^2} + \lambda G = -\delta(z-\xi) \tag{4.9}$$

that satisfies the lower boundary condition

$$G_z(0, \xi, \lambda) = -\frac{G(0, \xi, \lambda)}{2H}. \tag{4.10}$$

From (4.9) we see that

$$G = ae^{i\sqrt{\lambda}z} + be^{-i\sqrt{\lambda}z} \quad \text{for } z \neq \xi. \tag{4.11}$$

If λ is complex or if λ is real and negative, one of the terms on the right hand side in this

expression goes exponentially to ∞ and the other goes exponentially to zero as $z \to \infty$. It is clear then that for these values of λ the Green's function is Lebesgue integrable if, and only if, it goes to zero exponentially for large values of z. For real positive values of λ, both terms are bounded at infinity and neither term, nor the linear combination, is Lebesgue integrable. We therefore apply the principle of analytic continuation and define the Green's function for real positive values of λ to be the limit of the Green's function with complex λ as λ approaches the real axis.

Notice that this definition still does not specify the Green's function uniquely because λ may approach the positive real axis from above or from below, and these two different approaches will give different Green's functions. If we consider values of λ such that $Im\sqrt{\lambda} > 0$, the Green's function for real positive values of λ will behave like a multiple of $e^{i\sqrt{\lambda}z}$ for large values of z. On the other hand, if we consider values of λ such that $Im\sqrt{\lambda} < 0$, the Green's function for real positive values of λ will behave like a multiple of $e^{-i\sqrt{\lambda}z}$ for large values of z. Since we have already assumed a time factor $e^{-i\omega t}$, only the Green's function defined by analytic continuation from the Green's function for $Im\sqrt{\lambda} > 0$ will behave like "outgoing waves" for large values of z. Henceforth, the "Green's function" will refer to the Green's function that represents outgoing waves at infinity and automatically satisfies "the radiation boundary" at infinity. From the description above, "the radiation condition" is the natural boundary condition both physical and mathematical for the semi-infinity atmosphere.

Let us now return to the solutions of (4.10) and (4.11) for complex values of λ. We assume that $0 < \arg\lambda < 2\pi$ and choose the branch of the square root for which

$$0 < \arg\sqrt{\lambda} < \pi . \tag{4.12}$$

The term $e^{i\sqrt{\lambda}z}$ will vanish exponentially as z approaches infinity. Consequently, one determines coefficients a and b in equation (4.11) by using the continuous requirement and derivative jump requirement

$$\left.\frac{dG}{dz}\right|_{\xi^-}^{\xi^+} = -1 \tag{4.13}$$

for G at $z = \xi$. The solution for G is

$$G = \left(\cos\sqrt{\lambda}z - \frac{1}{2H\sqrt{\lambda}}\sin\sqrt{\lambda}z\right)\frac{e^{i\sqrt{\lambda}\xi}}{i\sqrt{\lambda} + 1/(2H)}\mathcal{H}(\xi - z) +$$

$$\left(\cos\sqrt{\lambda}\xi - \frac{1}{2H\sqrt{\lambda}}\sin\sqrt{\lambda}\xi\right)\frac{e^{i\sqrt{\lambda}z}}{i\sqrt{\lambda} + 1/(2H)}\mathcal{H}(z - \xi) , \tag{4.14}$$

where $\mathcal{H}(\eta)$ is Heaviside unit function.

4.3.2. The Vertical Eigenfunctions

The spectral representation of an operator $L = -d^2/dz^2$ can be expressed in terms of the Green's function defined by equation (4.9)

$$\lim_{R\to\infty}\frac{1}{2\pi i}\oint G(z, \xi, \lambda)d\lambda = -\delta(z - \xi) , \tag{4.15}$$

where G is given by equation (4.14). It can be shown that

$$\frac{1}{2\pi i}\oint G d\lambda = \frac{1}{2\pi i}\oint \frac{e^{i\sqrt{\lambda}|z-\xi|}}{i\sqrt{\lambda}+1/(2H)} d\lambda \tag{4.16}$$

plus terms of higher order in $1/R$. Put $\lambda = m^2$ of positive m, and we get

$$\frac{1}{2\pi i}\oint G d\lambda = \frac{1}{2\pi i}\oint \frac{e^{im|z-\xi|}}{im+1/(2H)} 2m dm \tag{4.17}$$

plus terms that go to zero as $R \to \infty$.

Cauchy's theorem is used to deform this circle into a contour around the singularities of G. Note that G has a branch point singularity at $\lambda = 0$ and a possible pole at $\sqrt{\lambda} = i/2H$. Because of the branch-point singularity, the value of G at A in Fig. 4.1 is not the same as the value of G at B; consequently, Cauchy's theorem does not apply to the circle ACB since G is not a single-value function on this contour. However, on the curve $ACBDA$ (here the real axis has been taken as a branch cut) the function G is a single-valued, and therefore by Cauchy's theorem

$$\frac{1}{2\pi i}\int_{ACBDA} G d\lambda \tag{4.18}$$

equals the sum of the residues of G inside the circle. The only possible singularity of G inside the circle is the point P, where $\sqrt{\lambda} = i/2H$. Since P is located at negative real axis, it is inside the circle and is a singularity. The residue at P is

$$-\frac{1}{H} e^{-(z+\xi)/2H}[\mathcal{H}(\xi - z) + \mathcal{H}(z-\xi)] = -\frac{1}{H} e^{-(z+\xi)/2H}. \tag{4.19}$$

From (4.18) and (4.19), one obtains

$$-\frac{1}{H}e^{-(z+\xi)/2H} = \frac{1}{2\pi i}\int_{ACBDA} G d\lambda = \frac{1}{2\pi i}\int_{ACB} G d\lambda + \frac{1}{2\pi i}\int_{BDA} G d\lambda, \qquad (4.20)$$

and, therefore, the first integral on the right-hand side of equation (4.20) gives a δ-function:

$$-\delta(z-\xi) = \frac{1}{2\pi i}\int_{ACB} G d\lambda = -\frac{1}{H}e^{-(z+\xi)/2H} - \frac{1}{2\pi i}\int_{BDA} G d\lambda. \qquad (4.21)$$

The last integral may be simplified by putting $\lambda = m^2$ of positive m. Note that on the upper side of the cut $\sqrt{\lambda} = m$, but on the lower side of the cut $\sqrt{\lambda} = -m$. One has

$$\begin{aligned}
\frac{1}{2\pi i}\int_{BDA} G d\lambda = {} & \frac{1}{2\pi i}\int_0^\infty \left(\cos mz - \frac{1}{2Hm}\sin mz\right)\frac{e^{imz}H(\xi-z)}{im+1/(2H)}2m dm \\
& + \frac{1}{2\pi i}\int_0^\infty \left(\cos mz - \frac{1}{2Hm}\sin mz\right)\frac{e^{imz}H(z-\xi)}{im+1/(2H)}2m dm \\
& + \frac{1}{2\pi i}\int_0^\infty \left(\cos mz - \frac{1}{2Hm}\sin mz\right)\frac{e^{imz}H(\xi-z)}{-im+1/(2H)}2m dm \\
& + \frac{1}{2\pi i}\int_0^\infty \left(\cos mz - \frac{1}{2Hm}\sin mz\right)\frac{e^{imz}H(z-\xi)}{-im+1/(2H)}2m dm. \qquad (4.22)
\end{aligned}$$

Combining the first and third integrals and also the second and fourth integrals yields

$$\frac{1}{2\pi i}\int_{BDA} G d\lambda = -\frac{2}{\pi}\int_0^\infty \left(\cos mz - \frac{1}{2Hm}\sin mz\right)\left(\cos m\xi - \frac{1}{2Hm}\sin m\xi\right)\frac{m^2}{m^2+1/(4H^2)}dm. \qquad (4.23)$$

Substituting (4.23) into (4.21), one finally obtains

$$\delta(z-\xi) = \frac{1}{H}e^{-(z+\xi)/2H}$$

$$+\frac{2}{\pi}\int_0^\infty\left(\cos mz-\frac{1}{2Hm}\sin mz\right)\left(\cos m\xi-\frac{1}{2Hm}\sin m\xi\right)\frac{m^2}{m^2+1/(4H^2)}dm\,. \quad (4.24.)$$

Equation (4.24) states that the eigenfunctions defined by the vertical structure equation (4.7) and its boundary conditions are complete and have two parts: one discrete mode that exponentially decays in the vertical, and continuous modes of any vertical wavenumber. Hence, one obtains the discrete eigenfunction (often called the external mode or the barotropic mode) that has the form

$$V_e(z) = e^{-\frac{z}{2H}}, \quad (4.25a)$$

and the continuous modes (often called the internal modes or the baroclinic modes) that have the form

$$V_{mi}(z) = \left(\cos mz-\frac{1}{2Hm}\sin mz\right)\frac{2Hm}{\sqrt{4H^2m^2+1}}, \quad (4.25b)$$

with m being any positive real number.

The discrete mode (4.25a) is often called the barotropic mode or external mode. Although the equivalent depth for this mode results from the vertical eigenvalue-eigenfunction problem approaches infinity, in the tidal approach (Lindzen 1967) this mode *is* the Lamb mode which is regarded as a free mode with an equivalent depth of $H/(1-\kappa)$. A feature of the Lamb mode is that the velocity is everywhere parallel to the Earth's surface, i.e., $w = 0$ (e.g., Gill 1982). The continuous modes represent all the

baroclinic modes in a semi-bounded atmosphere. When the scale height H approaches infinity (the incompressible limit), the discrete mode disappears and the continuous modes become the Fourier integral in a semi-bounded domain.

This section shows that the shallow water approach not only works for the vertically standing (free and forced) waves when an artificial lid is imposed but also is applicable to the vertically propagating forced waves. A key distinction between an atmosphere with a lid and a vertically unbounded atmosphere is that the free modes and the forced modes in the vertical are not distinguishable in an atmosphere with a lid: the zero vertical velocity requirement at the top and at the surface along with the vertical eigenvalue-eigenfunction equation defines the same complete set of vertical standing modes for both free and forced waves. For a vertically semi-bounded atmosphere, however, free vertically propagating baroclinic waves can not survive since wave energy always radiates to space, leaving only the forced waves. These forced vertically propagating modes of wavelength $2\pi/m$ then have a horizontal structure of a shallow water system of equivalent depth $N^2/[g(m^2 + 1/4H^2)]$.

4.4. Thermally Forced Tropical Circulation: Two Idealized Cases

Some simple analytical solutions to a forced shallow water system with a single positive equivalent depth were given by Matsuno (1966) and Gill (1980). With prescribed linear damping, the steady solution to equations (4.5a-c) is characterized by the Kelvin signal that decays to the east of the heat source and the Rossby signals that decay to the west of the heat source. The zonal distance the signals can reach is characterized by the product of the damping time scale and the zonal group speed. Since the propagation speed of the Kelvin signal is three times large as that of the fastest Rossby signal, the response to the east of the heat source extends about three times farther than that to the west of the heat

source. Since the zonal group speeds of the Kelvin and Rossby signals are determined by the equivalent depth of the shallow water system, in a zonally cyclic domain Gill's solution can be an approximate solution only for sufficiently small equivalent depth, sufficiently large damping, or both. Otherwise, the eastward and westward propagating signals will extend around the circumference of the Earth and interfere with each other.

For vertically isolated heating, the vertical structure of the response can not be resolved by a single vertical mode. Hence, the original three dimensional system must be decomposed into a infinite set of shallow water systems. For each shallow water system, the horizontal structure of the response to a heat source of a given horizontal structure is different since the equivalent depth of each vertical mode is different. In addition to that, the amplitude of the response is also affected by how much of the input energy goes to each mode. Since the overall solution is the summation of the contributions from all vertical modes, the projection of the vertical heating profile onto the vertical eigenmodes becomes the key factor in characterizing the structure of the thermally forced response.

4.4.1. The Projection of Heating onto the Vertical Eigenfunctions

To facilitate the discussion of which vertical modes contribute significantly in the response to prescribed heating, we first introduce the vertical wavelength l of a baroclinic (internal) mode

$$\left(\frac{2\pi}{l}\right)^2 = m^2 = \left(\frac{N^2}{gh_m} - \frac{1}{4H^2}\right). \tag{4.26}$$

Equation (4.26) gives the relationship between the vertical wavelength l and the equivalent depth h_m of the corresponding shallow water system. Fig. 4.2 plots the square root of

the equivalent depth $\sqrt{gh_m}$ (the horizontal gravity wave speed of a vertical mode) as a function of the corresponding vertical wavelength l for an isothermal atmosphere of temperature 300 K. (The corresponding scale height H is 8.785 km and the buoyancy frequency squared N^2 is 3.2×10^{-4} s^{-2}.) The "*" point corresponds to the mode with gravity wave speed of 60 ms^{-1}. The vertical wavelength corresponding to that equivalent depth is smaller in this case than that in Gill (1980) since we choose an isothermal atmosphere that has relatively larger N^2.

For simplicity, we assume that the heating rate $\tilde{Q}$ in equation (4.6) has the separable form $P(z)S(x, y)$. Then, we obtain

$$F_m(x, y) = F(m)S(x, y), \tag{4.27}$$

where $F(m)$ is the projection of $P(z)$ onto the vertical eigenfunction $V_m(z)$. The expression of $P(z)$ in terms of the vertical eigenfunctions is

$$P(z) = F_e e^{-\frac{z}{2H}} + \sqrt{\frac{2}{\pi}} \int_0^\infty F_i(m) \left(\cos mz - \frac{1}{2Hm} \sin mz \right) \frac{2Hm}{\sqrt{4H^2 m^2 + 1}} dm, \tag{4.28}$$

where F_e is the projection of $P(z)$ onto the external mode

$$F_e = \frac{1}{H} \int_0^\infty P(z) e^{-\frac{z}{2H}} dz, \tag{4.29a}$$

and $F_i(m)$ is the projection of $P(z)$ onto an internal mode

$$F_i(m) = \sqrt{\frac{2}{\pi}}\int_0^\infty P(z)\left(\cos mz - \frac{1}{2Hm}\sin mz\right)\frac{2Hm}{\sqrt{4H^2m^2+1}}dz. \qquad (4.29b)$$

Parseval's Theorem states that the energy E is given by

$$E = \int_0^\infty |P(z)|^2 dz \approx \int_0^\infty F^2(m)dm = \int_0^\infty \frac{2\pi F^2(l)}{l^2}dl, \qquad (4.30)$$

where the "≈" indicates that the contribution from the external mode is neglected since it contributes little to the total integral when large-scale convective heating is considered. $F^2(m)$ is often called the power spectrum and $2\pi F^2(l)/l^2$ is here called the spectral energy density with respect to vertical wavelength l. *The relative importance of the different modes in accounting for the overall response can be quantified by these two quantities.*

4.4.2. Responses to Two Vertical Heating Profiles

We consider a heat source associated with the large-scale persistent precipitation in the tropics (for example, the large-scale convective heating over the maritime continent near Indonesia). Since the vertical structure of the tropical heating related to cumulus convection varies with time and location (e.g., Frank and McBride 1989), it is difficult to find an exact representation of a realistic large-scale tropical heat source. Thus, here we simply follow Hartmann *et al.* (1984) and consider two different heating profiles: an idealized profile representing the total heating produced by convective plumes alone (CP), and an idealized profile representing the total heating produced by strataform cloud heating typical of a mature tropical cloud cluster (MC). Although the long term mean heating has a similar vertical structure to that of CP (Mapes and Houze 1995), the MC profile is exam-

ined to show that the vertical structure of the heating is one of the key factors in determining the three dimensional structure of the atmospheric response to a prescribed heating. The two heating profiles are expressed as

$$J(z) = \begin{cases} 0 & z \geq z_t \\ e^{\frac{z}{2H}} \sin\left(\frac{z - z_b}{z_t - z_b}\pi\right) & z_b < z < z_t \\ 0 & z \leq z_b \end{cases}, \tag{4.31}$$

where z_t is the cloud top (somewhere close to the tropopause) that is assumed to be at 16 km. The bottom of the heating at $z = z_b$ is assumed to be at 0.6 km and 4 km for the CP and the MC, respectively. The normalized vertical structures of J, Q, and $\tilde{Q}$ are plotted in Fig. 4.3. The contribution to $\tilde{Q}$ by the term with the scale height H in equation (4.6) is small (see Fig. 4.3). Hence, for simplicity we take

$$P(z) \approx \begin{cases} 0 & z \geq z_t \\ \cos\left(\frac{z - z_b}{z_t - z_b}\pi\right) & z_b < z < z_t \\ 0 & z \leq z_b \end{cases}. \tag{4.32}$$

From equations (4.29b) and (4.32), we obtain

$$F(m) = -\frac{m}{m^2 - n^2} \cdot \frac{1}{\sqrt{1 + 4H^2 m^2}} \cdot \sqrt{\frac{2}{\pi}} [2Hm(\sin mz_t + \sin mz_b) + \cos mz_t + \cos mz_b], \tag{4.33}$$

where $n = \pi/(z_t - z_b)$.

Equations (4.28) and (4.30) are used to calculate projections $P(z)$ of the heating onto the internal modes for these two cases; solutions are shown in Fig. 4.4. In both cases, the spectrum of the heating is dominated by the modes with vertical wavelength greater than 10 km; the modes with small vertical wavenumber do not contribute much to the forced response. The spectral energy distribution with respect to the vertical wavenumber is very sensitive to the location of the cloud base. For the MC case, the energy is dominated by the modes whose vertical wavelength is around 14 km (corresponding to a gravity wave speed of 40 ms^{-1}), while for the CP case, more than 70% of the energy is carried by the modes of the vertical wavelength greater than 18 km.

These differences are significant for the interpretation of the forced response. Gill (1980) showed that for a shallow water system, the amplitude of the zonal velocity to the east of the heating can be expressed as

$$u(x+\Delta x) = u(x)\exp(-\alpha \cdot \Delta t) = u(x)\exp\left(-\frac{\Delta x}{cT}\right), \tag{4.34}$$

where, α is the Rayleigh friction rate, T is the time scale of Rayleigh friction, and c is the gravity wave speed of the shallow water system. Since modes of different vertical wavelength propagate at different speeds, under the same linear damping, one could expect that a signal associated with larger vertical wavelength will decay slower in the zonal direction and would be detected farther away from the heat source than the signal with the shorter vertical wavelength. For this reason, we anticipate that the forced response to CP will decay slower in the zonal direction than in the response to MC, and it will result in solutions with different horizontal structures.

The drawback of a single mode approach used in Gill (1980) is also clear from Fig. 4.4. If the spectral energy density $2\pi F^2(l)/l^2$ is highly concentrated around some mode, it may be appropriate to approximate the response by just considering that single mode. However, Fig. 4.4 shows that the spectral energy is distributed broadly over vertical wavelength and is very sensitive to the vertical structure of the heating. Since the contribution from a single mode at a given height is dependent on the height, the overall solution at a given height will, in general, exhibit height dependent horizontal decay rates. Such a result is clearly in contrast to the Gill solution in which the horizontal decay rate is vertically uniform.

4.5. Numerical experiments

In this section, we analyze the results from two idealized numerical experiments, in which the vertical structure of the heating is prescribed as either CP or the MC. We examine the circulation patterns associated with both cases, and determine to what extent the model results can be explained by the linear theory presented in the previous sections.

4.5.1. The Model and Experiments

The model we use is the dry version of the primitive equation model developed by Saravanan and McWilliams (1995). The main features of the model are described in chapter 2.

The model atmosphere does has an artificial rigid top lid. Such an artificial lid produces the spurious free oscillations that are resonant when the atmosphere is forced (Lindzen *et al.* 1968). In general, an atmosphere bounded by a lid does not properly respond to oscillations that propagate vertically since a lid leads to spurious reflection of wave energy that does not occur in a semi-bounded atmosphere. To avoid this drawback, a

common approach is to incorporate strong damping at the top of the models to absorb vertically propagating waves (e.g., Hendon and Salby 1996). This approach is justified for low-frequency forcing in the presence of dissipation because the waves are damped before they reach the lid (Geisler and Stevens 1982).

In general, the time scale of Newtonian cooling is of the order of two weeks and that of Rayleigh friction is about 5 to 10 days. When the damping terms are assumed to represent cumulus friction and vertical transport of heat by cumulus convection, both the effective Rayleigh friction and Newtonian cooling can be of the order of a day or less in the tropics. Holton and Cotton (1972) pointed out that the damping used in a linear model need to be much stronger (less than a day) than people generally would believe to mimic for some of the nonlinearity existed in the tropical atmosphere. In this chapter, the Rayleigh friction rate and the Newtonian cooling rate are taken to be $\alpha^{-1} = \gamma^{-1} = 2.5$ days everywhere. These damping rates are close to the values used in Gill (1980) when a gravity wave speed of 60 ms^{-1} is selected and are twice as large as those used in other models (e.g., Geisler 1981). The model results to be discussed in the following are not qualitatively dependent on the values of the damping rates. The model results also show, for the values of dissipation used, that the solutions are almost independent of the artificial lid, as long as the lid is well above the top of the isolated heat source.

The heat source is prescribed to be

$$Q = \exp(-(\lambda - \lambda_0)^2/\lambda_L^2)\exp(-\phi^2/\phi_L^2)\mathcal{F}(p), \tag{4.35}$$

where λ is longitude, λ_0 is reference longitude with value of $93°E$, $\lambda_L = 20°$, ϕ is latitude, and $\phi_L = 11°$, and $\mathcal{F}(p)$ corresponds to the heating prescribed in section 4.4. Fig.

4.5 plots the normalized three-dimensional structure of that heat source. The solid line and the dashed line in Fig. 4.5*a* are the same vertical profiles as the solid lines in Fig. 4.3a and Fig. 4.3b where the *log pressure corrodinate* rather than the *p-coordinate* was used. The maximum heating rate is set by requiring the vertically integrated heating to be equivalent to the amount of latent heating provided by 10 mm of precipitation per day (corresponding to 2.5 K/day). The heating amplitude is not crucial in this study: numerical experiments show that the three dimensional structure of the response is not sensitive to the amplitude of the heating as long as the maximum heating rate corresponds to less than 20 mm per day of precipitation. However, the amplitude of the response is approximately proportional to the maximum heating rate. Hence, the modeled response is essentially linear.

The global kinetic energy and the global perturbed potential energy for both cases approach to their approximate steady states in a couple of model weeks. We therefore run both model experiments for 100 model days to approach an approximate equilibria.

4.5.2. The Forced Three-Dimensional Responses in the Primitive-Equation Model

In the previous sections, it has been shown that the signals carried by modes of different vertical wavelength propagate horizontally at different speeds. The larger the vertical wavelength of a mode, the faster the signal carried by this mode can propagate. The theoretical gravity wave speed limit for the baroclinic mode in an isothermal atmosphere of $300°K$ is 314 ms^{-1} (that is also the sound wave and Lamb wave speed) as indicated by equation (4.26) when the vertical wavenumber is taken to be zero. From equations (4.30) and (4.33), we expect that contributions by modes with extremely large vertical wavelength are very small for the MC and CP heating profiles. Hence, we expect the largest wave speed detected in the numerical experiments would be somewhat smaller than 314

ms^{-1}.

Fig. 4.6 plots the zonal velocity along the equator at 810 hPa level for the CP case at the Equator throughout the first day of the integration. In the early stages of spin-up, the amplitude of the forced signal is much smaller than that of the equilibrium (steady) solution at any given location, hence, the damping plays a relatively insignificant role and the forced signal propagates almost freely. Although the kinetic energy, which includes the contribution from all the modes, will disperse, signal fronts that propagate fastest are easy to detect. The slopes of the bold arrows in Fig. 4.6 which are tangent to isotachs mark the propagation speed of the signals of different vertical wavelength. The propagation speed of the fastest mode in the model by tracking incipient front as it travels along the equator. In this case, the speed of the fastest eastward propagating mode can be determined by tracking the zero contour of zonal wind, which indicates the fastest mode travels at about 250 ms^{-1}. This speed is comparable to the analytical value (314 ms^{-1}) and does not depend on details of the heating profile. From equation (4.33) and Fig. 4.4b, we can infer that contributions from the modes with gravity wave speed greater than 250 ms^{-1} are negligible. Hence, the numerical model used for this study is capable of simulating the true relationship between the vertical structure of the convective heating and the three-dimensional structure of the forced circulation in a vertically semi-bounded atmosphere.

The general features of the steady solution for the MC case are shown in Fig. 4.7 and Fig. 4.8. The response is mainly confined in the vertical to where the heating is located (Fig. 4.7): above and below the heating, the response is quite weak. The zero zonal wind contour is located around the 370 hPa which is much lower than the maximum heating level of about 270 hPa. In the meridional direction the response is confined mainly to the tropics. To the west of the heat source (Fig. 4.7*a*), the upper troposphere is dominated by

easterlies centered at the Equator with narrow bands of relatively weak westerly wind on the poleward flanks. The zonal wind in the lower troposphere is opposite to that in the upper troposphere and with a relatively small amplitude (also see Fig. 4.8). To the east of the heat source (Fig. 4.7*b*), the lower troposphere is dominated by easterlies and upper troposphere by westerlies and the zonal winds in upper troposphere has relatively larger amplitude. The maximum zonal wind level is at about 190 hPa in the upper troposphere and 560 hPa in the lower troposphere (see, Fig. 4.7*c*). The forced signal decays zonally away from the heat source, with much larger decay rate to the west of the heating (Fig. 4.8). Although the horizontal structure of the wind field at both levels is similar to that shown in Gill (1980), the zonal decay scale is smaller at 560 hPa than at 190 hPa (also see Fig. 5*c*), indicating that the contributions from different modes are different at different levels.

The steady circulation for the CP case is shown in Fig. 4.9 and Fig. 4.10. From Fig. 4.9, it is seen that the zero zonal wind level is at about 450 hPa, which is again far below the maximum heating level. Above the heating top, the response is again very small. However, the response now extends below the heating and to the ground. The maximum zonal wind level is at about 210 hPa in the upper troposphere and 810 hPa in the low troposphere (see, Fig. 4.9*c*). The horizontal structure of the wind field at these two levels is shown in Fig. 4.10. Unlike the MC case, in the CP case the zonal decay rate at the upper and lower maximum wind levels is very similar. This difference is more obvious in Fig. 4.11, where the zonal velocity from $137.8°E$ to $300.9°W$ along the Equator and along $10.7°N$ and at different levels are shown for both cases. It is clear that the zonal decay rate is dependent on height, latitude, and the structure of the heating profile.

To quantitatively describe these differences, we introduce the concept of effective

gravity wave speed. An effective gravity wave speed $\bar{c}$ is defined as the gravity wave speed of a hypothetical linear shallow water system that best approximates the multi-mode system at a given location. From equation (4.34), an local estimate of $\bar{c}$ is

$$\bar{c} = \frac{\Delta x}{T \cdot \ln\left(\frac{u(x)}{u(x+\Delta x)}\right)}, \tag{4.36}$$

where Δx is the zonal distance between neighboring grid boxes where u is measured and T is the damping time scale of Rayleigh friction. Fig. 4.12 shows contours of the effective gravity wave speed at the levels where the wind is an extreme in the vertical and to the east of the heating. It is clear that the effective gravity wave speeds are generally much larger in the CP case than in the MC case. The effective gravity wave speeds are different at upper troposphere and lower troposphere, but this difference is more notable in the MC case. At every level, the effective gravity wave speed increases with increasing latitudes from the equator because the slower wave modes will have experienced their turning latitudes, leaving only the faster (larger vertical wavelength) modes to carry the forced signal to the higher latitudes. Regardless of the type of heating, the effective gravity wave speed also becomes larger to the east until the longitude is reached where the Rossby wave signal significantly contributes.

As the forced signal propagates to the east, the part carried by the Kelvin solution with relatively smaller gravity wave speed is easily damped, leaving the faster Kelvin solutions to dominate the response. This is further shown in Fig. 4.13, where the vertical profiles of the zonal wind and their spectral energy densities with respect to the vertical wavelength are plotted for both cases. From panels *a* and *b* of Fig. 4.13, we see that the vertical scale of the response becomes larger and larger toward the east. Fig. 4.13*c* and *d* plots the den-

sities for the mass-weighted zonal velocities for the CP case and the MC case, respectively. By comparing the solid line in Fig. 4.13*c* with the solid line in Fig. 4.4*b*, we see that the spectral energy density of the mass-weighted zonal velocity immediately east of the heating resembles the spectral energy density of the heating. But at $149.1°W$, the modes with vertical wavelengths smaller than 10 km have diminishingly small amplitude. Further to the east at $81.8°W$, only the modes with vertical wavelengths greater than 16 km have survived. Similar decay properties also hold for the MC heating case.

In summary, the different heat profiles produce solutions that feature differences in: the zero wind level, the three-dimensional structure of the zonal decay rate, and the wind field below the heating. Clearly, a single vertical mode approximation is incapable of approximating the qualitative three-dimensional structure of the response to tropical heating.

4.6. Discussion and Summary

We have examined in this chapter the three-dimensional structure of the response to an isolated, steady, large-scale heat source in the tropics using both analytical arguments and numerical simulations of a dry primitive equation model of the atmosphere. In the analytical part of the study, we separate the linear equations into a homogeneous vertical structure equation and a set of forced shallow water equations. By solving the vertical eigenvalue-eigenfunction problem in a vertically semi-bounded domain, we obtained the eigenvalues and a complete set of vertical eigenfunctions which include a discrete barotropic mode and a continuous spectrum of baroclinic modes. These vertical eigenfunctions were used to decompose two different vertical heating profiles: a profile that represents the total heating produced by an ensemble of deep convective plumes (the CP case), and a

profile that represents the net heating produced by the aggregate heating due to a mature tropical cloud cluster (the MC case) which includes strataform and deep convective clouds. By examining the spectral energy density of the heating profiles and considering the steady solution to the shallow water system given by Gill (1980), the three dimensional structure of the response to each heating profile is analyzed. To verify the analytical results, we carry out complementary numerical experiments.

The results from both the analytical and the numerical simulations are consistent in showing that the vertical structure of the heating is fundamental to determining the structure of the response to a thermal source. Since the spectrum of the modes that contribute to the overall solution is very broad, under the same damping the signals carried by different modes possess different propagation speeds and different spatial decay rates, and hence, the relative contributions of different modes to the overall solution are different at different locations: the relative contribution to the net solution due to modes of large vertical wavelengths increases as one moves farther away from the heating.

Compared to the MC heating, the CP heating is deep and projects onto vertical eigenfunctions with relatively larger equivalent depth, so the forced signals propagate away from the heat source much faster than those forced by the MC heating. Hence, the averaged spatial decay rate of the signals forced by the convective plume heating is significantly smaller than the decay rate of the signals in the mature cloud cluster heating case and, as a result, the propagating signals can be detected farther away from the heat source in the CP case.

The numerical results show that the zero zonal wind level is far below the maximum heating level. This implies that a single-vertical-mode model (e.g., the Gill Model) is incapable of approximating the forced response throughout the tropics. The theoretical explanation is as follows: since different modes have different vertical structures, the rela-

tive contribution from each mode is different at different heights. Hence, it is extremely difficult to select a single suitable equivalent depth for a shallow water system to approximate the three-dimensional structure of the response to a given heating. This argument is confirmed by the model experiments through examining the effective gravity wave speed.

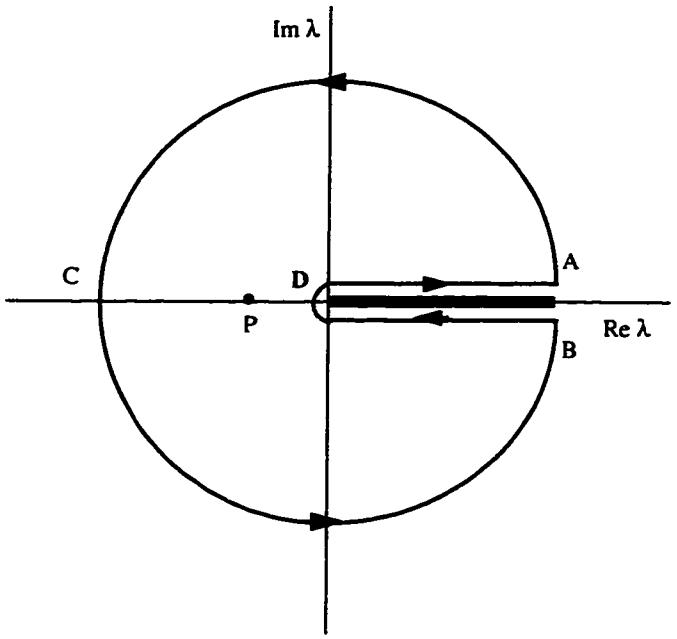

Figure 4.1: The contour **C** in the complex λ-domain along which the Green's function should be integrated. Since the Green's function at positive real axis is multi-valued, a branch-cut is performed. Point P is a pole of the Green's function.

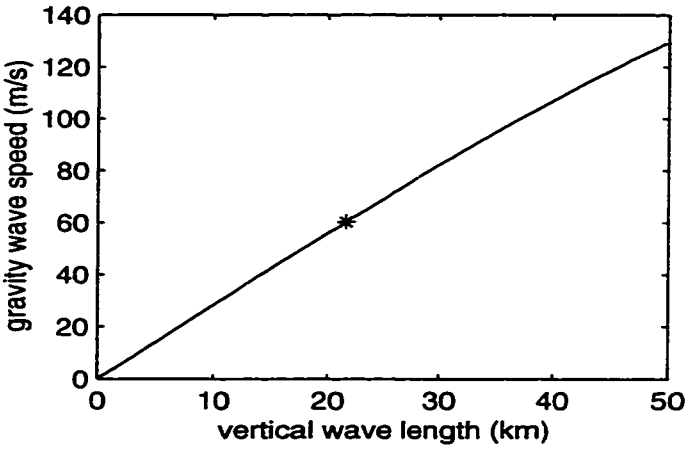

Figure 4.2: The plot of the gravity wave speed against the vertical wave length for a baroclinic mode in an isothermal atmosphere of 300 K. The '*' point corresponds to the gravity wave speed of 60 m/s.

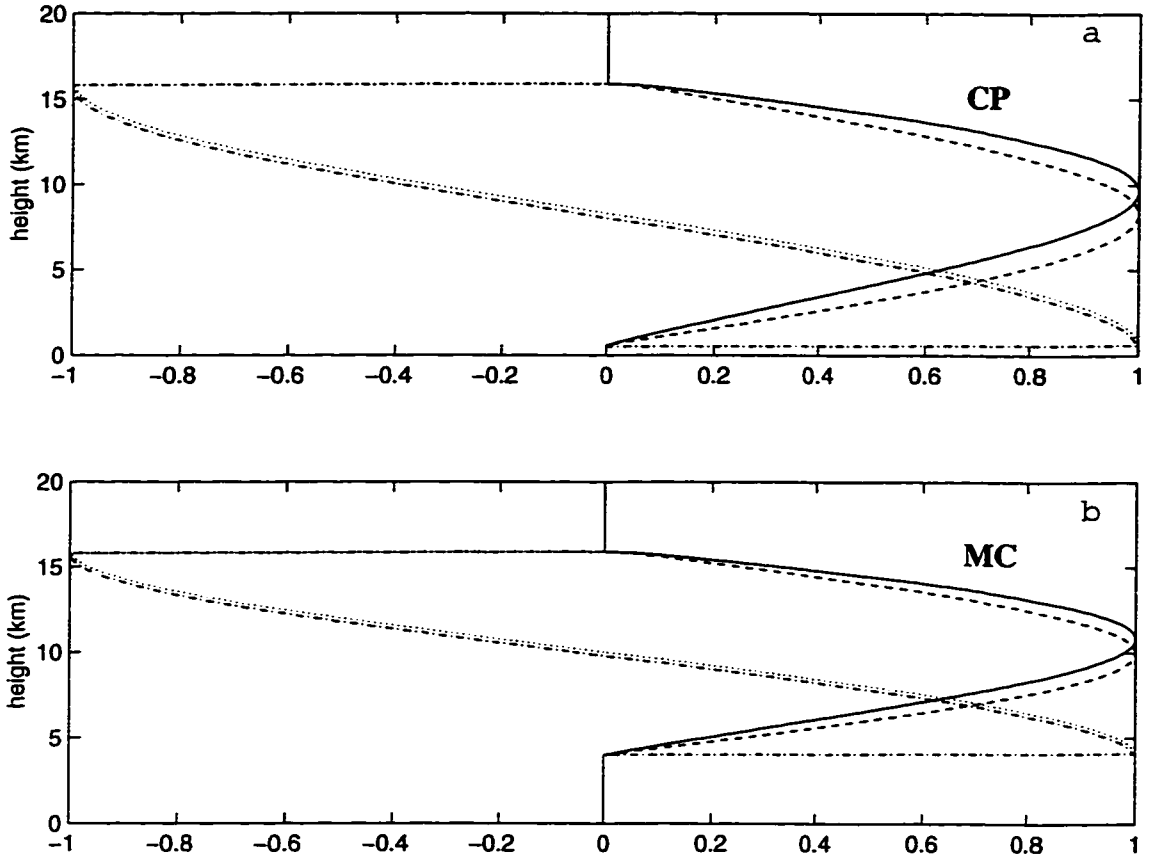

Figure 4.3: The normalized vertical heating profiles in the analytical study for two idealized cases: the convective plume heating (CP) case (panel a); and the mature cloud cluster heating (MC) case (panel b). In each panel, the solid line represents the vertical structure of the external heating rate J; the dashed line represents the vertical structure of the mass weighted external heating rate Q; the dash-dotted line is the vertical structure of the forcing function $\tilde{Q}$ defined by equation (4.31); and the dotted line is $P(z)$ given by equation (4.32).

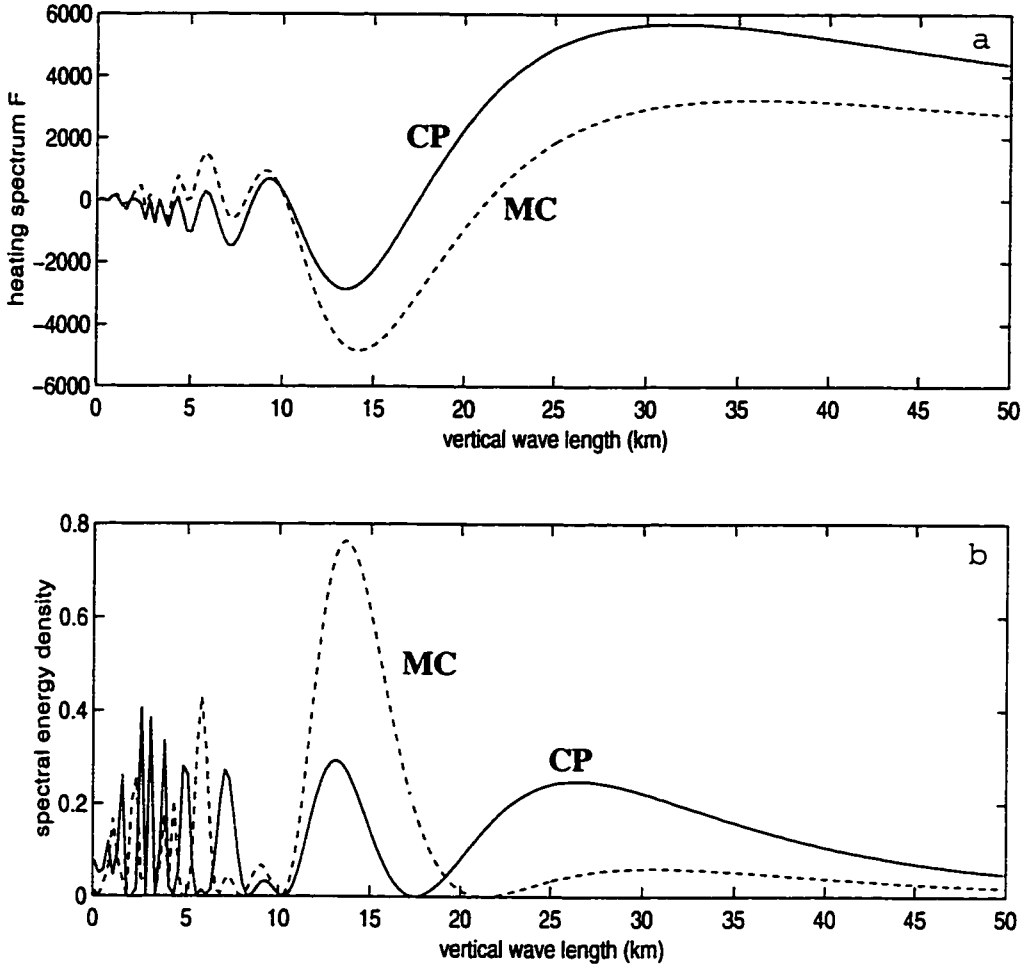

Figure 4.4: The projections of the external forcing functions (the dotted lines in Fig. 4.3) onto the vertical eigenfunctions. Panel a is the spectra $F(l)$, and panel b is the spectral energy density of the heating with respect to vertical wavelength l. The solid lines are for the CP case; and the dashed lines are for the MC case.

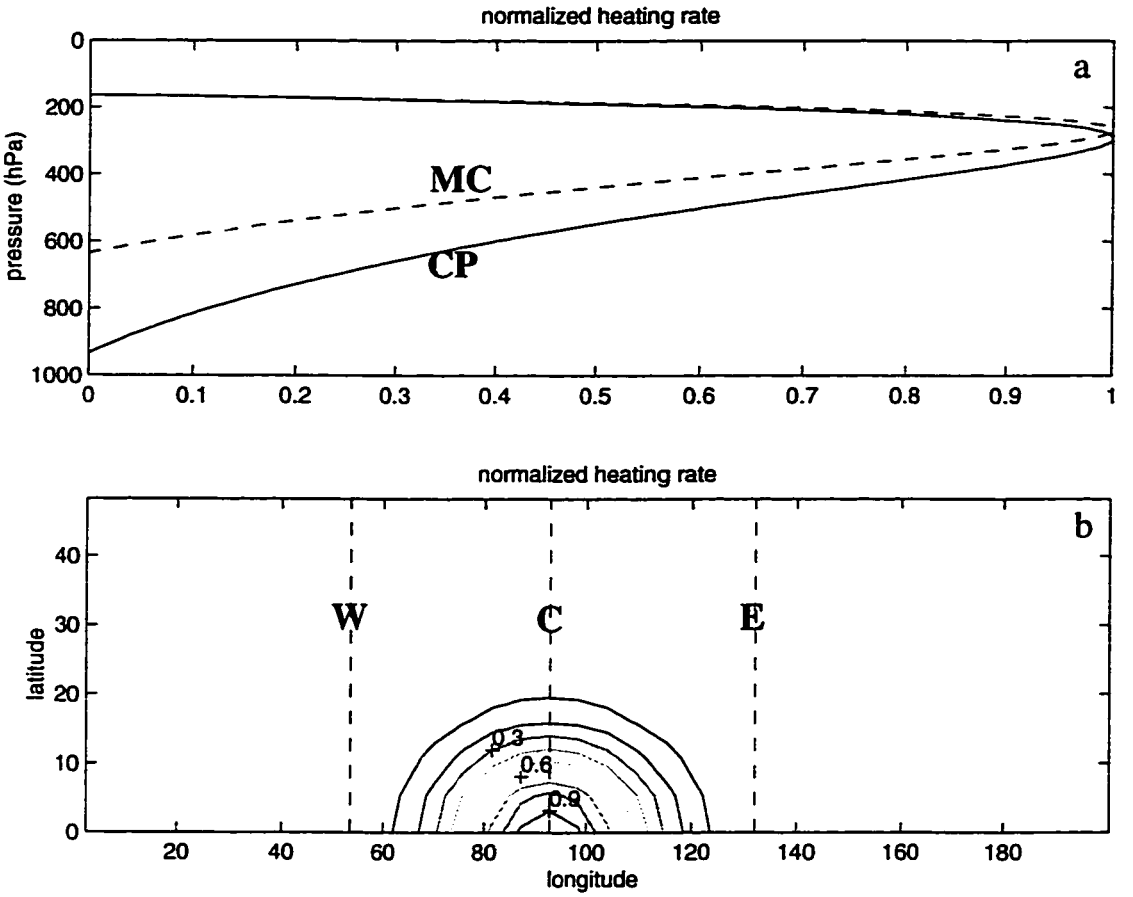

Figure 4.5: Distribution of normalized heating rate in the vertical direction (panel *a*) and on the horizontal plane (panel *b*). In panel *a*, the solid line is for the CP heating case and the dashed line is for the MC heating case, respectively. In panel *b*, the solid lines represent the normalized heating rate, the dashed lines show the locations where the physical fields are analyzed later: W, C, and E are the longitudes $53.4°E$, $92.8°E$, and $132.2°E$, respectively.

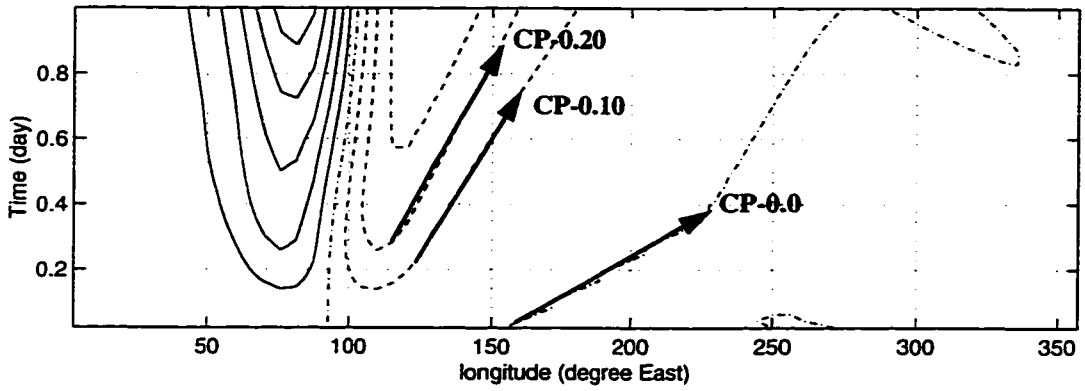

Figure 4.6: The zonal velocity along the equator for the CP case at 810 hPa level throughout the first day of the spin-up processes. The contour interval is 0.10 ms^{-1}. The solid lines represent westerlies; the dashed lines represent easterlies; and the dash-dotted lines are zero contour lines. The meaning of the superposed bold arrows are discussed in the text.

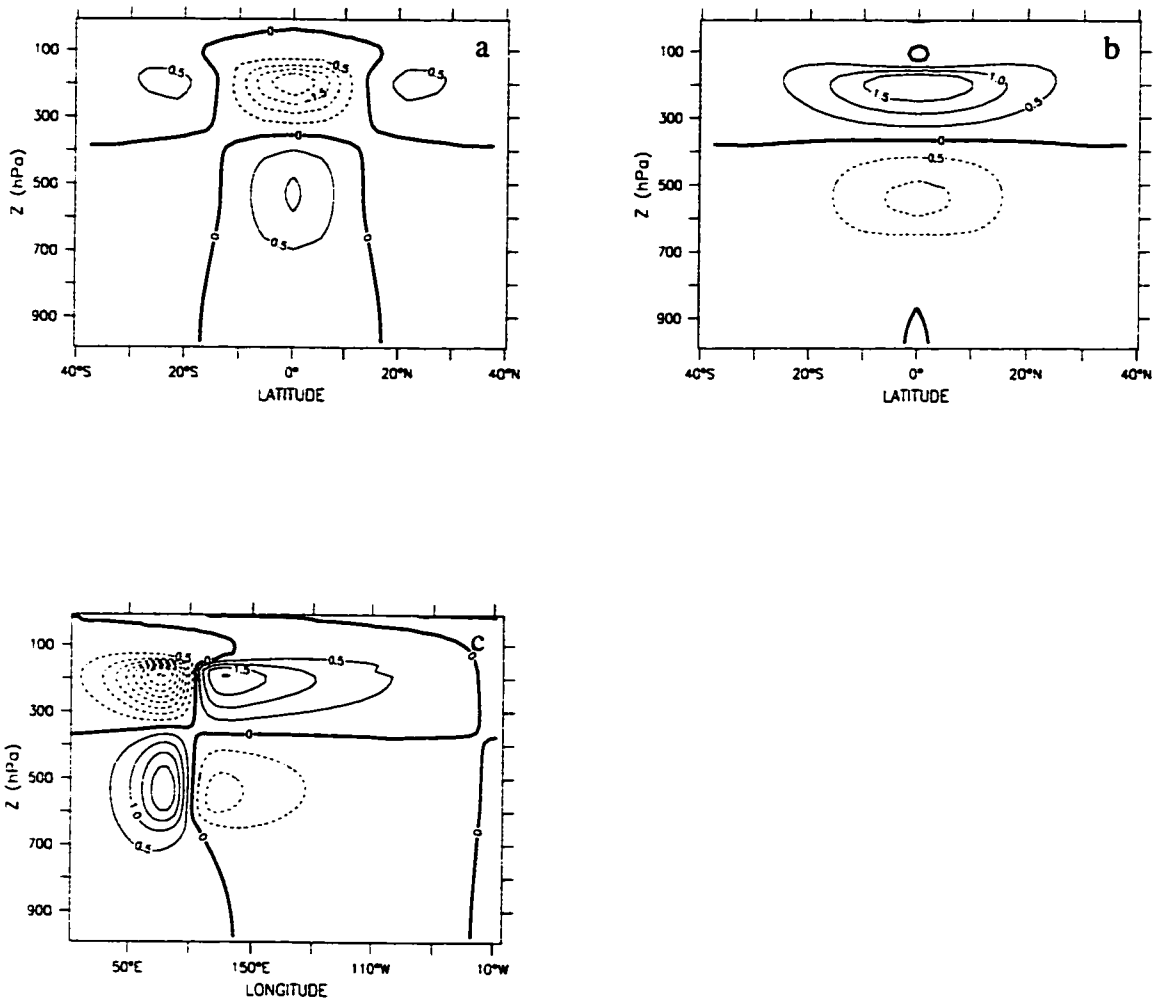

Figure 4.7: Zonal velocities at different locations for the MC case. Panel a is at $53.4°E$ (to the west of the heating); panel b is at $132°E$ (to the east of the heating); and panel c is at the Equator. The contour interval is 0.5 ms^{-1}. Westerlies are represented by the solid lines and easterlies are represented by dashed lines.

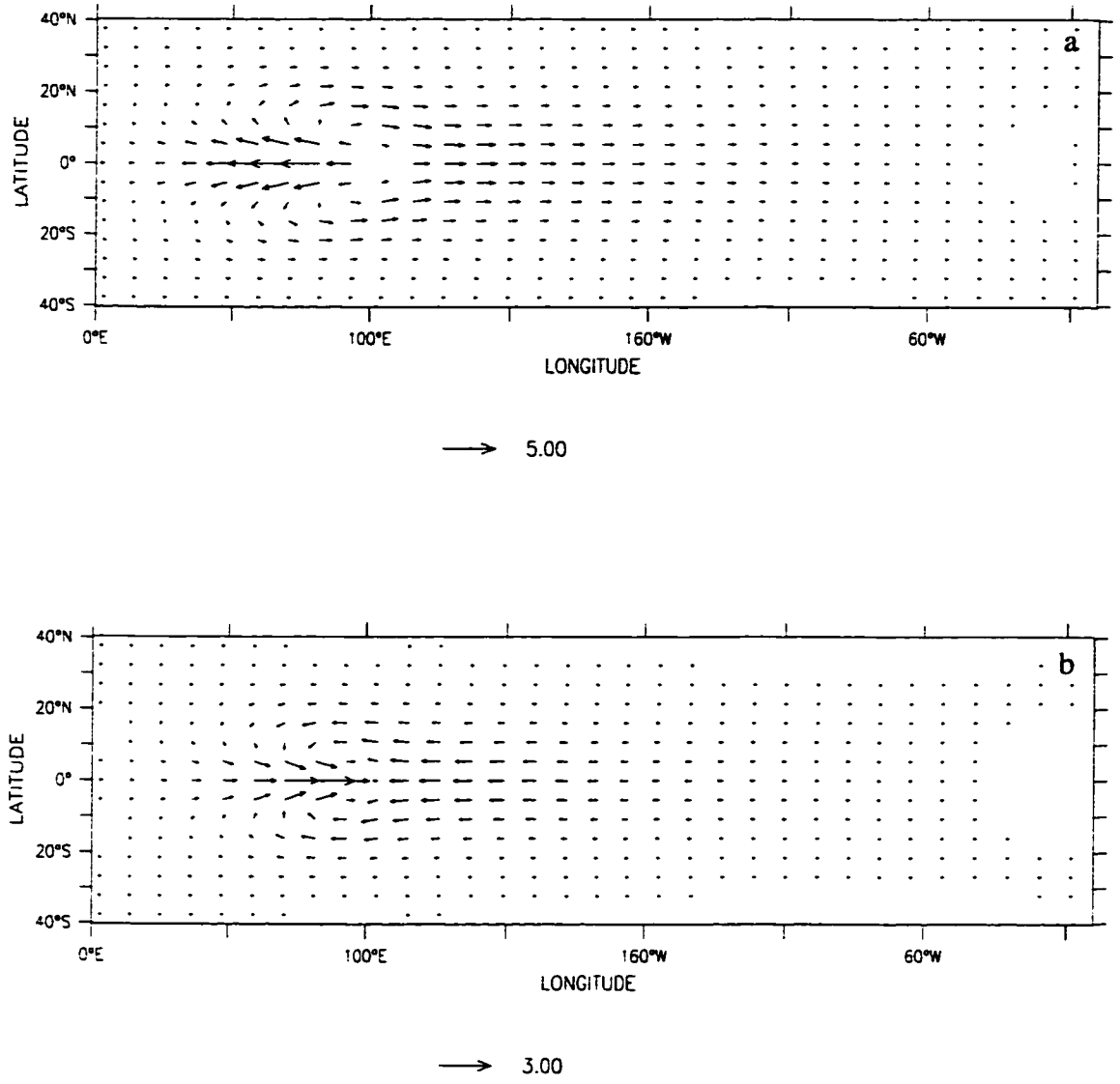

Figure 4.8: The horizontal velocities at 190 hPa (panel *a*) and at 560 hPa (panel *b*) for the MC case. The scaling vectors are shown under each panel. The unit of the velocity is ms^{-1}.

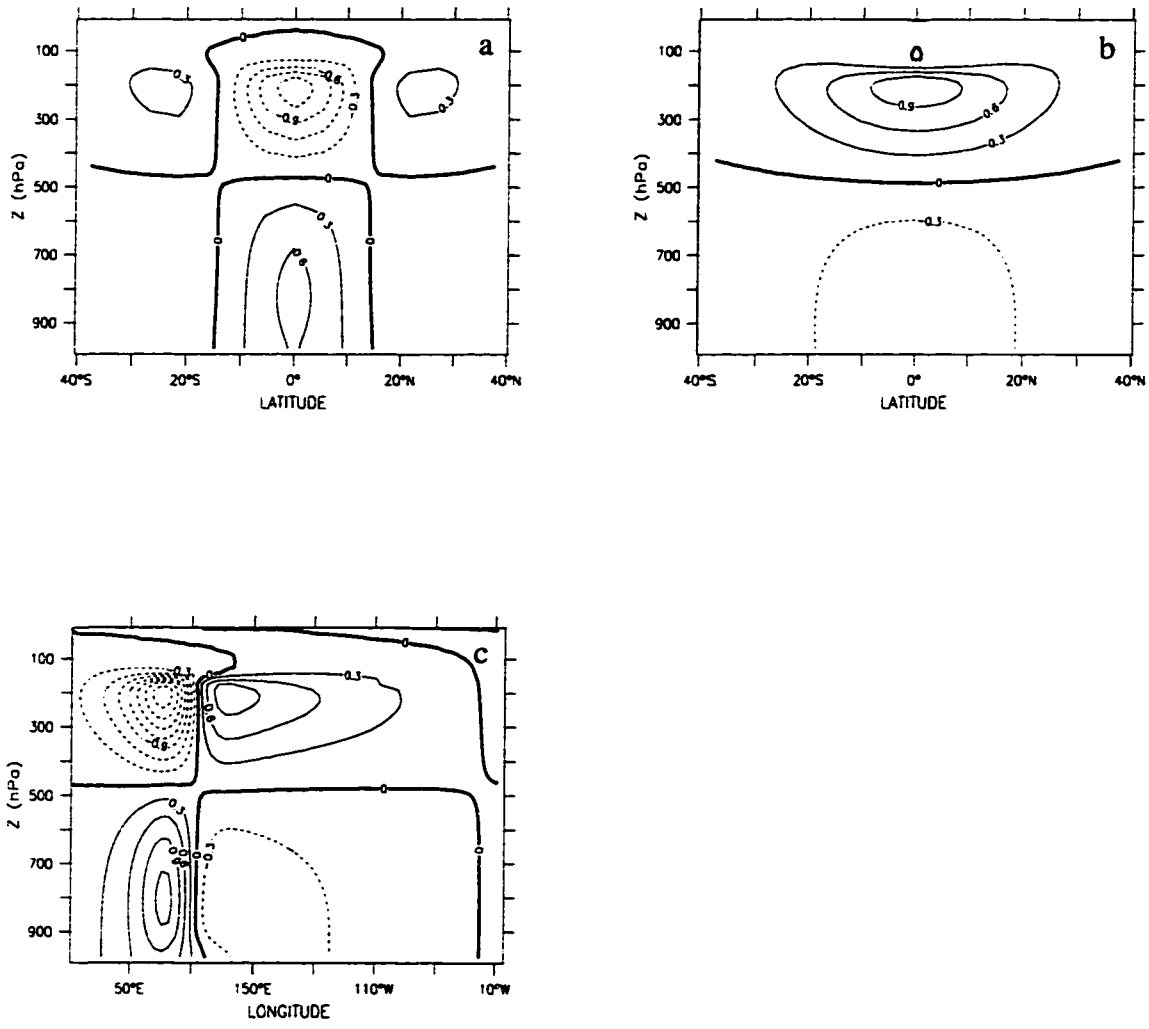

Figure 4.9: Zonal velocities at different locations for the CP case. Panel a is at $53.4°E$ (to the west of the heating); panel b is at $132°E$ (to the east of the heating); and panel c is at the Equator. The contour interval is 0.3 ms^{-1}. Westerlies are represented by the solid lines and easterlies are represented by dashed lines.

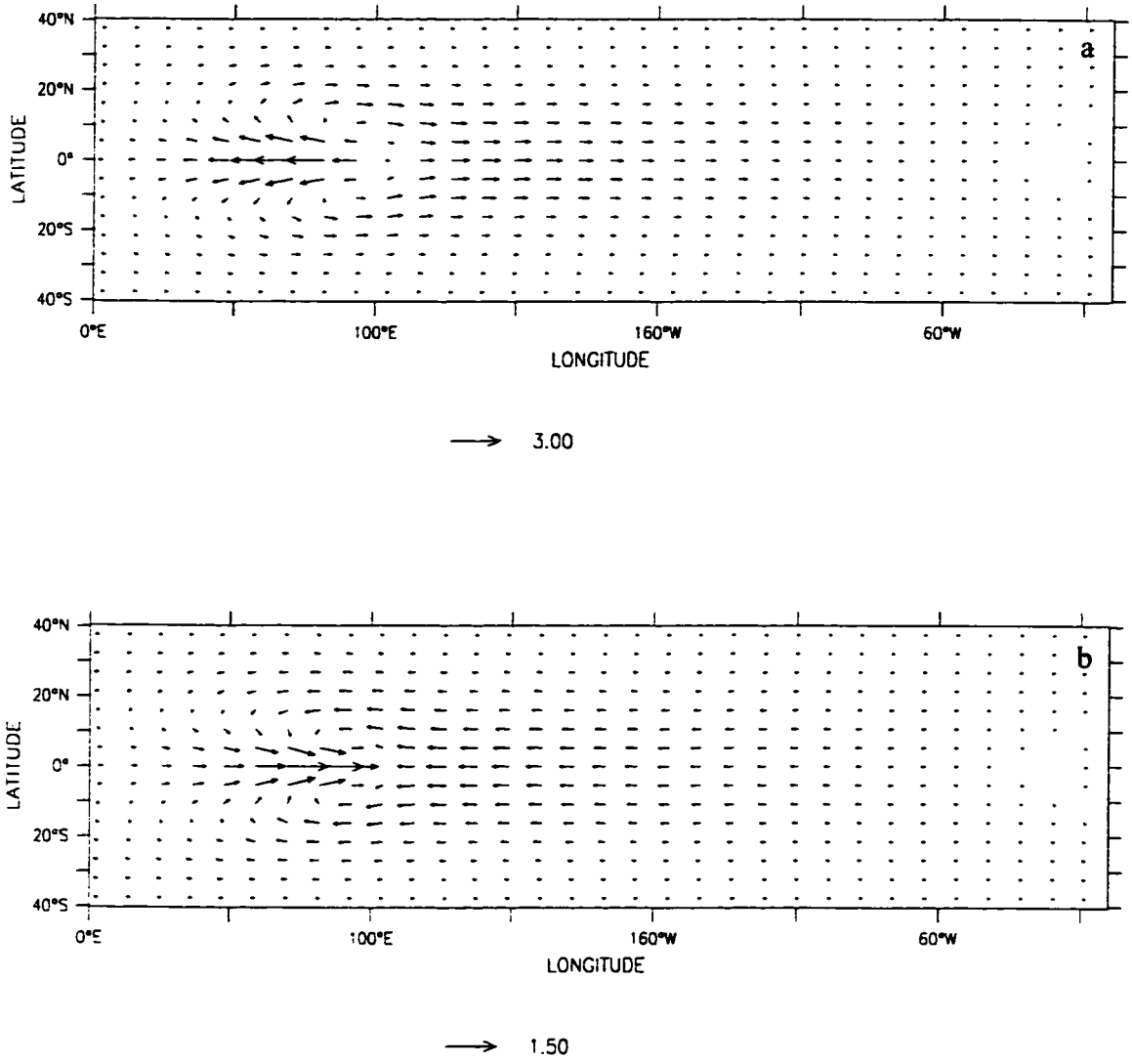

Figure 4.10: The horizontal velocities at 210 hPa (panel *a*) and at 810 hPa (panel *b*) for the CP case. The scaling vectors are shown under each panel. The unit of the velocity is ms^{-1}.

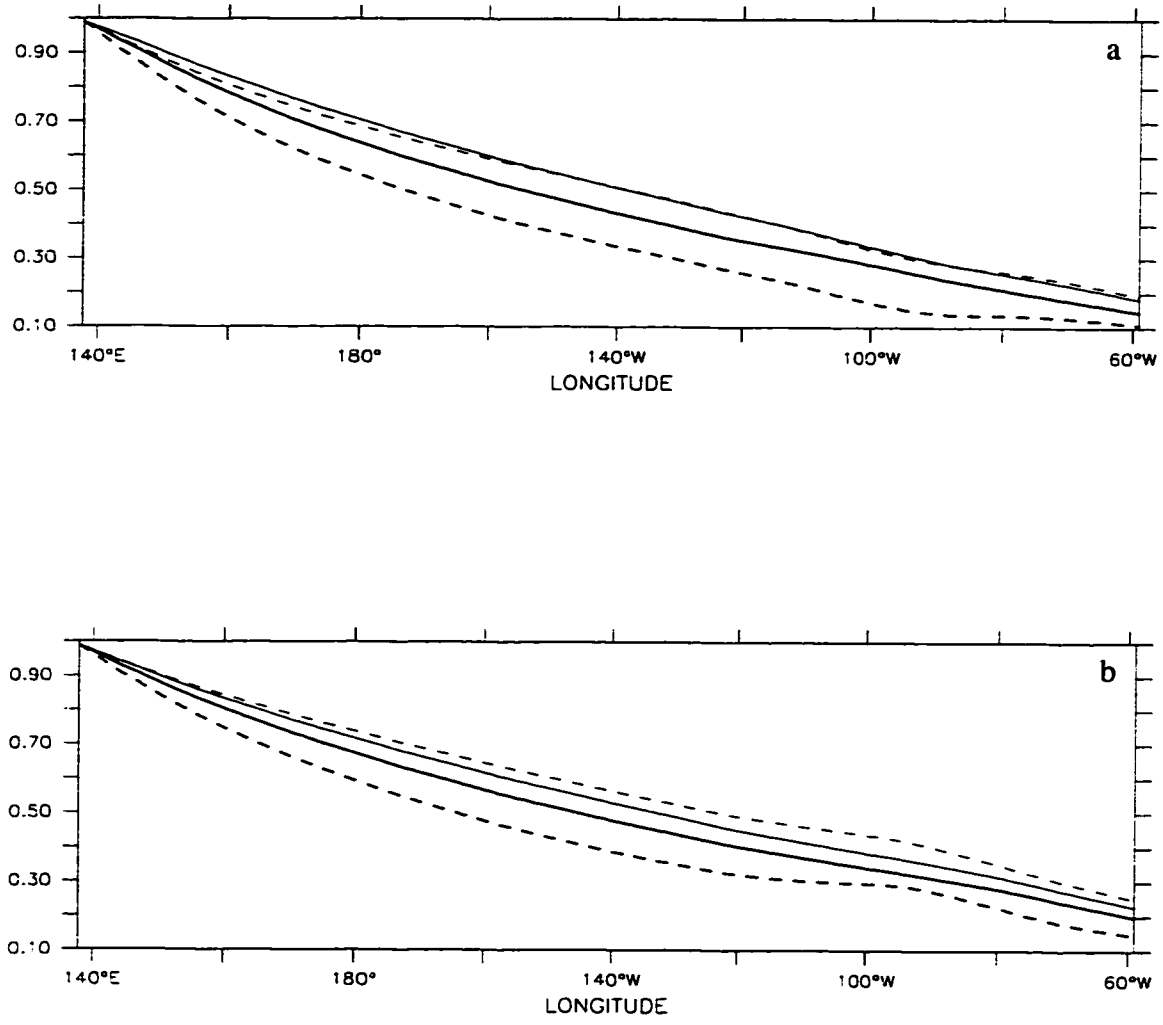

Figure 4.11: The scaled zonal velocities along the equator (panel *a*) and along $10.7°N$ (panel *b*) relative to the zonal velocities at $137.8°E$ at the same latitude and height. In each panel, the thin solid line and thin dashed line correspond to the heights of 210 hPa and 810 hPa for the CP case, respectively; the bold solid line and bold dashed line correspond to the heights of 190 hPa and 560 hPa for the MC case, respectively.

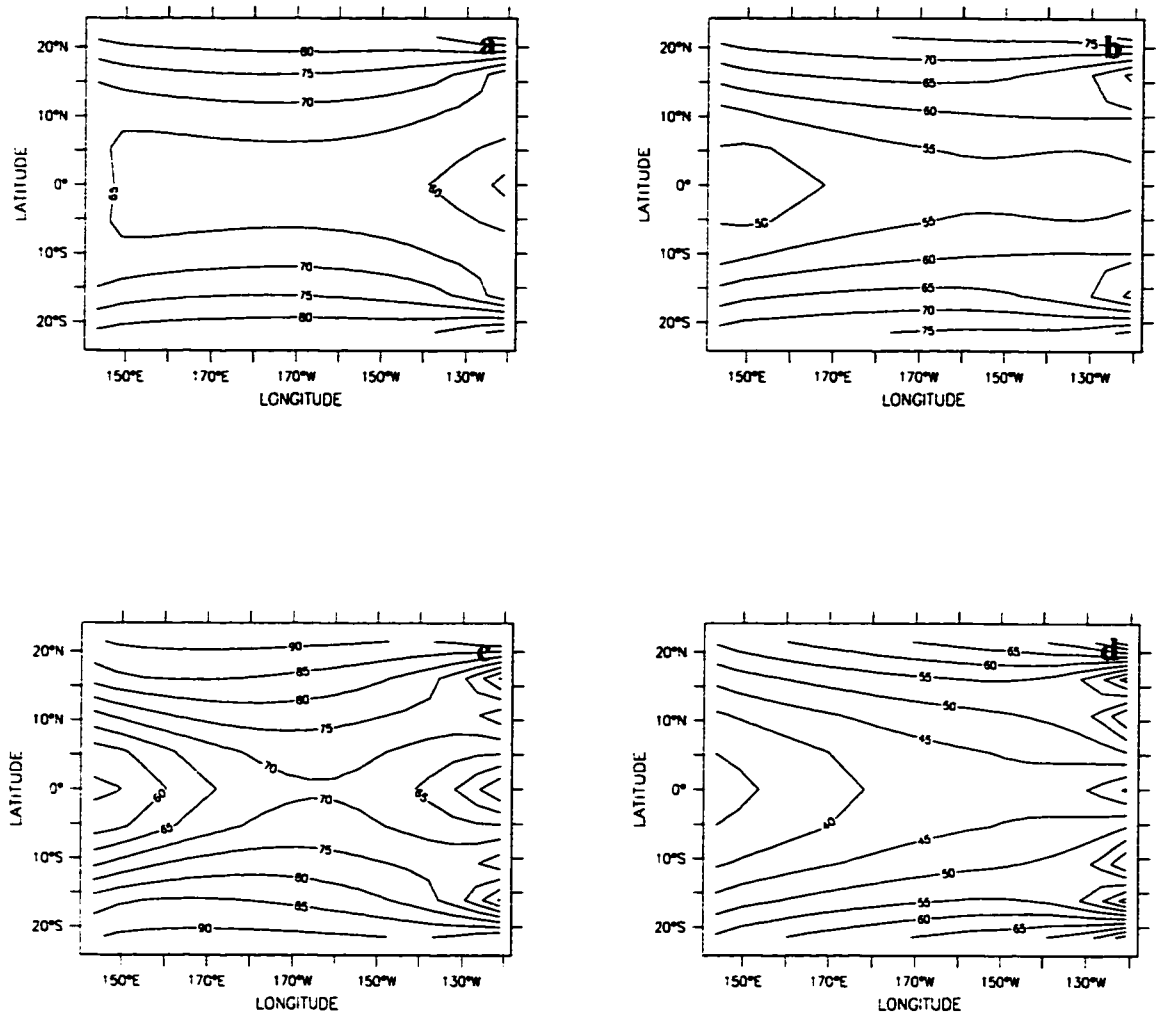

Figure 4.12: Effective gravity wave speed at different levels for the CP case (panel *a* at 210 hPa; and panel *c* at 810 hPa) and for the MC case (panel *b* at 190 hPa; and panel *d* at 560 hPa). The contour interval is 10 ms^{-1}.

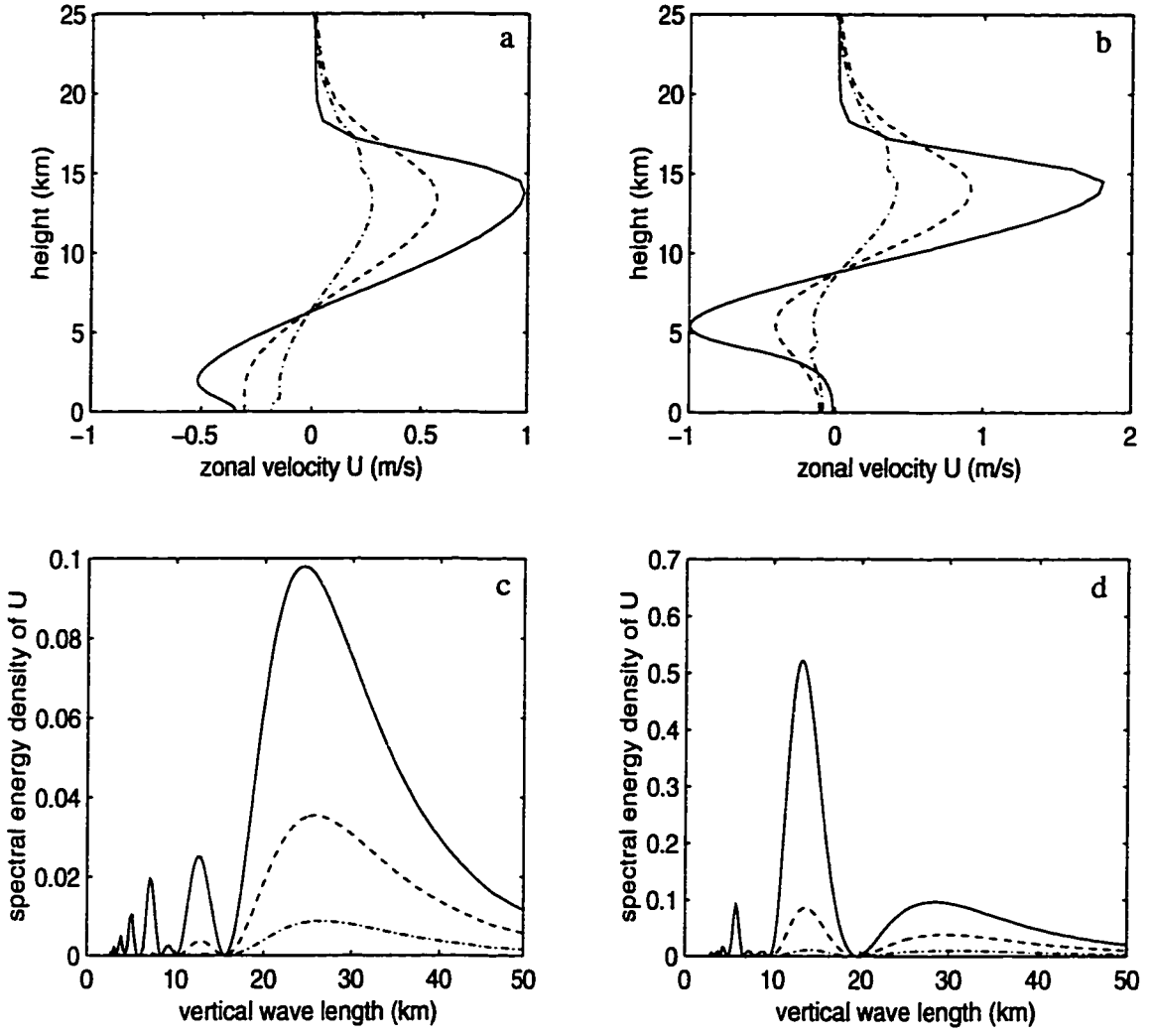

Figure 4.13: The zonal velocities (panel *a* for the CP case and panel *b* for the MC case) and their spectral energy densities (panel *c* for the CP case and panel *d* for the MC case) in the spectral space for the mass-weighted zonal velocities at different longitudes at the Equator. Solid lines are for $143.4°E$; dashed lines are for $149.1°W$; and dash-dotted lines are for $81.8°W$.

Chapter 5

RAYLEIGH FRICTION, NEWTONIAN COOLING, AND THE HORIZONTAL STRUCTURES OF THERMALLY FORCED CIRCULATIONS

5.1. Introduction

Rayleigh friction and Newtonian cooling are simple idealizations of physical processes in the atmosphere and ocean, such as nonlinear effects (Holton and Cotton 1972), eddy viscosity and eddy diffusivity (McCreary 1981). The ratio between Rayleigh friction and Newtonian cooling, called the Prandtl number (Pr), is an important quantity comparing the relative importance of momentum damping and thermal damping.

5.1.1. Previous Studies of the Role of Dissipation

Lindzen (1968) investigated the behavior of vertically propagating waves in an atmosphere with Newtonian cooling taken to be very small near the ground and increasing inversely with atmospheric density away from the ground. His results demonstrated that the amplitude of the divergence ($\partial u/\partial x + \partial v/\partial y$) does not vary with height at high altitudes where Newtonian cooling becomes very strong. Dickinson and Geller (1968) further showed that the method used in Lindzen (1968) can be applied to the tidal problem using Newtonian cooling with a more complex vertical structure. Shapiro (1977) examined the importance of boundary layer friction for thermally forced gravity and Rossby waves. Chang (1977) explored thermally driven low-frequency oscillations in the tropics in the presence of both Rayleigh friction and Newtonian cooling (both having the same damping time scale). He demonstrated that inclusion of simple linear damping has a strong influence at low frequencies on the forced equatorial waves, resulting in a different

dispersion relationship from that without dissipation. Haarsma and Opsteegh (1989), through their study of the circulations driven by the thermal sources in the tropics, showed that the Rayleigh friction affects the mid-latitude flow patterns in response to the tropical heating and it affects the transition threshold from linear to nonlinear regime. Kato (1997) used a global linear shallow-water model to show that the flow patterns driven by a propagating solar-insolation-like heat source are sensitively dependent on Rayleigh friction rather than Newtonian cooling.

The influence of eddy viscosity on oceanic waves in tropics has also been explored by many researchers. Among them, Martinsen and Weber (1981), through a decomposition of variables in terms of the vertical normal modes, examined the influence of eddy viscosity on internal Kelvin waves; Mofjeld (1981), using a shallow water model, investigated free internal wave solutions in the presence of linear (Rayleigh) friction in the equatorial waveguide. The latter study demonstrated that at low frequencies: 1) friction makes the meridional scale of the equatorial wave guide significantly larger than the inviscid scale; 2) there is relatively little zonal damping of Kelvin, inertial-gravity, and Rossby waves.

One study that systematically explored the roles of Rayleigh friction and Newtonian cooling in the tropics was Yamagata and Philander (1985). In their study, Yamagata and Philander showed that, for the steady shallow water system, the original coordinates (x, y) can be transformed into new coordinates (X, Y) $(x = (\alpha/\gamma)^{1/2}X$, $y = (\alpha/\gamma)^{1/4}Y)$, with appropriate scalings on the independent variables, such that the original shallow water system with differing values for the Rayleigh friction rate and the Newtonian cooling rate $(Pr \neq 1)$ can be transformed into the standard shallow water system with identical values for the Rayleigh friction rate and the Newtonian cooling rate $(Pr = 1)$ in the new coordinates (X, Y). From these results, they further inferred that

the zonal damping scale for the Kelvin signal in the original coordinates is characterized by the inverse of $\sqrt{\alpha\gamma}$, where α is the Rayleigh friction rate and γ is the Newtonian cooling rate. They also performed numerical studies using a nonlinear shallow water model for different combinations of Rayleigh friction rate and Newtonian cooling rate in a rectangle domain with rigid lateral boundaries. Unfortunately, since their focus was on the oceanic response to basin-wide wind stress and they could not eliminate the effect of the strong coastal Kelvin waves in their numerical experiments, their results can not be easily applied to the atmosphere forced by an isolated thermal source in the tropics.

5.1.2. Problems to Solve

Recently, Wu et al. (1998a) studied the different roles of Rayleigh friction and Newtonian cooling in a thermally forced tropical atmosphere, both numerically using a dry primitive-equation model and semi-analytically solving simple linear models. Some of their results, especially the vertical structure of the forced response, will be discussed in detail in Chapter 6. The focus in this chapter will be on the steady response of the shallow water system to a prescribed local heating for different combinations of Rayleigh friction and Newtonain cooling. In section 5.2, we will present some numerical results of the horizontal wind fields in the cases in which either Rayleigh friction or Newtonian cooling serves as the only dissipation. In section 5.3, an analytic method for solving a locally forced shallow water system in a zonally cyclic domain is developed. Calculation of the circulation driven by the heating with the same horizontal structure but using different dampings will be carried out in section 5.4. The implications of the present study will be discussed and a summary will be presented in section 5.5.

5.2. The Numerical Results

We use the same dry primitive-equation model as is described in section 2.3 to study the different surface responses to the same heating under different dissipation. Integrations are performed using the Rayleigh friction rate $\alpha^{-1} = 10$ days in the Rayleigh-friction-alone case and the Newtonian cooling rate $\gamma^{-1} = 2.5$ days in the Newtonian-cooling-alone case. The horizontal structures discussed in the following are not sensitive to the selected values of the Rayleigh friction rate and the Newtonian cooling rate as long as the maximum heating rate is comparable to that of the observed.

In this modeling study, the prescribed heating has the following three-dimensional structure:

$$Q = \exp(-(\lambda-\lambda_0)^2/\lambda_L^2)\exp(-\phi^2/\phi_L^2)F(p), \tag{5.1}$$

where λ is longitude, λ_0 is a reference longitude with the value of $93°E$, $\lambda_L = 20°$, ϕ is latitude, and $\phi_L = 11°$. The horizontal structure of the heating is exactly the same as was prescribed in last chapter and is shown in Fig. 4.5*b*. The vertical profile of the heating $F(p)$ is slightly different from the last chapter and is as follows:

$$F(p) = \begin{cases} 0 & p \geq p_b \\ F_0 \sin\left(\dfrac{p-p_t}{p_b-p_t}\pi\right) & p_t < p < p_b \\ 0 & p \leq p_t \end{cases}, \tag{5.2}$$

where, p is pressure, p_t is the pressure at the top of the heating, p_b is the pressure at the bottom of the heating. The cloud top is assumed at 160 hPa, and cloud base is at 840 hPa. F_0 is the maximum heating rate such that F corresponds to 10 mm of precipitation

per day. The cloud base taken in this chapter is somewhat higher than observed in the tropical western Pacific (840 hPa vs. the observed 940 hPa; see Mapes and Houze (1995)) so as to clearly illuminate the vertical structure of the flow in the region extending below the heating to the surface.

Fig. 5.1 shows the horizontal wind fields at 760 hPa in the Rayleigh-friction-alone case in which Rayleigh friction serves as the only dissipation, and in the Newtonian-cooling-alone case in which Rayleigh friction is the unique dissipative mechanism. It is obvious that in both cases, the forced flows in the lower half of the troposphere are easterly almost everywhere and are quite uniform zonally except in a very narrow zone along the equator outside the heating longitudes. In the Newtonian-cooling-alone case, the driven flows are confined to the heating latitudes, while in the Rayleigh-friction-alone case, the driven flows resemble a Gaussian shape in the meridional direction with a meridional Gaussian scale of about 60 degrees except in a very narrow zone along the equator.

Clearly, the above results can hardly be explained by the classical Gill model in a zonally infinite domain that predicts the Kelvin signal to the east of the heating and Rossby signals to the west of the heating. In the following sections, we will search for the reasons why the horizontal winds have such structures.

5.3. The Solution to a Shallow-Water System

It is convenient to convert the shallow water equations (4.5a-c) into a non-dimensional form. The units of time, length, geopotential, and forcing are as follows:

$$[T] = \sqrt{1/(\beta\sqrt{gh_m})},\ [L] = \sqrt{\sqrt{gh_m}/\beta},\ [\Phi] = [L]^2/[T]^2,\ \text{and}\ [F] = [L]^2/[T]^3,$$

where $\sqrt{\sqrt{gh_m}/\beta}$ is the equatorial radius of deformation, an intrinsic scale of the shallow water system. Using these units, one obtains the nondimensional form of the frictional shallow water equations for the steady case:

$$\alpha u - yv = -\frac{\partial \Phi}{\partial x}, \tag{5.3a}$$

$$\alpha v + yu = -\frac{\partial \Phi}{\partial y}, \tag{5.3b}$$

$$\gamma \Phi + \left(\frac{\partial u}{\partial x} + \frac{\partial v}{\partial y}\right) = -F. \tag{5.3c}$$

All the variables in (5.3a-c) are defined in a zonally cyclic domain. In the meridional, the boundary conditions are assumed to be $u, v, \Phi \to 0$ at $y \to \pm\infty$. Combining equations (5.3a-c) leads to a single equation of variable v:

$$\left[\frac{\partial^2}{\partial y^2} + \frac{\partial^2}{\partial x^2} + \frac{1}{\alpha}\frac{\partial}{\partial x}\right]v - \frac{\gamma}{\alpha}[y^2 + \alpha^2]v = \frac{1}{\alpha}\left[y\frac{\partial}{\partial x} - \alpha\frac{\partial}{\partial y}\right]F. \tag{5.4}$$

Equation (5.4) can be solved by using the method of separation of variables. The corresponding meridional eigenfunction $\psi_n(y)$ has the form:

$$\psi_n(y) = \exp\left(-\frac{y^2}{2R^2}\right)H_n\left(\frac{y}{R}\right), \tag{5.5}$$

which satisfies the differential equation:

$$\frac{d^2\psi_n}{dy^2} + \left[\frac{(2n+1)}{R^2} - \frac{y^2}{R^4}\right]\psi_n = 0, \tag{5.6}$$

where $R = (\alpha/\gamma)^{1/4}$ is called the non-dimensional effective equatorial radius of deformation of the frictional shallow water system, H_n are the class of Hermite polynomials, and n is a non-negative integer. The corresponding effective radius of deformation of the shallow water system with different damping rates for Rayleigh friction and Newtonian cooling ($Pr \neq 1$) in dimensional form is therefore the equatorial radius of deformation multiplied by the fourth root of the ratio between the Rayleigh friction rate and Newtonian cooling rate, i.e., $(\alpha/\gamma)^{1/4}\sqrt{\sqrt{gh_m}/\beta}$.

The set $\{\psi_n(y)\}$ is complete and orthogonal. Some of the recursive relations are:

$$R^2\frac{d\psi_n}{dy} + y\psi_n = 2nR\psi_{n-1}, \tag{5.7a}$$

and

$$R^2\frac{d\psi_n}{dy} - y\psi_n = -R\psi_{n+1}. \tag{5.7b}$$

5.3.1. Zonal Structure Equations

To simplify the mathematics, we assume a semi-geostrophic balance, with the eastward flow balancing the pressure gradient. As pointed out by Gill (1980), this approximation is equivalent to making a "long wave" approximation in the transient problem. Thus, equation (5.3b) becomes:

$$yu = -\frac{\partial \Phi}{\partial y}. \tag{5.8}$$

Next, following Gill (1980), we introduce two new variables:

$$q = \sqrt{\alpha}u + \sqrt{\gamma}\Phi, \tag{5.9a}$$

and

$$r = \sqrt{\gamma}\Phi - \sqrt{\alpha}u. \tag{5.9b}$$

Combining equations (5.3a) and (5.3c) leads to the equations for the new variables:

$$\sqrt{\alpha}q + \frac{1}{\sqrt{\gamma}}\frac{\partial q}{\partial x} - yv + \sqrt{\frac{\alpha}{\gamma}}\frac{\partial v}{\partial y} = -\sqrt{\frac{\alpha}{\gamma}}F, \tag{5.10a}$$

and

$$\sqrt{\alpha}r - \frac{1}{\sqrt{\gamma}}\frac{\partial r}{\partial x} + yv + \sqrt{\frac{\alpha}{\gamma}}\frac{\partial v}{\partial y} = -\sqrt{\frac{\alpha}{\gamma}}F, \tag{5.10b}$$

while equation (5.8) can be rewritten as:

$$yq + \sqrt{\frac{\alpha}{\gamma}}\frac{\partial q}{\partial y} - yr + \sqrt{\frac{\alpha}{\gamma}}\frac{\partial r}{\partial y} = 0. \tag{5.10c}$$

Expanding all q, r, v and F in terms of the meridional eigenfunctions $\psi_n(y)$, i.e.,

$$\begin{bmatrix} q \\ r \\ v \\ F \end{bmatrix} = \sum_n \begin{bmatrix} q_n(x) \\ r_n(x) \\ v_n(x) \\ f_n(x) \end{bmatrix} \psi_n(y), \tag{5.11}$$

and substituting equations (5.11) into equations (5.10a-c), one obtains (cf. Gill (1980) for the case in which the Rayleigh friction rate and the Newtonian cooling rate are identical):

$$\sqrt{\alpha}\sum_n q_n\psi_n + \frac{1}{\sqrt{\gamma}}\sum_n \frac{dq_n}{dx}\psi_n - y\sum_n v_n\psi_n + \sqrt{\frac{\alpha}{\gamma}}\sum_n v_n\frac{d\psi_n}{dy} = -\sqrt{\frac{\alpha}{\gamma}}\sum_n f_n\psi_n, \tag{5.12a}$$

$$\sqrt{\alpha}\sum_n r_n\psi_n - \frac{1}{\sqrt{\gamma}}\sum_n \frac{dr_n}{dx}\psi_n + y\sum_n v_n\psi_n + \sqrt{\frac{\alpha}{\gamma}}\sum_n v_n\frac{d\psi_n}{dy} = -\sqrt{\frac{\alpha}{\gamma}}\sum_n f_n\psi_n, \tag{5.12b}$$

and

$$y\sum_n q_n\psi_n + \sqrt{\frac{\alpha}{\gamma}}\sum_n q_n\frac{d\psi_n}{dy} - y\sum_n r_n\psi_n + \sqrt{\frac{\alpha}{\gamma}}\sum_n r_n\frac{d\psi_n}{dy} = 0, \tag{5.12c}$$

respectively. Using the recursion relationships (5.7a-b) and the orthogonality of $\psi_n(y)$, one obtains:

$$\frac{dq_n}{dx} + \sqrt{\alpha\gamma}q_n = -\sqrt{\alpha}f_n + (\alpha\gamma)^{\frac{1}{4}}v_{n-1}, \tag{5.13a}$$

$$\frac{dr_n}{dx} - \sqrt{\alpha\gamma}r_n = \sqrt{\alpha}f_n + 2(n+1)(\alpha\gamma)^{\frac{1}{4}}v_{n+1}, \tag{5.13b}$$

and

$$2(n+1)q_{n+1} - r_{n-1} = 0. \tag{5.13c}$$

After manipulating equations (5.13a-c), one obtains:

$$\frac{dq_0}{dx} + \sqrt{\alpha\gamma}q_0 = -\sqrt{\alpha}f_0, \tag{5.14a}$$

$$q_1 = 0, \tag{5.14b}$$

$$\frac{dq_{n+1}}{dx} - (2n+1)\sqrt{\alpha\gamma}q_{n+1} = \frac{\sqrt{\alpha}}{2}(f_{n-1} + 2nf_{n+1}) \quad \text{for} \quad n \geq 1, \tag{5.14c}$$

$$(\alpha\gamma)^{\frac{1}{4}}v_0 = \sqrt{\alpha}f_1, \tag{5.14d}$$

$$(\alpha\gamma)^{\frac{1}{4}}v_n = 2(n+1)\sqrt{\alpha\gamma}q_{n+1} + (n+1)\sqrt{\alpha}f_{n+1} + \frac{\sqrt{\alpha}}{2}f_{n-1} \quad \text{for} \quad n \geq 1, \tag{5.14e}$$

$$r_{n-1} = 2(n+1)q_{n+1} \quad \text{for} \quad n \geq 1. \tag{5.14f}$$

Thus only the variables q_n, for non-negative n, are defined by ordinary differential equations of the first order; all other variables v_n and r_n are only arithmetic combinations in terms of the sets $\{q_n\}$ and $\{f_n\}$.

5.3.2. The Green's Function in the Zonal Direction

Equations (5.14a) and (5.14c) are solved in a zonally cyclic domain. It is common to use Fourier series to represent all the variables and the forcing and then determine the coefficients. Here, we use the Green's function method to obtain the solutions to equa-

tions (5.14a) and (5.14c). The Green's function method $G_n(x, x_0)$ is defined by the following equation:

$$\frac{dG_n(x, x_0)}{dx} + l_n G_n(x, x_0) = \delta(x - x_0), \tag{5.15}$$

where $x \in (0, C]$ is any position in a cyclic domain, C is the length of a cyclic domain, $l_n = \sqrt{\alpha\gamma}$ for $n = 0$, and $l_n = -(2n-1)\sqrt{\alpha\gamma}$ for $n > 1$. When $C \to \infty$, the zonally cyclic domain becomes the zonally unbounded domain. In equation (5.15), G_n is differentiable everywhere except $x = x_0$ where an amplitude jump happens. For this reason, the Green's function G_n in equation (5.15) is defined as the following:

$$G_n(x, x_0) = \begin{cases} \tilde{G}_n(x, x_0) & for\ C \geq x > x_0 \\ \tilde{G}_n(x + C, x_0) & for\ 0 < x < x_0 \end{cases}, \tag{5.16}$$

where $\tilde{G}_n(x, x_0)$ is defined in the domain $x \in (x_0, x_0 + C]$ and is differentiable everywhere. This definition of the Green's function $G_n(x, x_0)$ is illustrated in Fig. 5.2. Hence, the amplitude jump condition becomes:

$$\tilde{G}_n(x_0, x_0) - \tilde{G}_n(x_0 + C, x_0) = 1. \tag{5.17}$$

From equations (5.15-17), one obtains:

$$G_n(x, x_0) = \begin{cases} \dfrac{\exp[-l_n(x - x_0)]}{1 - \exp(-l_n C)} & for\ C \geq x > x_0 \\ \dfrac{\exp[-l_n(x + C - x_0)]}{1 - \exp(-l_n C)} & for\ 0 < x < x_0 \end{cases} . \qquad (5.18)$$

The solutions to equations (5.14a) and (5.14c) are therefore expressed as:

$$q_0(x) = \int_0^C G_0(x, x_0)[-\sqrt{\alpha} f_0(x_0)]dx_0 \qquad (5.19a)$$

and

$$q_{n+1}(x) = \int_0^C G_{n+1}(x, x_0)\frac{\sqrt{\alpha}}{2}[f_{n-1}(x_0) + 2n f_{n+1}(x_0)]dx_0 \quad \text{for} \quad n \geq 1 . \qquad (5.19b)$$

5.4. The Response to an Isolated Heat Source

In this section, solutions to the shallow water system in a zonally cyclic domain and in a zonally infinite domain will be found for various combinations of Rayleigh friction and Newtonian cooling. We will illustrate how the solutions are affected by the dissipation, the zonal domain, and the vertical heating structure (represented by the gravity wave speed). Since the scaling factors $[L]$ and $[T]$ are different for different vertical modes, we select three different set of units that correspond to the vertical modes with the gravity wave speeds of 20 ms^{-1}, 28 ms^{-1}, 60 ms^{-1}, respectively. Although these values are arbitrarily selected, the gravity wave speeds of 20 ms^{-1} and 60 ms^{-1} are typical for communicating the response of the system (see, Fig 5.3) to a heat source whose vertical structure is given by equation (5.2) and by Fig. 5.3b. Some of the scaling values are listed in Table 1.

Table 5.1. Scaling units for different vertical modes. The first column is the gravity wave speeds of the modes; the second column is the length scales (in degrees); the third column is the time scales (in days); the fourth column is the nondimensional Earth's circumference in terms of the length scales; and the fifth column is the nondimensional damping rate corresponding to 1/(4 days).

$\sqrt{gh_m}$ (m/s)	$[L_m]$ (deg.)	$[T_m]$ (day)	$[C_m]$	damping rate
20.0	8.4	0.53	42.9	0.133
28.2	10.0	0.46	36.0	0.114
60.0	14.6	0.31	24.7	0.078

To compare directly with the simple solutions in Gill (1980), the external forcing is prescribed slightly differently from what is expressed by equation (5.1) in the zonal direction. The horizontal structure of the heating in this section has the form:

$$F(x, y) = f(x) \cdot \exp\left(-\frac{y^2}{2Y^2}\right), \tag{5.20}$$

where Y is 1100 km (corresponding to $10°$ of latitude) and:

$$f(x) = \begin{cases} \cos\left(\dfrac{x - x_0}{x_r - x_l}\pi\right) & x_l \le x \le x_r \\ 0 & 0 < x < x_l \text{ or } C \ge x > x_r \end{cases}, \tag{5.21}$$

where x_l, x_0, x_r correspond to the longitudes $80°E$, $100°E$, $120°E$, respectively, and C is the circumference of the Earth.

Four categories of damping cases are examined: 1) *the strong-damping cases* in which the damping time scales for Rayleigh friction and Newtonian cooling are prescribed as 4 days; 2) *the weak-damping cases* in which the damping time scales for Rayleigh friction and Newtonian cooling are prescribed as 10 days; 3) *the Rayleigh-friction-dominant cases* in which the damping time scale is 10 days for Rayleigh friction and 100 days for Newtonian cooling; and 4) *the Newtonian-cooling-dominant cases* in which the damping time scale is 1000 days for Rayleigh friction and 10 days for Newtonian cooling. Since the solutions in a zonally cyclic domain may differ significantly to those in a zonally infinite domain, we will carry out the calculations in both types of zonal domains for each case. The cases that will be analyzed in the following are listed in Table 2.

Table 5.2. The list of parameters for each case. The second column is the gravity wave speeds of the modes; the third column is the damping time scales for Rayleigh friction; the fourth column is the damping time scales for Newtonian cooling; and the fifth column is the domain types for each case.

	$\sqrt{gh_m}$ (ms^{-1})	$1/\alpha$ (days)	$1/\gamma$ (days)	Zonal Domain
CASE I	28.2	4.0	4.0	cyclic
CASE II	20.0	4.0	4.0	cyclic
CASE III	60.0	4.0	4.0	cyclic
CASE IV	60.0	4.0	4.0	unbounded
CASE V	60.0	10.0	10.0	cyclic
CASE VI	60.0	10.0	10.0	unbounded
CASE VII	60.0	100.0	100.0	cyclic
CASE VIII	60.0	1000.0	10.0	cyclic
CASE IX	60.0	10.0	100.0	unbounded
CASE X	60.0	1000.0	10.0	unbounded

5.4.1. Responses under Strong Damping

Fig. 5.4 illustrates the solutions for Case I. In this case, the external forcing projects only onto the zero order parabolic cylinder function. The horizontal structure of response is almost identical to Fig. 1 in Gill (1980), which is anticipated since the selected parameters for this case are almost identical to those given in Gill (1980) provided that 10° is taken as the equivalent to one spacial unit in Gill (1980). In a zonally infinite domain, Gill (1980) showed that the nondimensional forms of u and Φ are identical to the east of the heating. In a zonally cyclic domain, if damping is strong enough, one would expect the same. This is clearly true in Fig. 5.4c since in this case, the fastest propagating Kelvin signal with a propagation speed of 28.2 ms^{-1} takes about 16 days to travel along the Earth's circumference, while the damping time is 4 days.

Fig. 5.5 are the plots for the response corresponding to a vertical mode whose horizontal gravity wave speed is 20 ms^{-1} (Case II). In this case, the forcing projects onto higher order parabolic cylinder functions as well (Fig. 5.5b). Thus, the response accounted for by the higher modes is no longer zero everywhere (see the dash-dotted line in Fig. 5.5c). The forced signals propagate at smaller speeds, their corresponding spatial decay rates are larger than those in Case I, and therefore the horizontal structure of the response (Fig. 5.5a) looks like a zonally squeezed version of Fig. 5.4a. Since the length scale $[L]$ in this case is smaller than that in the previous case, the Kelvin signal to the east of the heating has a smaller meridional scale and is more equatorial trapped.

For vertical modes of larger vertical wave length and faster horizontal propagating speed, the length scale $[L]$ is larger. The corresponding parabolic cylinder functions are also of larger meridional scales. Again, many parabolic cylinder functions are needed to

expand the forcing given by equation (5.20). The solutions in such a case (Case III) is shown in Fig. 5.6. Clearly, the forced signals cover a larger meridional extent. Since it takes less than 8 days for a Kelvin signal in this case to travel along the Earth's circumference, the eastward propagating Kelvin signal and westward propagating Rossby signals overlap in the most of the equatorial zone. This is clearer by comparing Fig. 5.6 to Fig. 5.7 (Case IV), which is the same case but using a zonally infinite domain. In Fig. 5.6, the geopotential Φ along the equator (panels c and d) is considerably flatter than in Fig. 5.7 in which a zonally infinite domain is adopted instead of a zonally cyclic domain. Since the warming signal (corresponding to negative Φ) is confined to a zonally cyclic domain in Case III, the amplitude of the warming signal in Case III is larger than that in Case IV.

5.4.2. Responses under Weak dissipation

When dissipation is weak, the forced signals can propagate farther away from the heating region before they are damped. In a cyclic domain, this means that a forced signal may still keep a large enough amplitude after it travels along the Earth's circumference and returns to the excitation region. Fig. 5.8 features the solutions for a vertical mode whose horizontal gravity wave speed is 60 ms^{-1} (Case V) in the presence of weak dissipation. By comparing panels a and c of Fig. 5.8 with panels a and c of Fig. 5.6, one sees that the easterly winds from 30° to 40° latitude (mainly contributed by the modes corresponding to $\psi_0(y)$ and $\psi_2(y)$) is much stronger in Case V than in Case III. The geopotential at the equator (Fig. 5.8b) and at different longitudes (Fig. 5.8d) also shows that their zonal decay rates are very small and the geopotential is almost zonally uniform.

In a zonally unbounded domain (Case VI, Fig. 5.9), the solutions are again very differ-

ent from those in Case V. The easterlies to the east of heating are weaker than those in case V, while the westerlies near the equator is stronger than those in case V. The geopotential is about half the amplitude of that in case V almost everywhere.

5.4.3. The Rayleigh-Friction-Dominant Case and the Newtonian-Cooling-Dominant Case

In section 5.2, we indicated that the numerical model shows that the response is almost zonally uniform but extended meridionally to the pole region when the only dissipative mechanism is Rayleigh friction. The calculation using a linear model for a Rayleigh-friction-dominant case is shown in Fig. 5.10 (Case VII). Clearly, the wind field (Fig. 5.10a) retains the most characters of Fig. 5.1a. In this case, the meridional scale (the effective equatorial radius of deformation) of the parabolic cylinder functions $\psi_n(y)$ expressed by equation (5.5) are very large. Hence, all the Kelvin signal and Rossby signals extended to high latitudes. Near the equator, the zonal wind signal associated with the Kelvin mode (with meridional structure $\psi_0(y)$) and the zonal wind signal associated with the Rossby modes are of opposite signs and cancel each other, and the net winds are easterly to the east of the heating and westerly to the west of the heating. However, in the mid-latitudes, the zonal wind signals associated with the Kelvin mode and the second Rossby modes have the same sign (see the thin solid, dashed, and dash-dotted lines in Fig. 5.10b, c), therefore, almost zonally uniform easterlies are seen. At higher latitudes, the contribution from Kelvin signal is diminishingly small, but the zonal wind signals associated with different Rossby modes (e.g., $\psi_2(y)$ and $\psi_4(y)$) have opposite signs and cancel each other. The meridional wind signals are an order smaller than the zonal wind signals almost everywhere. The geopotential, of course, is zonally uniform and meridionally extended (Fig. 5.10d).

When a smaller Newtonian cooling rate is selected, the results and arguments are essentially similar to the above case. However, the meridional scale of $\psi_n(y)$ becomes even larger. The wind field (not shown here) outside the equatorial zone looks like a meridionally stretched form of Fig. 5.10*a*.

Fig. 5.11 shows the results when Newtonian cooling is the dominant dissipative mechanism for a vertical mode whose horizontal gravity wave speed is 60 ms^{-1} (Case VIII). Fig. 5.11 catches the essence of the numerical result (Fig. 5.1*b*) from a dry primitive-equation model: the forced winds are almost zonally uniform and meridionally confined to the heating latitudes. In this case, the meridional scales (the effective equatorial radius of deformation) of the parabolic cylinder functions $\psi_n(y)$ expressed by equation (5.5) are very small. Hence, the Kelvin signal and low order Rossby signals extended to high latitudes. From Fig. 5.11*b*, one sees that the heating mainly projects onto the modes $\psi_n(y)$ with their turning points residing inside the meridional extent of the heating. Thus, the response to the heating is also accounted for by these modes and confined to the heating latitudes. Since the zonal decay rates are so small for all the Rossby modes, the zonal wind response accounted for by those Rossby modes are almost zonally uniform outside the heating longitudes (Fig. 5.11*c*), and the geopotential is zonally uniform at every latitude (Fig. 5.11*d*).

The maximum zonal winds at about 15° latitude are mainly due to the easterlies associated with $\psi_2(y)$. In a very narrow zone along the equator, the forced zonal response associated with that mode are westerly winds, which counteract the easterly winds associated with $\psi_0(y)$ and result in easterlies to the east of the heating and westerlies to the west of the heating. The effective equatorial radius of deformation of the shallow water system

becomes smaller when Rayleigh friction is weaker; therefore, the zonal wind response is a meridionally shrunken form (not shown here) of Fig. 5.11*a* with modes of larger n accounting for a slightly larger amount of the response.

The solutions for both *the Rayleigh-friction-dominant case* (Case IX) and *the Newtonian-cooling-dominant case* (Case X) in an infinite zonal domain are shown in Fig. 5.12. It is clear that the responses in both cases are significantly different from those in a zonally cyclic domain (cf Case IX with Case VII, and Case X with Case VIII). In both cases, since the effective equatorial radius of deformation is proportional to the fourth root of the Prandtl number (the ratio between Rayleigh friction rate and Newtonian cooling rate), the meridional extent of the response in the Rayleigh-friction-dominant case is much larger than in the Newtonian-cooling-dominant case.

5.5. Discussion and Summary

In this chapter, the forced shallow water system resulting from the vertical decomposition of a vertically semi-infinite atmosphere was analytically solved in the presence of different combinations of Rayleigh friction and Newtonian cooling. Both zonally cyclic and zonally infinite domains were considered to examine the sensitivity of the horizontal structure of the forced response to the various model domains. The solutions were then used to understand the numerical results from a dry primitive equation model presented in section 5.2.

The meridional extent of the forced response is characterized by the effective equatorial radius of deformation of a shallow water system with a given equivalent depth, which is the equatorial radius of deformation of the shallow water system multiplied by the fourth root of the Prandtl number (the ratio between the Rayleigh friction rate and the Newtonian cooling rate). When the values of the Rayleigh friction rate and the Newtonian

cooling rate are same, the effective equatorial radius of deformation of a shallow water system is exactly the equatorial radius of deformation of that shallow water system. Hence, the forced response covers a larger meridional domain for a shallow water system with larger equivalent depth compared to those with relatively smaller equivalent depth under external forcing of the same meridional structure. In last chapter, we showed that the deeper the heating, the larger the portion of heating energy accounted for by the modes with large equivalent depth. Hence, the deep heating implies the forced atmospheric circulation covers a large meridional extent.

When the values of the Rayleigh friction rate and the Newtonian cooling rate are different, the effective equatorial radius of deformation of a shallow water system will be very large when Rayleigh friction dominates and very small when Newtonian cooling dominates. The turning point of any single parabolic cylinder function can be outside the heating latitude in *the Rayleigh-friction-dominant case*, and therefore, the total forced response can extend to very high latitude. For *the Newtonian-cooling-dominant case*, however, almost all the parabolic cylinder functions onto which the forcing has significant projection have their turning points inside the latitudinal boundaries of the heating, and the total response is confined to the heating latitudes. The more extensive numerical results from a dry primitive equation model will be discussed in next chapter, where the implication of these results to the thermally driven surface winds in the tropics are emphasized.

The zonal decay scale of a shallow water system is characterized by the product of the gravity wave speed of the shallow water system and the damping time scale. When this product is small enough, the solutions in a zonally infinite domain can be very good approximations to the solutions in a zonally cyclic domain. Since deep thermal forcing generally projects a significant part of its energy onto the shallow water system with a relatively large gravity wave speed, a significant amount of the forced signals can propagate a

great distance along the equator before being totally damped and therefore can interfere with the signal coming from the opposite direction. In such a case, the Kelvin signal and Rossby signals can either interfere with or reinforce each other. The net results in a zonally cyclic domain are therefore, in general, different from those in an unbounded domain in which only the Kelvin signal is seen to the east of the heating and only Rossby signals are seen to the west of the heating. The damping time scale is the inverse of the square root of the product of the Rayleigh friction rate and the Newtonian cooling rate. In the cases when both Rayleigh friction and Newtonian cooling are quite weak or when either Rayleigh friction or Newtonian cooling is diminishingly small, the zonal decay scale becomes very large. Hence, the response to a zonally isolated heating is almost zonally uniform outside the heating longitudes in a zonally cyclic domain.

An interesting feature of the tropical atmosphere that has not been well explained is the zonally uniform low-frequency variation in pressure and temperature in the tropics. Barnett (1985) analyzed the variations in 200 hPa height field and showed that the variations appear coherent for the tropical belt around the entire globe. Newell and Wu (1992) found that the correlation between the tropospheric temperature in the whole tropical zone and the averaged tropospheric temperature in the tropical eastern Pacific is almost zonally uniform. Yulaeva and Wallace (1994) and Wallace et al. (1998) further observed that the warming signals are highly uniform in the zonal direction and extended meridionally. These results indicate that the locally forced warming signal exhibits little spacial decay when it propagates away from the heating region, which can hardly be explained by the structure of the classical Gill's solutions. However, in the previous sections, we have shown that deep heating projects significantly onto the fast-propagating vertical modes. For these modes, under reasonable dissipation (e.g., a damping time scale on the order of ten days), the geopotential response hardly decays in the zonal direction in a zonally cyclic domain. Hence, these observed features can somehow be explained by

the linear response of the tropical atmosphere to deep heating due to cumulus convection. However, it remains to be further examined whether the observed zonal mean signal is solely due to linear response to an isolated heat source in a zonally cyclic domain.

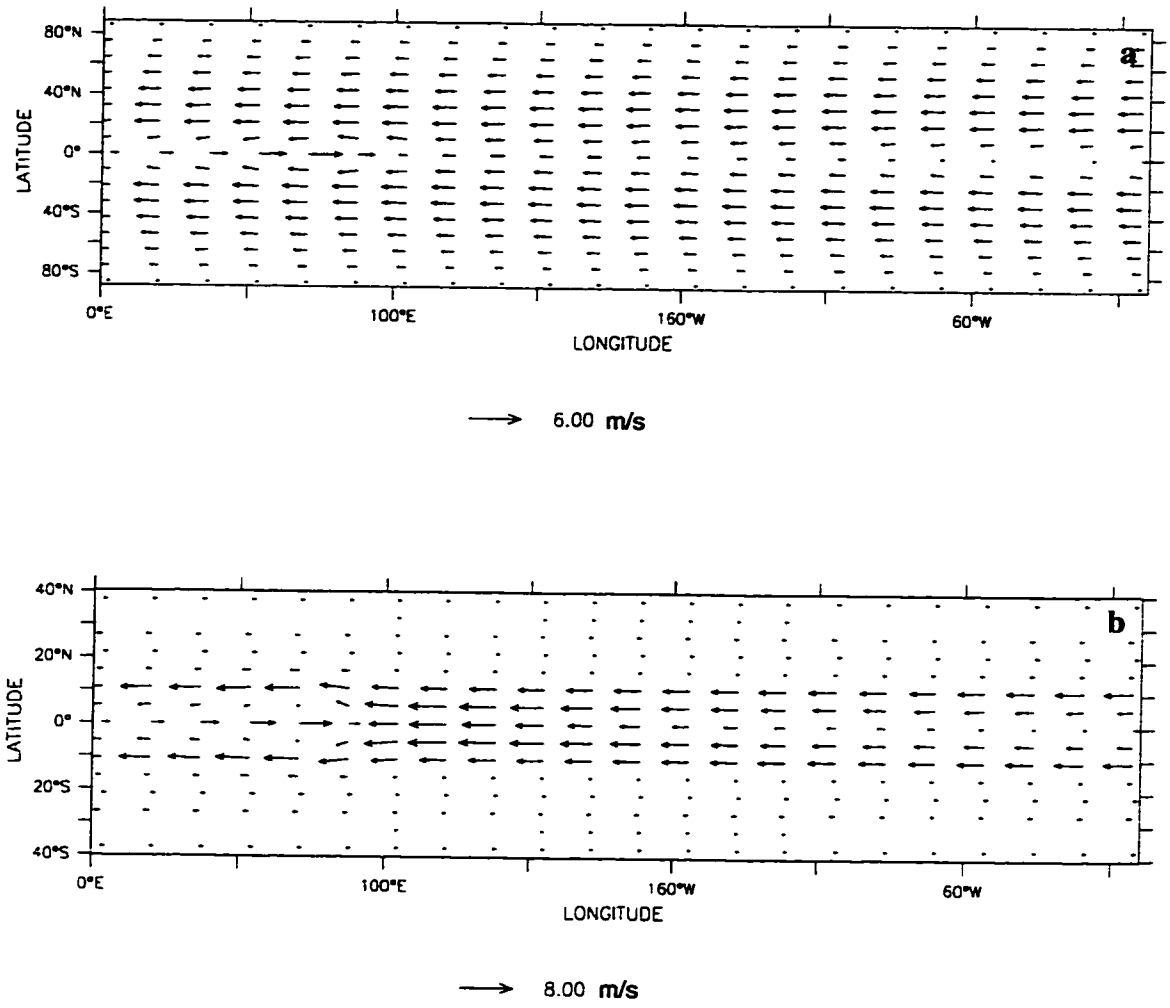

Figure 5.1: The horizontal wind fields at 760 hPa for *the Rayleigh-friction-alone-case* (panel *a*) and for *the Newtonian-cooling-alone-case* (panel *b*) in a dry primitive equation general circulation model. The scale of the horizontal velocity is shown under each panel.

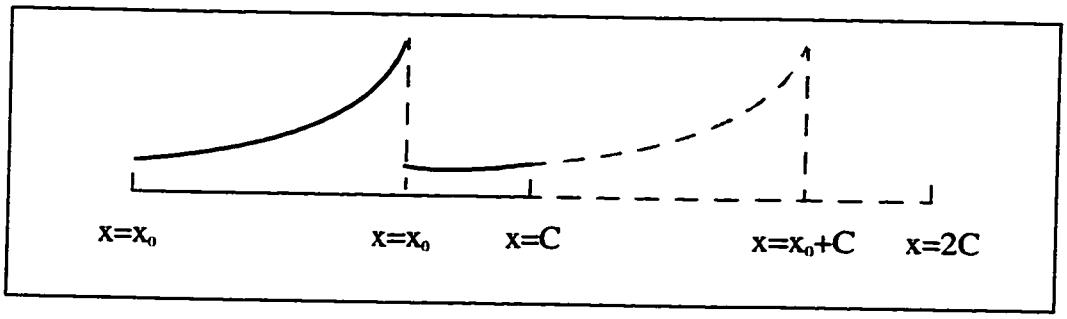

Figure 5.2: The sketch of the Green's function in a cyclic domain $x \in (0, C]$ for a linear ordinary differential equation of the first order. The domain is extended to $x \in (0, 2C]$ so as to apply the jump condition at $x = x_0$ and the differentiable requirement at $x = C$. The Green's function is represented by the bold solid line. See also the corresponding text in Appendix B.

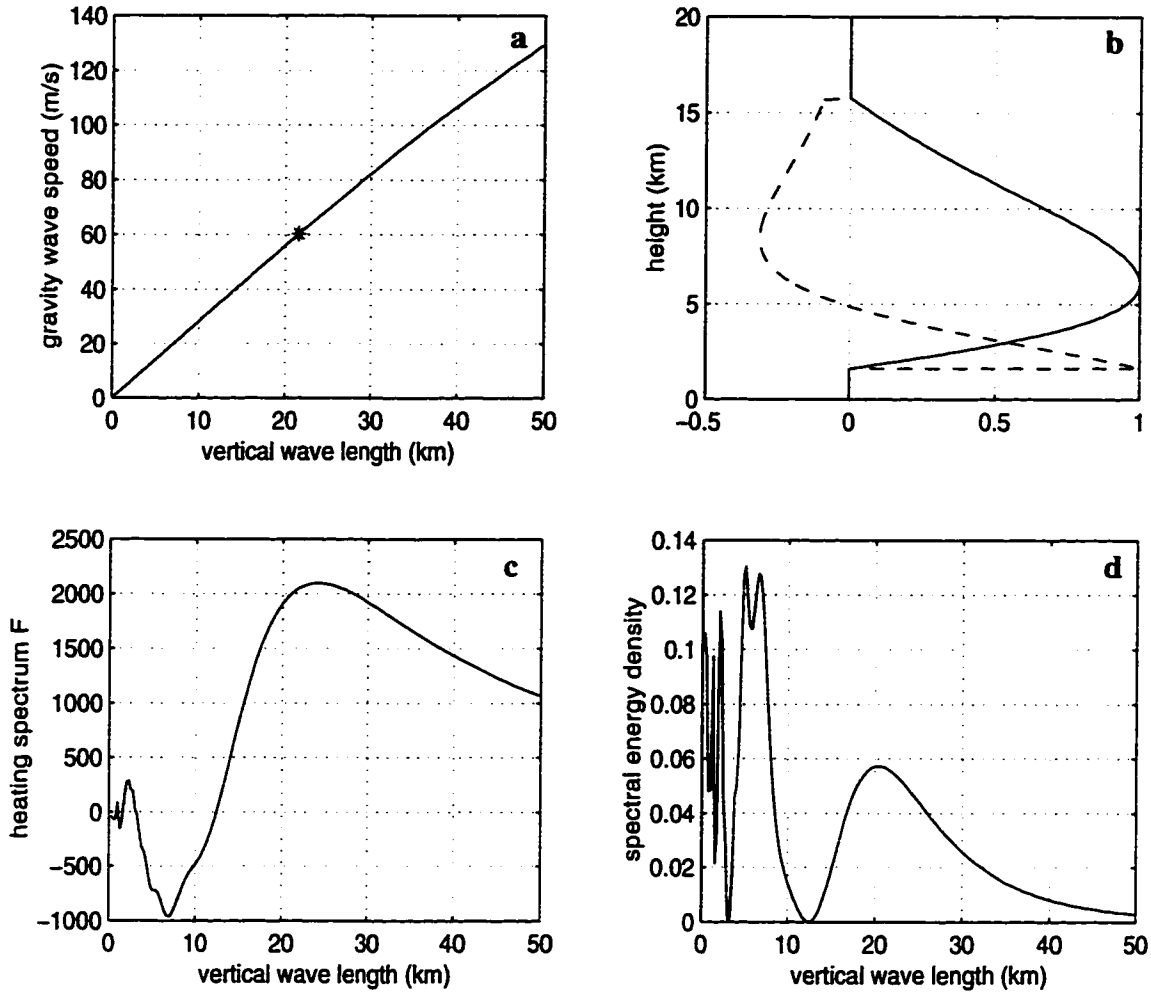

Figure 5.3: Panel a: The plot of the gravity wave speed against the vertical wave length for a baroclinic mode in an isothermal atmosphere of 300 K. The '*' point corresponds to the gravity speed of 60 ms^{-1}; Panel b: The normalized vertical heating profiles used in both the numerical modeling study and the analytical studies. The solid line represents the vertical structure of the external heating given by eqution (5.2), and the dashed line represents the corresponding vertical structure of $\tilde{Q}$ in equation (4.6); Panel c: The projection (the spectrum $F(l)$) of $P(z)$ onto the vertical eigenfunctions; Panel d: The spectral energy density of the heating with respect to vertical wavelength l. See section 4.4 for the definitions of $F(l)$, $P(z)$, and spectral energy density.

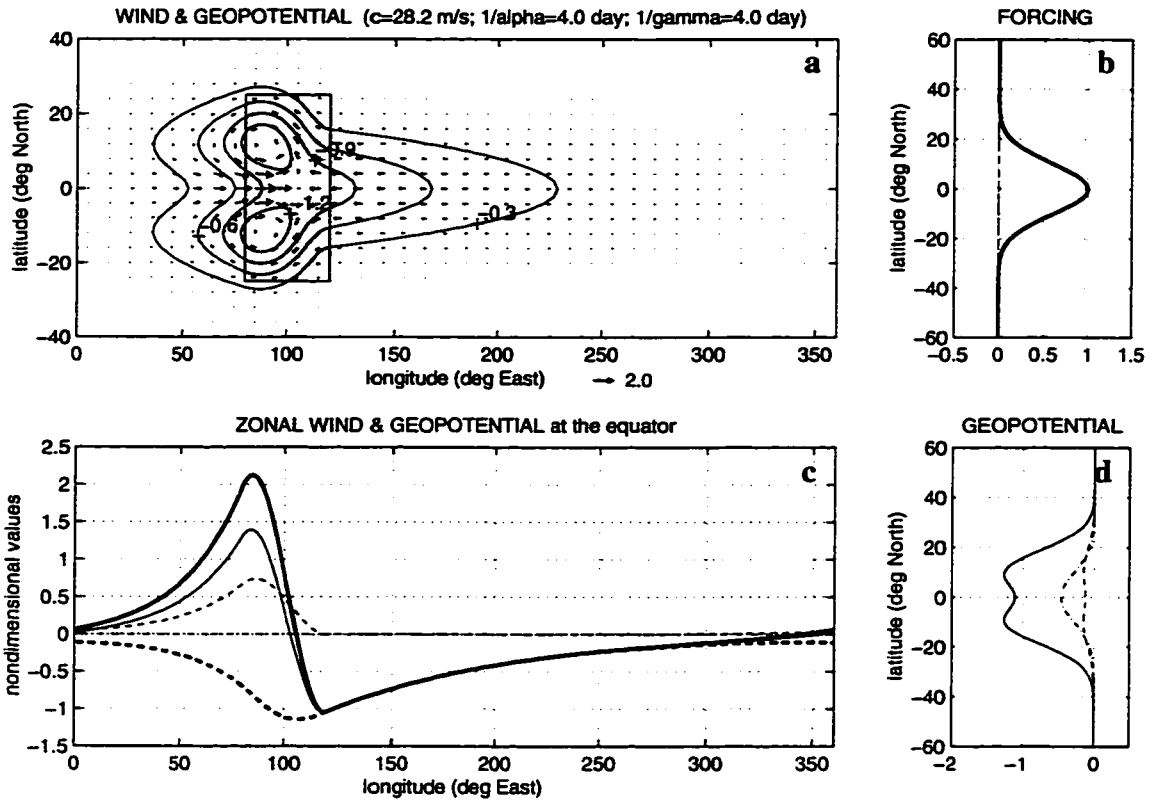

Figure 5.4: The solutions for CASE I. In panel a, the vector field (with its scale shown under the panel) of horizontal velocities are superposed on the contoured geopotential. The shaded area is where the heating happens. Panel b plots the meridional profile of the heating (the bold solid line). Note in this case, the heating only projects on to $\psi_0(y)$. Panel c plots the total zonal velocity at the equator (the bold solid line), the total geopotential at the equator (the bold dashed line), and the decomposed form of the zonal velocity at the equator (The contributions from meridional modes $\psi_0(y)$, $\psi_2(y)$,and $\psi_4(y)$ at the equator are represented by the thin solid line, the thin dashed line, and the thin dash-dotted line, respectively). Panel d plots the meridional structures of the geopotential at different longitudes (Solid line: $100°E$ corresponding to the heating center; dashed line: $10°E$; and dash-dotted line: $190°E$).

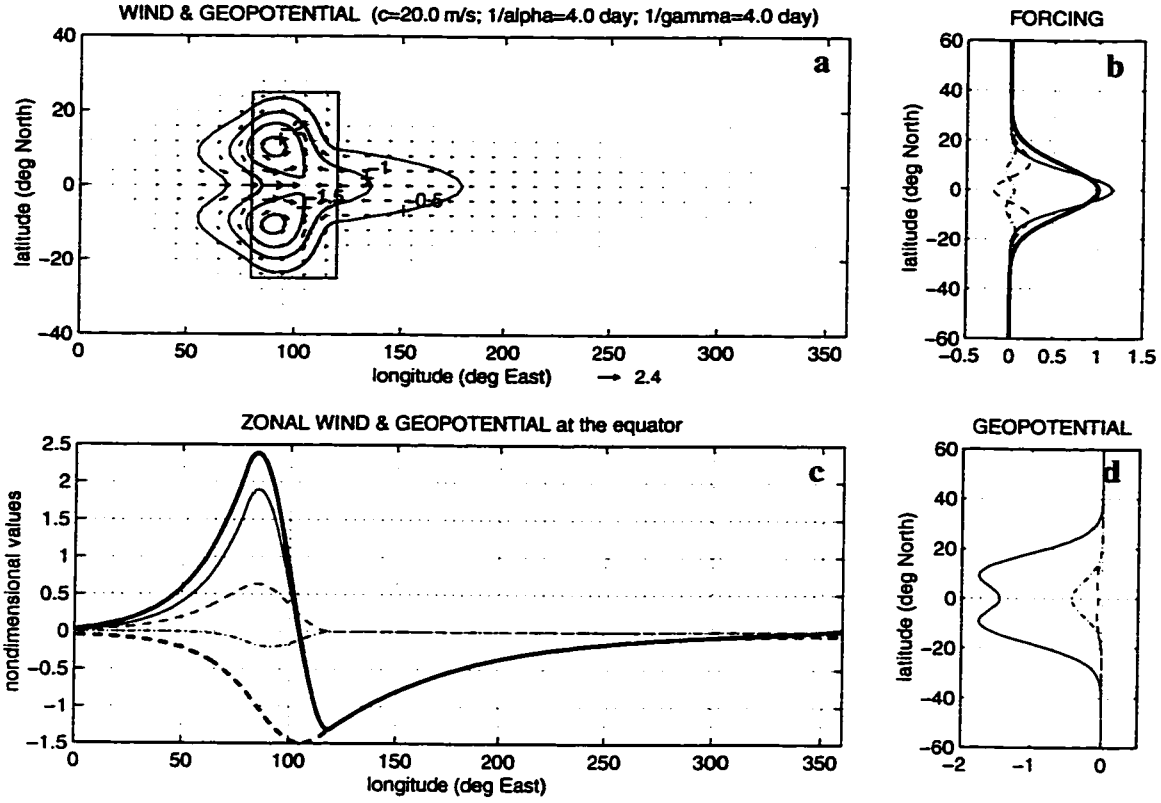

Figure 5.5: The solutions for CASE II. In panel a, the vector field (with its scale shown under the panel) of horizontal velocities are superposed on the contoured geopotential. The shaded area is where the heating happens. Panel b plots the meridional profile of the heating (the bold solid line) and its decomposed form in terms of the parabolic cylinder functions with characteristic meridional scale of the shallow water system. The parts associated with $\psi_0(y)$, $\psi_2(y)$, and $\psi_4(y)$ are shown by the thin solid line, the thin dashed line, and the thin dash-dotted line, respectively. Panel c plots the total zonal velocity at the equator (the bold solid line), the total geopotential at the equator (the bold dashed line), and the decomposed form of the zonal velocity at the equator (The contributions from meridional modes $\psi_0(y)$, $\psi_2(y)$,and $\psi_4(y)$ at the equator are represented by the thin solid line, the thin dashed line, and the thin dash-dotted line, respectively). Panel d plots the meridional structures of the geopotential at different longitudes (Solid line: $100°E$ corresponding to the heating center; dashed line: $10°E$; and dash-dotted line: $190°E$).

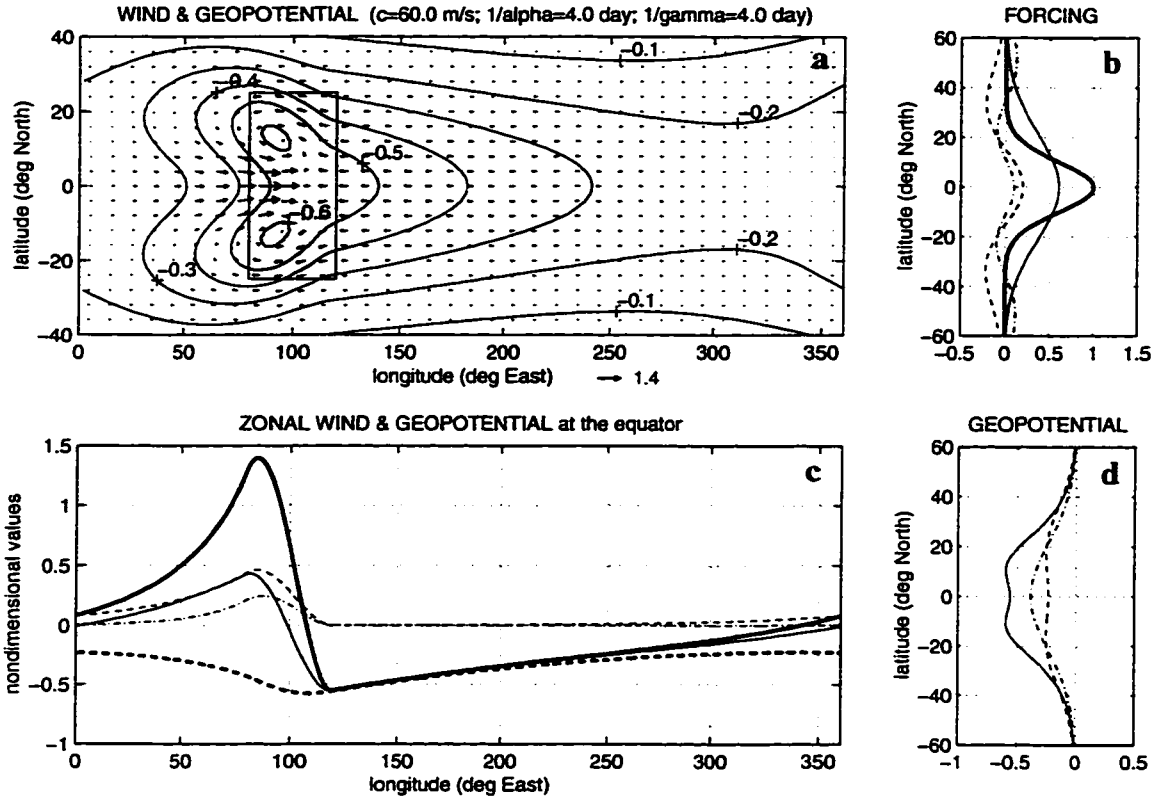

Figure 5.6: The solutions for CASE III. In panel a, the vector field (with its scale shown under the panel) of horizontal velocities are superposed on the contoured geopotential. The shaded area is where the heating happens. Panel b plots the meridional profile of the heating (the bold solid line) and its decomposed form in terms of the parabolic cylinder functions with characteristic meridional scale of the shallow water system. The parts associated with $\psi_0(y)$, $\psi_2(y)$, and $\psi_4(y)$ are shown by the thin solid line, the thin dashed line, and the thin dash-dotted line, respectively. Panel c plots the total zonal velocity at the equator (the bold solid line), the total geopotential at the equator (the bold dashed line), and the decomposed form of the zonal velocity at the equator (The contributions from meridional modes $\psi_0(y)$, $\psi_2(y)$,and $\psi_4(y)$ at the equator are represented by the thin solid line, the thin dashed line, and the thin dash-dotted line, respectively). Panel d plots the meridional structures of the geopotential at different longitudes (Solid line: $100°E$ corresponding to the heating center; dashed line: $10°E$; and dash-dotted line: $190°E$).

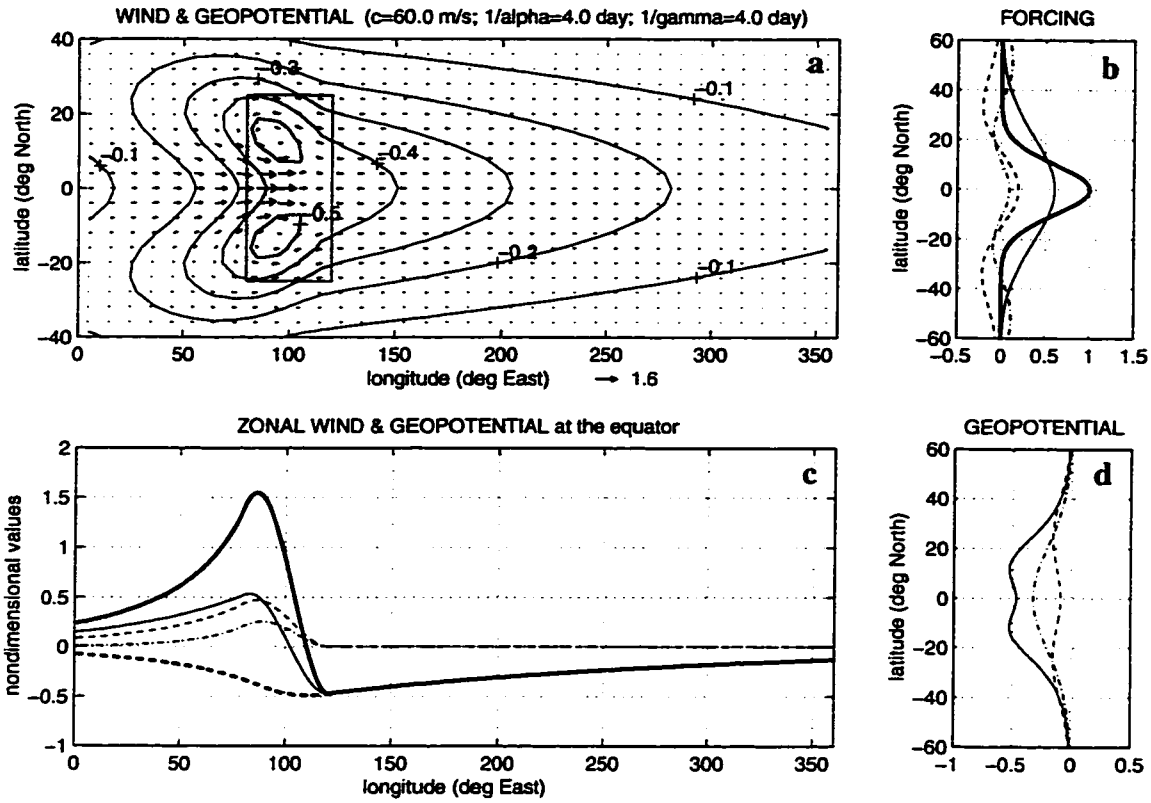

Figure 5.7: The solutions for CASE IV. In panel *a*, the vector field (with its scale shown under the panel) of horizontal velocities are superposed on the contoured geopotential. The shaded area is where the heating happens. Panel *b* plots the meridional profile of the heating (the bold solid line) and its decomposed form in terms of the parabolic cylinder functions with characteristic meridional scale of the shallow water system. The parts associated with $\psi_0(y)$, $\psi_2(y)$, and $\psi_4(y)$ are shown by the thin solid line, the thin dashed line, and the thin dash-dotted line, respectively. Panel *c* plots the total zonal velocity at the equator (the bold solid line), the total geopotential at the equator (the bold dashed line), and the decomposed form of the zonal velocity at the equator (The contributions from meridional modes $\psi_0(y)$, $\psi_2(y)$,and $\psi_4(y)$ at the equator are represented by the thin solid line, the thin dashed line, and the thin dash-dotted line, respectively). Panel *d* plots the meridional structures of the geopotential at different longitudes (Solid line: $100°E$ corresponding to the heating center; dashed line: $10°E$; and dash-dotted line: $190°E$).

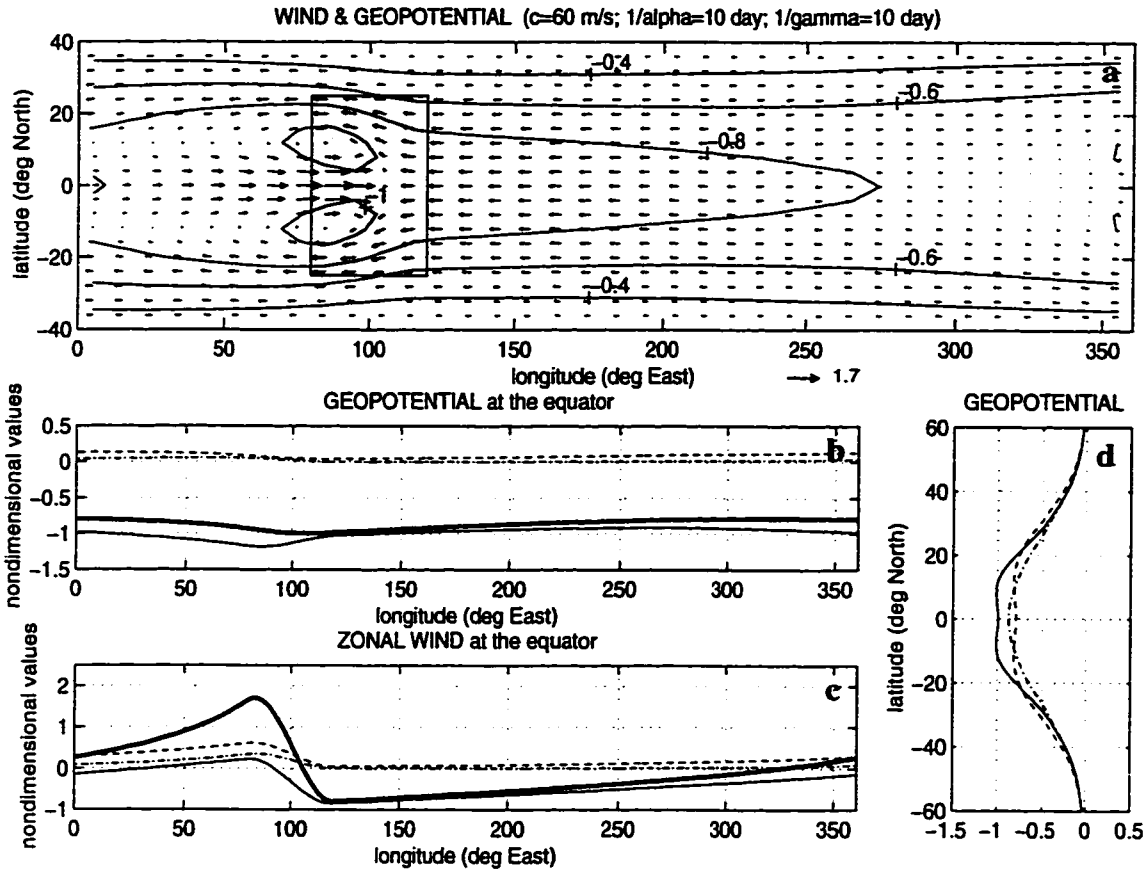

Figure 5.8: The solutions for CASE V. In panel a, the vector field (with its scale shown under the panel) of horizontal velocities are superposed on the contoured geopotential. The shaded area is where the heating happens. Panel b plots the total geopotential at the equator (the bold solid line), and the decomposed form of the geopotential at the equator (the contributions from meridional modes $\psi_0(y)$, $\psi_2(y)$,and $\psi_4(y)$ at the equator are represented by the thin solid line, the thin dashed line, and the thin dash-dotted line, respectively). Panel c plots the total zonal velocity at the equator (the bold solid line), and the decomposed form of the zonal velocity at the equator (The contributions from meridional modes $\psi_0(y)$, $\psi_2(y)$,and $\psi_4(y)$ at the equator are represented by the thin solid line, the thin dashed line, and the thin dash-dotted line, respectively). Panel d plots the meridional structures of the geopotential at different longitudes (Solid line: $100°E$ corresponding to the heating center; dashed line: $10°E$; and dash-dotted line: $190°E$).

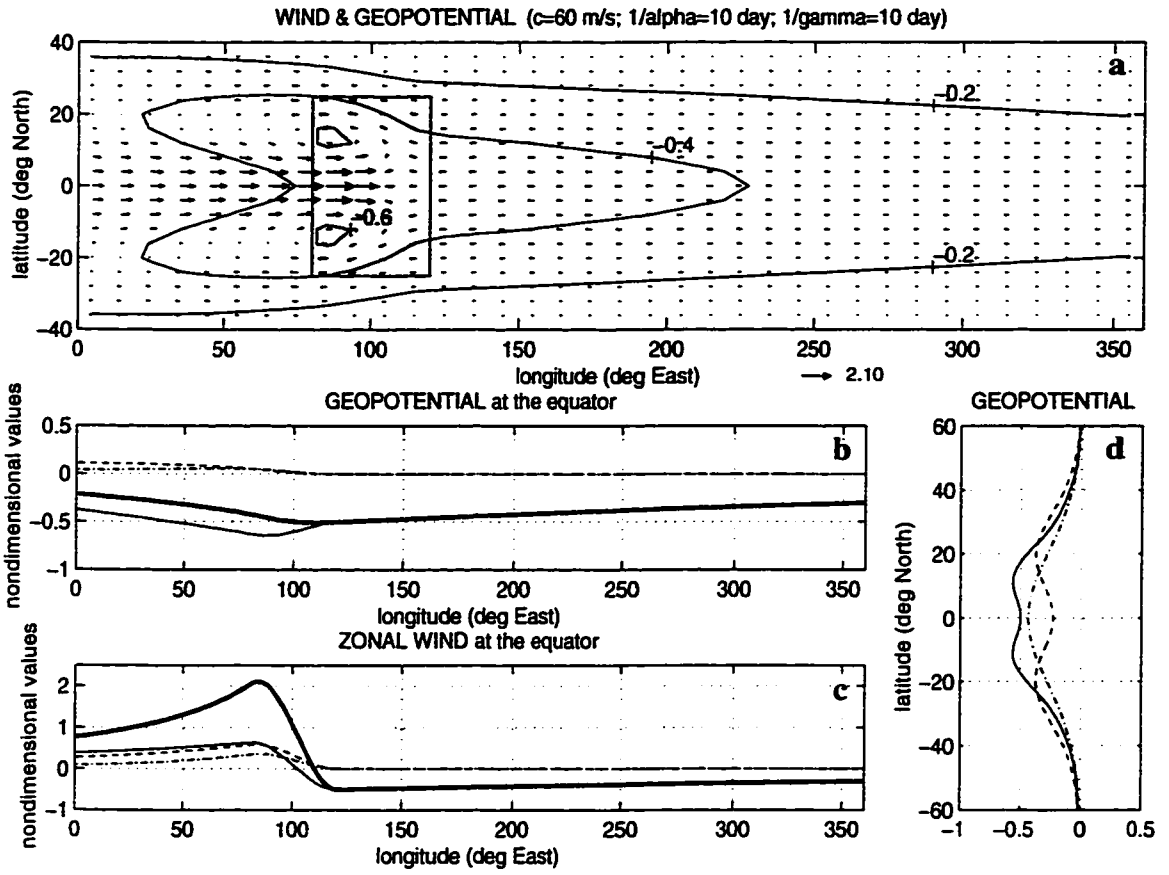

Figure 5.9: The solutions for CASE VI. In panel a, the vector field (with its scale shown under the panel) of horizontal velocities are superposed on the contoured geopotential. The shaded area is where the heating happens. Panel b plots the total geopotential at the equator (the bold solid line), and the decomposed form of the geopotential at the equator (the contributions from meridional modes $\psi_0(y)$, $\psi_2(y)$,and $\psi_4(y)$ at the equator are represented by the thin solid line, the thin dashed line, and the thin dash-dotted line, respectively). Panel c plots the total zonal velocity at the equator (the bold solid line), and the decomposed form of the zonal velocity at the equator (The contributions from meridional modes $\psi_0(y)$, $\psi_2(y)$,and $\psi_4(y)$ at the equator are represented by the thin solid line, the thin dashed line, and the thin dash-dotted line, respectively). Panel d plots the meridional structures of the geopotential at different longitudes (Solid line: $100°E$ corresponding to the heating center; dashed line: $10°E$; and dash-dotted line: $190°E$).

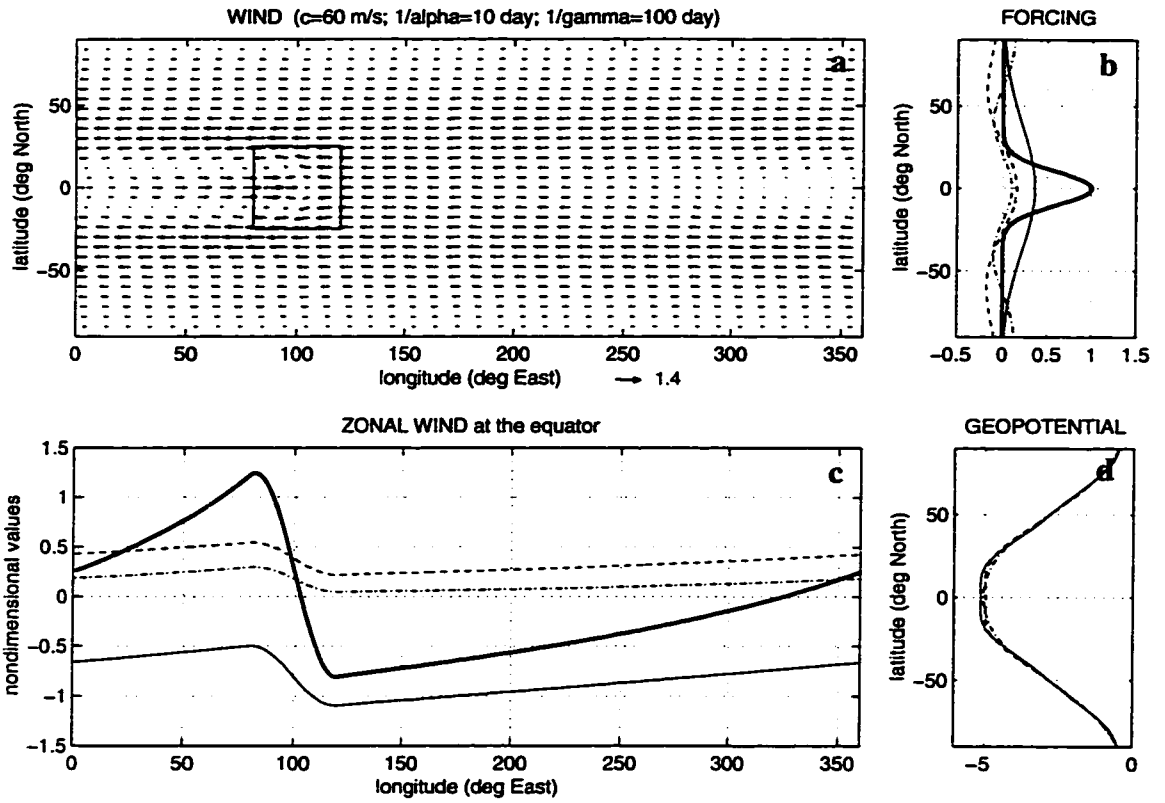

Figure 5.10: The solutions for CASE VII. Panel *a* plots the vector field (with its scale shown under the panel) of horizontal velocities. The shaded area is where the heating happens. Panel *b* plots the meridional profile of the heating (the bold solid line) and its decomposed form in terms of the parabolic cylinder functions with characteristic meridional scale of the shallow water system. The parts associated with $\psi_0(y)$, $\psi_2(y)$, and $\psi_4(y)$ are shown by the thin solid line, the thin dashed line, and the thin dash-dotted line, respectively. Panel *c* plots the total zonal velocity at the equator (the bold solid line), and the decomposed form of the zonal velocity at the equator (The contributions from meridional modes $\psi_0(y)$, $\psi_2(y)$,and $\psi_4(y)$ at the equator are represented by the thin solid line, the thin dashed line, and the thin dash-dotted line, respectively). Panel *d* plots the meridional structures of the geopotential at different longitudes (Solid line: $100°E$ corresponding to the heating center; dashed line: $10°E$; and dash-dotted line: $190°E$).

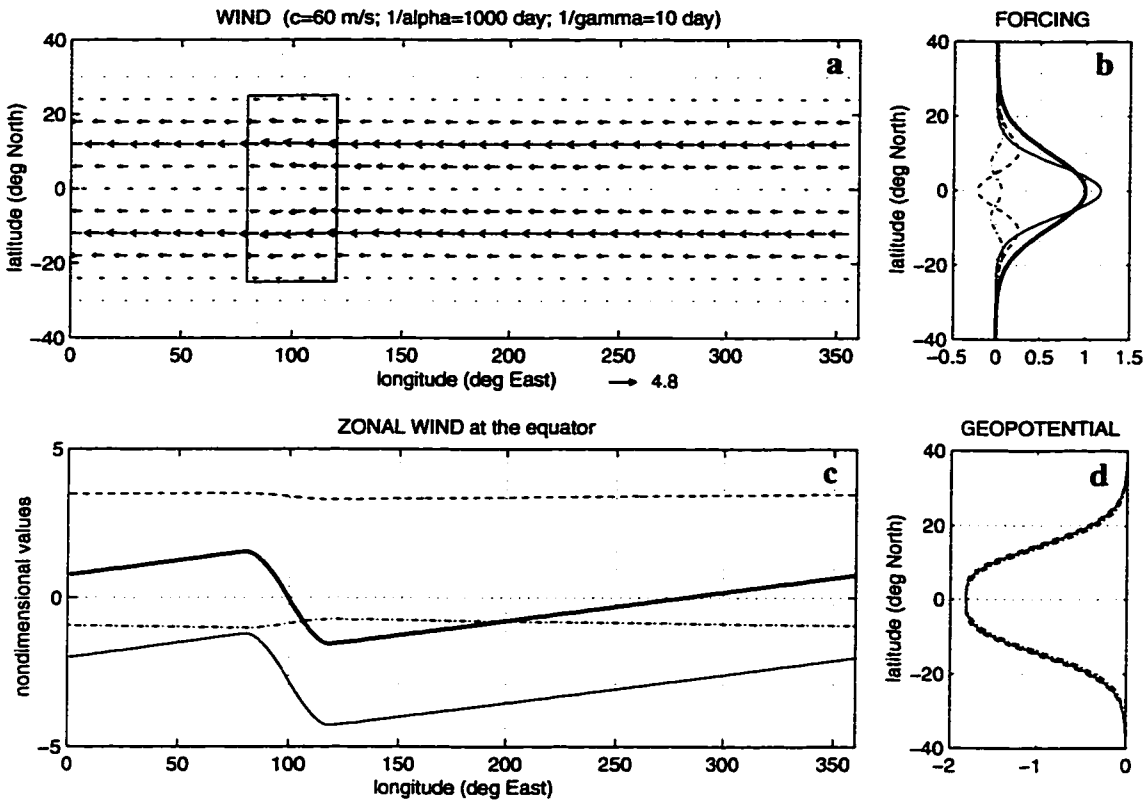

Figure 5.11: The solutions for CASE VIII. Panel *a* plots the vector field (with its scale shown under the panel) of horizontal velocities. The shaded area is where the heating happens. Panel *b* plots the meridional profile of the heating (the bold solid line) and its decomposed form in terms of the parabolic cylinder functions with characteristic meridional scale of the shallow water system. The parts associated with $\psi_0(y)$, $\psi_2(y)$, and $\psi_4(y)$ are shown by the thin solid line, the thin dashed line, and the thin dash-dotted line, respectively. Panel *c* plots the total zonal velocity at the equator (the bold solid line), and the decomposed form of the zonal velocity at the equator (The contributions from meridional modes $\psi_0(y)$, $\psi_2(y)$,and $\psi_4(y)$ at the equator are represented by the thin solid line, the thin dashed line, and the thin dash-dotted line, respectively). Panel *d* plots the meridional structures of the geopotential at different longitudes (Solid line: $100°E$ corresponding to the heating center; dashed line: $10°E$; and dash-dotted line: $190°E$).

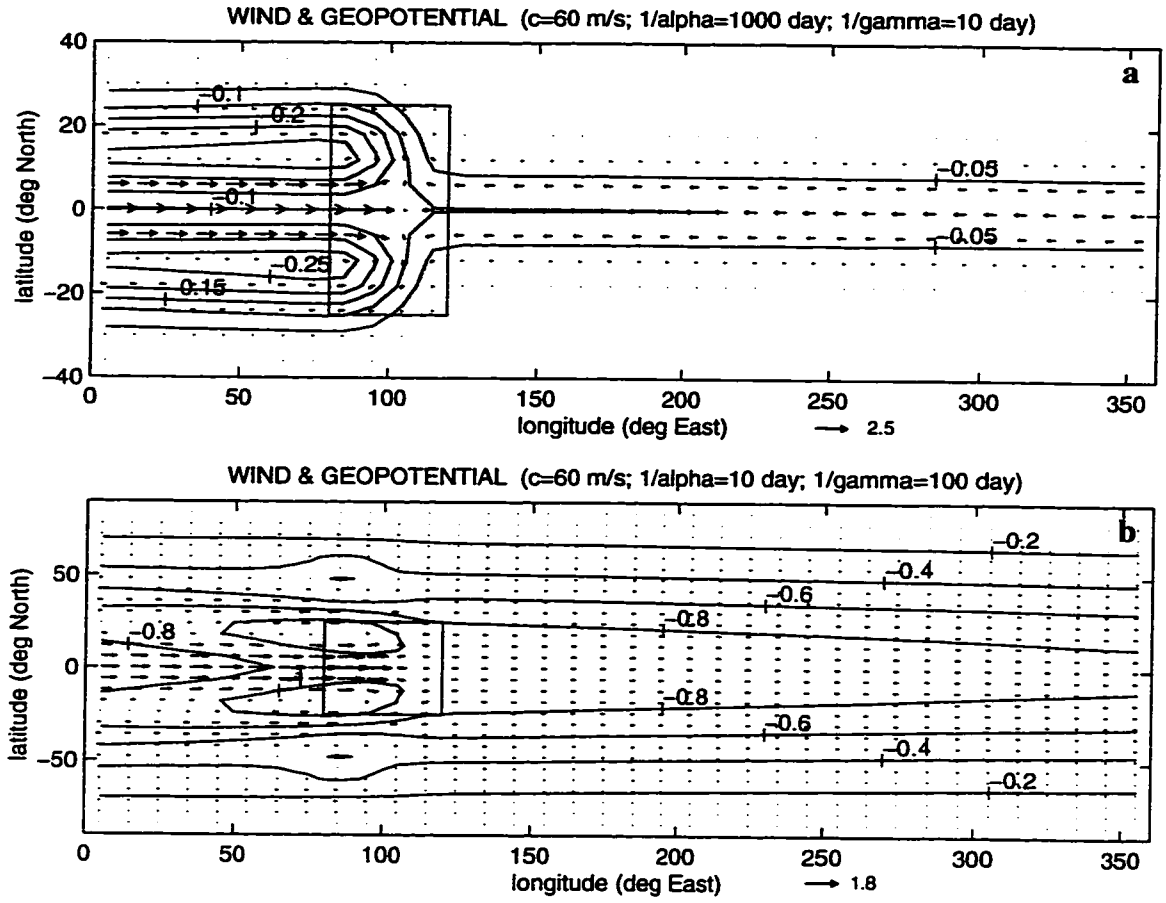

Figure 5.12: The solutions for CASE IX (panel *a*) and CASE X (panel *b*). In both panels, the vector field (with its scale shown under the panel) of horizontal velocities are superposed on the contoured geopotential. The nondimensional contour interval is 0.05 for CASE IX and 0.2 for CASE X.

Chapter 6
THERMALLY DRIVEN CIRCULATIONS IN THE TROPICS: A MODELING STUDY

6.1. Introduction

We showed in chapter 3 that Newtonian cooling changes the vertical structure of low-frequency forced waves dramatically and the vertically uniform response is seen below the bottom of the heating. To what extent this conclusion can be extended to an atmosphere with both thermal and momentum damping is not clear. In chapter 4, we demonstrated that the vertical modes that are significant for explaining the response to prescribed heating in the tropics have vertical wavelengths greater than 5 km. In chapter 5, the different impacts of Rayleigh friction and Newtonian cooling on the horizontal structure of thermally driven circulations in a single vertical mode (shallow water model) was investigated. With the solutions presented in chapters 4 and 5, we now have the tool to examine the three-dimensional structure of thermally driven circulations in the presence of both Rayleigh friction and Newtonian cooling.

In this chapter, we will mainly explore the thermally driven circulations, especially the surface winds, of the tropical atmosphere in response to a steady, large-scale, elevated heat source in a dry primitive-equation GCM. In section 6.2, we will qualitatively discuss the roles of Newtonian cooling and Rayleigh friction, the two simplest damping mechanisms often used in the theoretical studies. In section 6.3, experiments are run to simulate both the Rayleigh-friction-alone case and the Newtonian-cooling-alone case and the results are compared to the qualitative results discussed in section 6.2. In section 6.4, the model response in the presence of a simple frictional boundary layer is investigated. The discussion and summary are presented in section 6.5.

6.2. Thermally Driven Circulation in a Dissipative Atmosphere: A Qualitative Discussion

The single equation (2.11) for mass-weighted meridional velocity v is rewritten here:

$$\frac{\gamma}{N^2\alpha}\left(\frac{\partial^2}{\partial z^2}-\frac{1}{4H^2}\right)(\beta^2y^2+\alpha^2)v+\left[\left(\frac{\partial^2}{\partial x^2}+\frac{\partial^2}{\partial y^2}\right)+\frac{\beta}{\alpha}\frac{\partial}{\partial x}\right]v=$$

$$\left(\beta y\frac{\partial}{\partial x}-\alpha\frac{\partial}{\partial y}\right)\frac{1}{N^2\alpha}\left(\frac{\partial}{\partial z}-\frac{1}{2H}\right)Q\,. \tag{6.1}$$

When $\alpha\gamma$ is very small, based on the results in chapter 5, one anticipates that the terms with $\partial v/\partial x$ and $\partial^2 v/\partial x^2$ are much smaller compared to the other terms in equation (6.1). In such cases, equation (6.1) can be approximated by:

$$\frac{\gamma}{N^2\alpha}\left(\frac{\partial^2}{\partial z^2}-\frac{1}{4H^2}\right)(\beta^2y^2+\alpha^2)v+\frac{\partial^2 v}{\partial y^2}=\left(\beta y\frac{\partial}{\partial x}-\alpha\frac{\partial}{\partial y}\right)\frac{1}{N^2\alpha}\left(\frac{\partial}{\partial z}-\frac{1}{2H}\right)Q\,. \tag{6.2}$$

Equation (6.2) is elliptic. In chapter 5, it was shown that the effective equatorial radius of deformation is proportional to $(\alpha/\gamma)^{1/4}$, therefore, $\partial^2 v/\partial y^2$ is approximately proportional to $v\sqrt{\gamma/\alpha}$. Hence, at any location (x_0, y_0, z_0) outside the heating region, one has an approximate relationship:

$$\left(\frac{\partial^2}{\partial z^2}-\frac{1}{4H^2}\right)v\propto W(x_0,y_0,z_0)\sqrt{\frac{\alpha}{\gamma}}v\,, \tag{6.3}$$

where $W(x_0, y_0, z_0)$ is an unknown function whose value is usually not zero. Hence, the

structure of the forced response is greatly effected by the ratio α/γ.

Equation (6.3) gives a gross view of the vertical structure of thermally forced motion in the presence of both Rayleigh friction and Newtonian cooling. However, the presence of Rayleigh friction in equation (6.1) makes it impossible to find a complete set of meridional eigenfunctions that satisfy the boundary conditions at infinity, assuming also a Fourier representation in the zonal direction. Therefore, it is difficult to use a tidal approach to derive a non-homogeneous vertical structure equation and then to obtain the Green's functions response in the vertical. Hence, alternative approaches must be used to reveal the properties of the solutions to equations (6.1). One approach is to find the solutions in different parameter regimes. To do that, we consider two sub-systems of equations (2.3a-d). In one sub-system, we assume that the thermal damping is not effective so that the Rayleigh friction is the only mechanism to dissipate energy (the Rayleigh-friction-alone case). In the second sub-system, only Newtonian cooling is assumed to dissipate energy (the Newtonian-cooling-alone case).

6.2.1. The Newtonian-Cooling-Alone Case

In this case, γ is a limited value and $\alpha \to 0$. Hence, equations (2.3a-d) for the steady case become

$$-\beta y v = -\frac{\partial \Phi}{\partial x}, \tag{6.4a}$$

$$\beta y u = -\frac{\partial \Phi}{\partial y}, \tag{6.4b}$$

$$\frac{\partial u}{\partial x} + \frac{\partial v}{\partial y} + \left(\frac{\partial}{\partial z} - \frac{1}{2H}\right) w = 0, \tag{6.4c}$$

$$\gamma\left(\frac{\partial}{\partial z}+\frac{1}{2H}\right)\Phi + wN^2 = Q. \tag{6.4d}$$

Combining of equations (6.4a-d) leads to

$$\frac{\gamma}{N^2}\beta y^2\left(\frac{\partial^2}{\partial z^2}-\frac{1}{4H^2}\right)\Phi+\frac{\partial\Phi}{\partial x} = \frac{\beta y^2}{N^2}\left(\frac{\partial}{\partial z}-\frac{1}{2H}\right)Q. \tag{6.5}$$

Terms with scale height H in equation (6.5) are very small for the response of the system under the forcing considered in this paper, and these terms can be omitted (these terms come from basic density variation in the vertical direction).

In the previous chapter, we have already shown that outside of the heating longitudes $\partial/\partial x \propto \sqrt{\alpha\gamma}$. When $\alpha \to 0$, $\partial/\partial x \to 0$. Therefore, outside of the heating longitudes equation (6.5) becomes

$$\frac{\gamma}{N^2}\beta y^2\left(\frac{\partial^2}{\partial z^2}-\frac{1}{4H^2}\right)\Phi \approx 0 . \tag{6.6}$$

Away from the immediate vicinity of the equator, equation (6.6) results in

$$\left(\frac{\partial^2}{\partial z^2}-\frac{1}{4H^2}\right)\Phi \approx 0 \tag{6.7}$$

outside of the heating layers. The upper boundary condition requires that the total perturbed kinetic energy is limited at the top of the atmosphere. If the heating term Q represents the large-scale cumulus heating of the tropical atmosphere, Q is zero below the lifting condensation level Z_l and above the cloud top Z_t (somewhere close to the

tropopause). Thus we find

$$\left(\frac{\partial}{\partial z}+\frac{1}{2H}\right)\Phi \approx 0 \tag{6.8}$$

both below the lifting condensation level Z_l and above the cloud top Z_t. The solutions to equation (6.8) automatically satisfy the lower boundary condition. Combining equations (6.4b), and (6.8) leads to

$$\left(\frac{\partial}{\partial z}+\frac{1}{2H}\right)u \approx 0 \text{ , for } z<Z_l \text{ or } z>Z_t. \tag{6.9a}$$

Note that u is the mass-weighted eastward (zonal) velocity. For eastward (zonal) velocity u^* itself, equation (6.9a) simplifies to

$$\frac{\partial u^*}{\partial z} \approx 0 \text{ , for } z<Z_l \text{ or } z>Z_t. \tag{6.9b}$$

Equation (6.9b) indicates that from the cloud base to the surface where the external forcing is zero, the zonal velocity is vertically uniform. Since the zonal velocity is generally *not* zero at the cloud base, this result implies that surface wind can be driven by upper level forcing when thermal damping dominates.

Physically, Newtonian cooling parameterizes the processes that drive the perturbed atmosphere to its thermal equilibrium state. Since temperature is proportional to $\partial\Phi/\partial z$ in an isothermal atmosphere (this relation is also a very accurate approximation in the case of a non-isothermal atmosphere), Newtonian cooling relaxes $\partial\Phi/\partial z$ to zero in the layers where the external heating rate is zero. Hence, we can expect that the vertical derivative

of horizontal velocity to be zero in non-heated layers where the Newtonian cooling dominates. This also indicates that Newtonian cooling in a three-dimensional atmosphere acts differently from in a two-dimensional shallow water system where Newtonian cooling mainly relaxes the amplitude of the perturbation of geopotential forced by external heating.

6.2.2. The Rayleigh-Friction-Alone Case

In this case, α is a limited value and $\gamma \to 0$. Hence, equations (2.3a-d) for the steady case become

$$\alpha u - \beta y v = -\frac{\partial \Phi}{\partial x}, \tag{6.10a}$$

$$\alpha v + \beta y u = -\frac{\partial \Phi}{\partial y}, \tag{6.10b}$$

$$\frac{\partial u}{\partial x} + \frac{\partial v}{\partial y} + \left(\frac{\partial}{\partial z} - \frac{1}{2H}\right) w = 0, \tag{6.10c}$$

$$wN^2 = Q. \tag{6.10d}$$

If the heating $Q(x, y, z)$ can be expressed as the product of horizontal $\underset{\sim}{Q}(x, y)$ and vertical $S(z)$ structures for which the first-order vertical derivatives at Z_l and Z_t exist (so that the vertical boundary conditions can be satisfied), we can write all the variables as $u = \underset{\sim}{u}(x, y)(\partial/\partial z - 1/2H)S$, $v = \underset{\sim}{v}(x, y)(\partial/\partial z - 1/2H)S$, $w = \underset{\sim}{w}S$, and $\Phi = \underset{\sim}{\Phi}(x, y)(\partial/\partial z - 1/2H)S$. Then, equations (6.10a-d) become:

$$\alpha \underset{\sim}{u} - \beta y \underset{\sim}{v} = -\frac{\partial \underset{\sim}{\Phi}}{\partial x}, \tag{6.11a}$$

$$\alpha \underset{\sim}{v} + \beta y \underset{\sim}{u} = -\frac{\partial \underset{\sim}{\Phi}}{\partial y}, \tag{6.11b}$$

$$\frac{\partial \underset{\sim}{u}}{\partial x} + \frac{\partial \underset{\sim}{v}}{\partial y} = -\frac{\underset{\sim}{Q}}{N^2}, \tag{6.11c}$$

$$\underset{\sim}{w} N^2 = \underset{\sim}{Q}. \tag{6.11d}$$

Equations (6.11a-c) are a two-dimensional system that has already been analytically solved in last chapter. Since the response is proportional to $S(z)$, it is limited to the layers where the heating is not zero. Hence, in this model an elevated large-scale heat source can not affect the surface circulation in the tropics when Rayleigh friction dominates. Combining equations (6.11a-c), we obtain equations of $\underset{\sim}{u}$ and $\underset{\sim}{v}$ in terms of $\underset{\sim}{Q}$:

$$\left[\left(\frac{\partial^2}{\partial x^2} + \frac{2\beta}{\alpha}\frac{\partial}{\partial x}\right) + \frac{\partial^2}{\partial y^2}\right]\underset{\sim}{u} = \frac{1}{N^2}\left(\frac{\partial}{\partial x} + \frac{\beta y}{\alpha}\frac{\partial}{\partial y} + \frac{2\beta}{\alpha}\right)\underset{\sim}{Q}. \tag{6.12}$$

In the previous chapter, we showed that outside the heating longitudes $\partial/\partial x \propto \sqrt{\alpha\gamma}$. When $\gamma \to 0$, $\partial/\partial x \to 0$. Therefore, outside of the heating longitudes equation (6.12) becomes

$$\frac{\partial^2 \underset{\sim}{u}}{\partial y^2} \approx \frac{1}{N^2}\left(\frac{\beta y}{\alpha}\frac{\partial}{\partial y} + \frac{2\beta}{\alpha}\right)\underset{\sim}{Q}. \tag{6.13}$$

Outside of the heating latitudes, equation (6.13) can be further simplified to

$$\frac{\partial \underline{u}}{\partial y} \approx 0. \tag{6.14}$$

Equation (6.14) states that outside of the heating latitudes, the zonal wind driven by the thermal source bears little variation in the Rayleigh-friction-alone case. In a meridional infinite domain, this also means that the amplitude of the zonal velocity approaches to zero so as to satisfy the meridional boundary condition.

6.2.3. Discussion

The overall response to an elevated heat source in the presence of both Rayleigh friction and Newtonian cooling is expected to be an amalgamation of these two extreme cases and will depend on the relative rates of both Rayleigh friction and Newtonian cooling (see also section 6.3). The observational studies by Reed and Recker (1971) and Wallace (1971) suggests that the thermal damping term is at least an order of magnitude smaller than the large-scale cumulus heating term in the heating region. Outside the heating region, the radiative cooling is often balanced by the adiabatic heating due to the downward motion; in general, the time scale of Newtonian cooling is of the order of two weeks and that of Rayleigh friction is about 5 to 10 days. When the damping terms are assumed to represent cumulus friction and vertical transport of heat by cumulus convection, however, both the effective Rayleigh friction and Newtonian cooling can be of the order of a day or less in the tropics. Holton and Cotton (1972) pointed out that the damping used in a linear model need to be much stronger (less than a day) than people generally would believe to mimic for some of the nonlinearity existed in the tropical atmosphere. In short, it is difficult to say a priori if the true atmosphere has a response to heating that is similar to the either limiting dissipation case (thermal or momentum), or if it has a response that is altogether different due to nonlinearity.

6.3. Numerical experiments

The analytical arguments in section 6.2 suggest the different roles of Rayleigh friction and Newtonian cooling in defining the gross response to steady tropical heating. In this section, we analyze model output from two idealized numerical experiments, in which the prescribed heating is identical. The first experiment is "*the Newtonian-cooling-alone case*" in which the model only has Newtonian cooling as the only dissipation mechanism. In the second experiment, Rayleigh friction replaces Newtonian cooling (*the Rayleigh-friction-alone case*). We will examine the circulation patterns associated with both cases, and determine to what extent the model results are consistent with the qualitative analysis in section 6.2.

6.3.1. The Model Experiments

The numerical model used in this chapter was introduced in Chapter 2. The prescribed heating in this chapter is the same as in equations (5.1) and (5.2). The shape of Q is displayed in Fig. 6.1, along with the locations of the cross-sections (labeled W, C, E, P_i, and H_i) that we will use to examine the results. Panel a is the horizontal structure (in which only part of the horizontal domain is shown) and panel b is the vertical distribution of the heating. The cloud base taken in this chapter is somewhat higher than observed in the tropical western Pacific (840 hPa vs. the observed 940 hPa; see Mapes and Houze (1995)) so as to clearly illuminate the vertical structure of the flow in the region extending below the heating to the surface.

Two model runs are performed. The first run has Rayleigh friction only: no other dissipation is applied to the model. The Rayleigh friction rate is taken to be $\alpha^{-1} = 10$ days. The second run examines the opposite end of the parameter regime, where the

momentum damping is set to zero and Newtonian cooling is the only damping in the model. The lower boundary condition is the inviscid condition, $\partial u^*/\partial z = 0$ (i.e., there is no boundary layer.)

There are two ways to determine the value of Newtonian cooling rate. The first approach is from a linearization of the basic physical processes, such as radiative cooling. In this approach, the inverse of the Newtonian cooling rate is estimated to be about two weeks or longer. Because the Newtonian cooling must also account for additional thermal dissipative processes (e.g., turbulence, convection), an appropriate (effective) Newtonian cooling rate in a primitive equation model may be much greater than the inverse of the radiative time scale. Hence, we determine the Newtonian cooling rate as follows. In the tropics, the maximum temperature perturbation observed on seasonal time scale is less than $2°C$ (Bantzer and Wallace 1996). To keep the model temperature perturbation comparable to the observations when the model is driven by a heat source that is similar to the observed heat source in western tropical Pacific in spacial scale (a few thousand kilometers) and amplitude (maximum heating rate corresponding to 10 mm of precipitation per day), we found that $\gamma^{-1} \approx 2.5$ days, a value comparable to that used in other models (e.g., Gill 1980, Geisler 1981). The model results discussed later are not qualitatively dependent on the value of Newtonian cooling rate in the Newtonian-cooling-alone case as long as the prescribed maximum heating rate in the model is less than 50 mm of precipitation per day, i.e., the model response is essentially linear.

We run both model experiments for 400 model days. Fig. 6.2 plots the global kinetic energy and the global perturbed potential energy for both cases. Since there is no thermal damping in the Rayleigh-friction-alone case, the global potential energy grows linearly while the global kinetic energy approaches a steady state. A physical scenario corresponding to this case is that the thickness between two isobaric planes increases as it is

heated while the slope of the two planes remains unchanged. For the Newtonian-cooling-alone case, the global potential energy goes to steady state very fast, while the global kinetic energy equilibrates at a much slower rate. After about 100 model days, the magnitude of the horizontal velocity is increasing in the Newtonian-cooling-alone case but the three dimensional structure of horizontal velocity is robust for integrations larger than 100 model days.

6.3.2. Model Results I: the Newtonian-Cooling-Alone Case

Fig. 6.3 shows the zonal velocity at different longitudes. Although the zonal winds in the upper troposphere are crudely opposite to that in the lower troposphere at almost every latitude, there are some differences between the vertical structure of the response to the east and the west of the heat source (see also Fig. 6.4). To the west of the heat source (panel *a*), the level of zero wind is located at about 450 hPa. In the lower troposphere, a narrow but strong westerly band sits between two strong easterly bands to the north and the south, and the maximum width of this westerly band is about 10° in latitude. The upper troposphere is dominated by westerlies although there is a band of relatively weak easterly wind just above the westerly jet in the lower half of the troposphere in the equatorial zone. To the east of the heat source (panel *c*), the lower troposphere is dominated by easterlies and the upper troposphere by westerlies and the zero wind level is much lower than it is to the west of the heat source. At the center of the heating region (panel *b*), the zonal winds in the upper troposphere resembles those to the west of the heating, while the zonal winds in the lower troposphere resembles those to the east of the heating. At every longitude, the response is meridionally confined to where the heating takes place: poleward of 20° latitude, the signal is vanishingly small. This result is consistent with the analytical results obtained in chapter 5.

At the surface, easterlies are predominant. The magnitude of easterlies increases with increasing latitude from the equator to about 10° where the easterlies reach their maximum. Poleward of 10° latitude, the magnitude of easterlies decreases dramatically. To the west of the heating region, the surface winds are very weak in a very narrow band (about 2°) centered about the equator.

The winds at the top of the model atmosphere are not zero. However the response to such an isolated heat source is not sensitive to where the lid is imposed as long as it is imposed higher than 100 hPa because the density above 100 hPa is very small. Thus, there is little vertical energy propagation near the lid; hence, the total energy reflected by the artificial lid is negligible.

Fig. 6.4 and Fig. 6.5 show the forced circulations and the temperature perturbations at different latitudes. Easterlies dominate in the lower troposphere; above, westerlies dominate almost everywhere except in a narrow meridional band along the equator. Large vertical velocity is significant equatorward of 10° latitude, where heating is mainly balanced by adiabatic cooling due to upward motions. To the east of the forcing region, the meridional velocity is almost zero everywhere, while to the west the meridional velocity decreases very rapidly away from the heat source. Fig. 6.5 shows the temperature perturbations at different latitudes. The temperature perturbations reach their maximum at the level of maximum heating. The isotherms are almost flat in the zonal direction at all the latitudes, especially in the upper troposphere, despite the large Newtonian cooling rate. The zonal overturning can be identified in panels a and b of Fig. 6.4 but the two-cell structure is somewhat ill-defined along the equator.

The decoupling between the temperature and the horizontal wind (which does show decay away from the heating in the equatorial region) is quite clear in the previous

figures. In panel *b* and *d* of Fig. 6.6, the anomaly zonal winds do decay away from the heat source in the zonal direction, but the zonal decay rate to the west of the heat source is similar to that to the east of the heat source, rather than being three-fold higher as in Gill's solution. Finally, by removing the zonal mean from the zonal velocities then averaging over two 10° latitude bands, one finds that the zonally overturning cells are confined to a narrow band along the equator (Fig. 6.7).

Vertical profiles of zonal velocity at different locations are shown in Fig. 6.8. It is clear that the vertical structure of zonal velocity varies dramatically at different locations. At about 10°N, the low level zonal velocity is almost as large as the zonal velocity at 750 hPa. The zonal velocity at that latitude is also fairly uniform zonally. Another interesting feature is that zonal velocity is quasi-uniform with height below the bottom of the heat source, also evident in Fig. 6.9: below 900 hPa, the zonal velocity is everywhere nearly uniform vertically. This agrees well with the analytical results in section 6.2 and chapter 3.

6.3.3. Model Results II: the Rayleigh-Friction-Alone Case

As we anticipated from the analysis in section 6.2, for the Rayleigh-friction-alone case the atmospheric motion is confined in the vertical to where the heating takes place: below and above the heat source, the atmosphere is not effected by the heating. Fig. 6.10 is the counterpart of Fig. 6.3 for the Rayleigh-friction-alone case. Compared to the narrow meridional response in the Newtonian-cooling-alone case (Fig. 6.3), we see that the response to the heating is global. Westerly jets are found in the subtropical upper troposphere to the west of the heat source. To the east of the heating, these two westerly jets merge to form a broad westerly flow extending from pole to pole in the upper troposphere. The flow in the lower troposphere is similar in pattern to that in the upper

atmosphere, albeit weaker and with opposite sign. The zonal flow below and above the heat source in the tropical region is vanishingly small, consistent with the analysis applied on the tropical beta-plane in section 6.2.

The circulations at different latitudes are displayed in Fig. 6.11. A zonal overturning circulation is evident along the equator, especially to the east of the heating region. At higher latitudes, easterlies are found in the lower troposphere and westerlies dominate in the upper troposphere. The zonal decay away from the heating region is much clearer than in the Newtonian-cooling-alone case. The *pattern* of meridional velocity in the Rayleigh-friction-alone case is quite different from that in the Newtonian-cooling-alone case (cf. Fig. 6.4). Off the equator, the westward decay of the meridional velocity is more gradual than in the Newtonian-cooling-alone case: for example, at about 15 degree latitude (Fig. 6.11*d*), we see poleward motion in the upper troposphere and an equatorward motion in the lower troposphere at almost every longitude except where the heat source is located.

As expected, the upward motion takes the shape of the heating in the equatorial region while the downward motion is broad but very weak (Fig. 6.11*a*). Although the forcing is localized, isotherms are again flat in the zonal direction throughout the tropics (not shown). Because there is no thermal damping, the amplitude of temperature perturbation is very large.

Fig. 6.12 shows the zonal velocity at different heights. After its zonal mean is removed, we see that zonal wind is qualitatively similar to that described by Gill (1980). The zonally averaged quantities are shown in Fig. 6.13, which clearly illustrates a global Hadley circulation (cf., Fig 6.13 *a* for the Newtonian-cooling-alone case). The flow below the heating is weak everywhere, evident from Fig. 6.11 and Fig. 6.13.

The zonal overturning in the Rayleigh-friction-alone case is quite different from that in the Newtonian-cooling-alone case (comparing Fig. 6.14 to Fig. 6.7). In the Rayleigh-friction-alone case, the zonal overturning is zonally asymmetric about the heat source and the zonal wind anomaly in the upper troposphere is much thinner vertically but larger in strength than that in the lower troposphere in the Rayleigh-friction-alone case.

In Fig. 6.15, we plot vertical profiles of zonal velocity, vertical velocity, and temperature perturbation at different locations. Although a non-zero surface wind is seen at high latitudes, there is vanishingly small flow in the tropical region above and below the heating layers.

6.3.4. Model Results III: Convergence of Low Level Mass and Moisture

The divergence at different altitudes and the vertically integrated mass convergence from surface to all levels below 400 hPa for the two experiments are shown in Fig. 6.16. The convergence below the heat source in both cases is negligible. The transition altitude from convergence to divergence in the Rayleigh-friction-alone case is at about 400 hPa, which is much higher than that in the Newtonian-cooling-alone case. The convergence between 850 hPa and 500 hPa in the Newtonian-cooling-alone case is stronger than that in the Rayleigh-friction-alone case.

Importantly, the maximum vertically integrated mass convergence in both cases is smaller than 300 $kg \cdot day^{-1} m^{-2}$. Even if we assume that the mixing ratio of water vapor below 400 hPa is everywhere 25 g/kg (which is about the saturation value of moisture at $30°C$), the total convergence of moisture from the surface to the top of atmosphere is still less than 7.5 $kg \cdot day^{-1} m^{-2}$ which corresponds to 7.5 mm/day of precipitation. If the moisture convergence is regarded as mainly a boundary layer process, then it is clear that

the flows generated by a large-scale heat source with a base at 840 hPa (or above) could not provide enough moisture convergence to maintain that heat source.

6.4. Role of a simple frictional boundary layer

In the previous sections we found that when the damping is exclusively momentum damping (Rayleigh friction), the response of the atmosphere to a heat source localized in the vertical is constrained to the layers of the atmosphere that are heated; hence, there is no surface response unless the heating extends to the surface. In contrast, an elevated heat source *does* support a surface wind response in the case where the damping is exclusively thermodynamic (Newtonian cooling). Of course, this solution is unrealistic because any surface response must in nature experience momentum damping. In this section we perform one more integration in order to explore how the inclusion of a simple frictional boundary layer affects the surface response when there is also uniform thermal damping throughout the atmosphere. The heating and the Newtonian cooling rate are prescribed identically to that in section 6.3. The atmosphere above 850 hPa is inviscid, and we have included a frictional boundary layer with a Rayleigh friction time scale of 2 days between 850 hPa and 975 hPa and 1 day below 975 hPa. Selected results from this experiment are shown in Fig. 6.17.

The panels in Fig. 6.17 show that including a simple representation of a boundary layer dramatically suppresses the surface circulation that was found in the Newtonian-cooling-alone case. Taken at face value the analytical and numerical results of sections 6.2 and 6.3 along with this experiment suggest that it is very unlikely that an elevated heat source locates above 1 km could generate a significant boundary layer circulation unless the base of the heating is embedded well within the boundary layer. When the cloud base is quite low (for example, the CP heating in Chapter 4), we can not rule out the possibility of strong surface winds driven by elevated heat source (see, Fig. 4.9). It remains to be

seen to what extent this conclusion is sensitive to the formulations of friction and thermal damping and especially to the location of the base of the heating and its relationship to the top of the boundary layer.

6.5. Discussion and Summary

In this chapter, We have examined the three-dimensional steady response of the tropical atmosphere to an isolated heat source in the tropics using both analytical methods and a dry primitive equation model of the atmosphere. In the analytical part of the study, two special cases are examined: one has Newtonian cooling as the only dissipation to balance the energy input by the heating, while the other has Rayleigh friction and no thermal damping. To verify the analytical arguments, we carried out a series of numerical experiments.

The analytical results and the numerical results are consistent in showing that Rayleigh friction and Newtonian cooling play very different roles in the tropical atmosphere. Newtonian cooling homogenizes the atmospheric motion in the vertical, and a strong, vertically uniform wind is found below the bottom of the heat source. When Rayleigh friction serves as the only damping in the tropical atmosphere, there is not much interaction in the vertical between the forced and unforced atmospheric layers: all the energy put into a layer is dissipated within that layer. Hence, no surface wind is found unless the heat source reaches close to the surface. The horizontal structure of winds in this case is somewhat similar to the solution given by Gill (1980).

From the analysis in section 6.2, we know that only when momentum damping is fairly strong can the signal in the tropics propagate to the extratropics and a strong meridional overturning circulation will form. The strong momentum damping also causes the response to be vertically confined to the layer in which the heat source resides. Hence, the

low-level flow in the deep tropics (i.e., between $10°N$ and $10°S$) is not associated with a strong Hadley circulation driven by an elevated tropical heat source: it is due to the surface pressure gradients generated by the hydrostatic adjustment to SST gradients. This conclusion is confirmed by our numerical results and is also quite consistent with the modeling results of Schneider and Lindzen (1977) and Battisti and Ovens (1995), who found that the surface winds in the deep tropics are not associated with the thermally forced Hadley circulation.

The zonal overturning circulation (the Walker circulation) is identified in a narrow band centered about the equator in both the Rayleigh-friction-alone case and the Newtonian-cooling-alone case. However, the structure of the zonal overturning cell is much different in these two cases. In the Newtonian-cooling-alone case, the zonal overturning cell (after removing the zonal means) is fairly symmetric about the heat source, while in the Rayleigh-friction-alone case, the overturning to the east of the heat source is wider than that to the west.

The numerical solution is also found for the case where Newtonian cooling acts uniformly in the vertical *and* Rayleigh friction is included in the lower atmosphere to mimic crudely the dissipation of momentum in the boundary layer. The introduction of the simple boundary layer dramatically reduces the surface circulation that was supported in the Newtonian-cooling-alone case. Together these results suggest a significant surface circulation will unlikely be driven by an elevated heat source if the base of the heating lies outside the planetary boundary layer.

The vertically integrated mass convergence shows that the forced flow does not provide enough moisture convergence to maintain the heat source, suggesting that heating is fueled by the moisture convergence associated with the boundary layer flows driven by SST gradients. Since our estimation of the moisture convergence is somewhat an upper

limit and is not sensitively dependent on the base of the heating, we expect that the previous conclusion concerning the moisture convergence will hold even when a realistic boundary layer is included in the model.

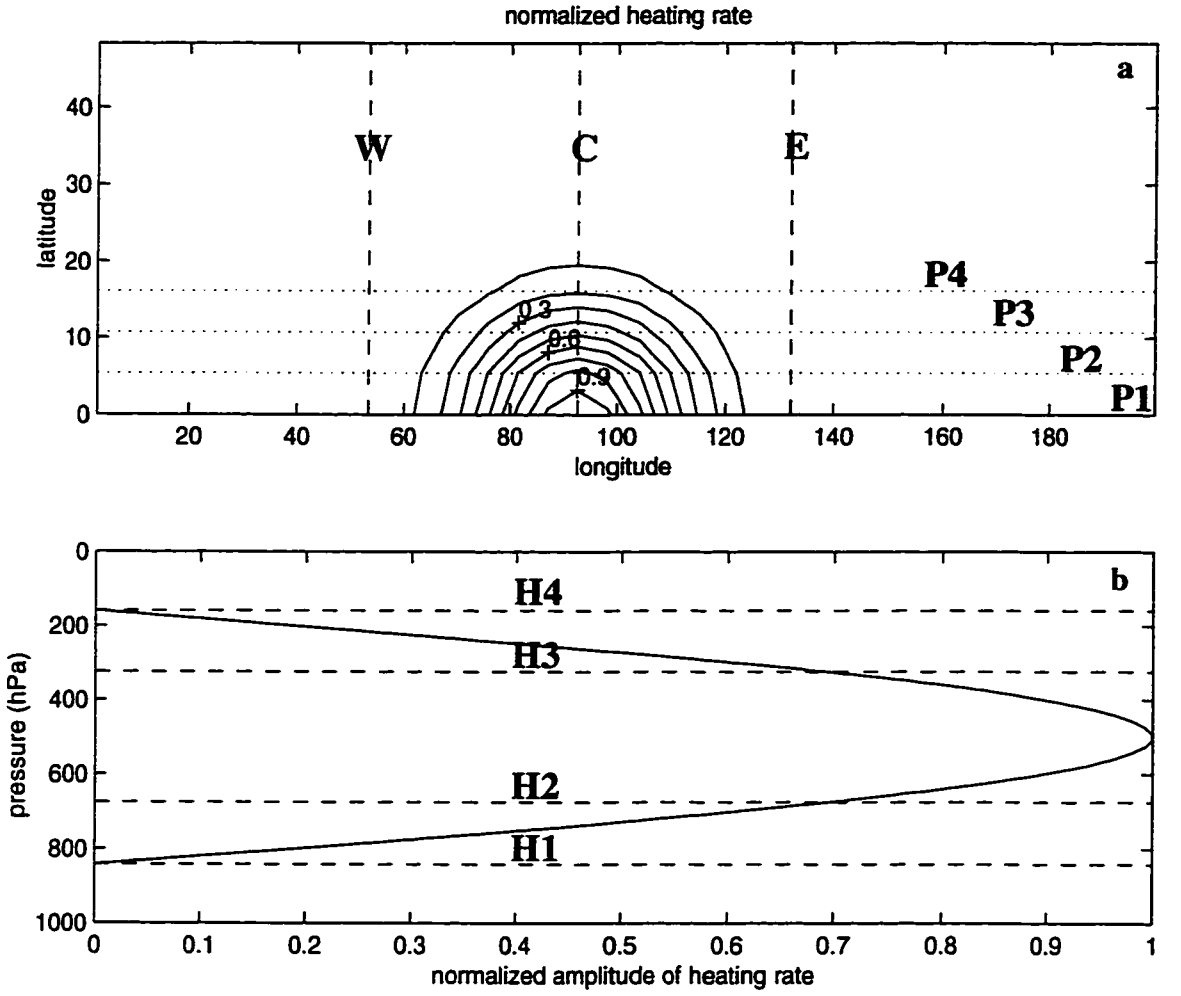

Figure 6.1: Distribution of normalized heating rate on the horizontal plane (panel *a*) and in the vertical direction (panel *b*). In panel *a*, the solid lines represent the normalized heating rate, the dashed lines and the dotted lines show the locations where the physical fields are analyzed later: W, C, and E are the longitudes $53.4°E$, $92.8°E$, and $132.2°E$, respectively; P1, P2, P3, and P4 are latitudes $0°$, $5.4°N$, $10.7°N$, and $16.1°N$, respectively. In panel *b*, the solid line represents the dependence of heating rate on height, the dashed lines show the heights where the physical fields are analyzed later: H1, H2, H3, and H4 are the altitudes 840 hPa, 675 hPa, 325 hPa, and 160 hPa, respectively.

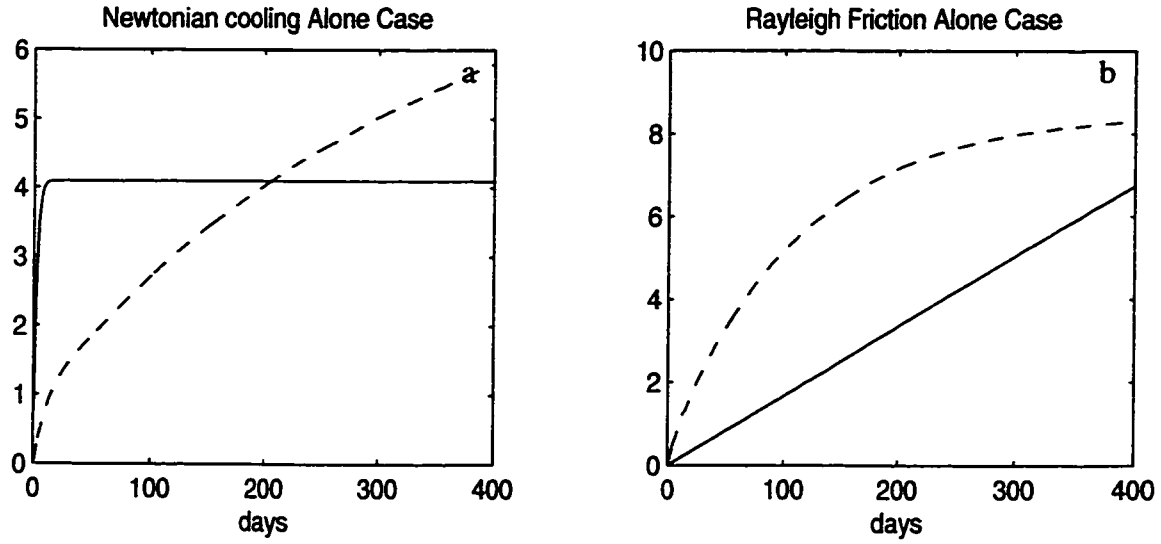

Figure 6.2: Time evolution of global potential energy (solid lines) and global kinetic energy (dashed lines) for the Newtonian-cooling-alone-case (panel a) and for the Rayleigh-friction-alone-case (panel b). The units for all plots except the potential energy in the Rayleigh-friction-alone-case are $10^{18}J$. For the potential energy in the Rayleigh-friction-alone-case, the units are $10^{20}J$.

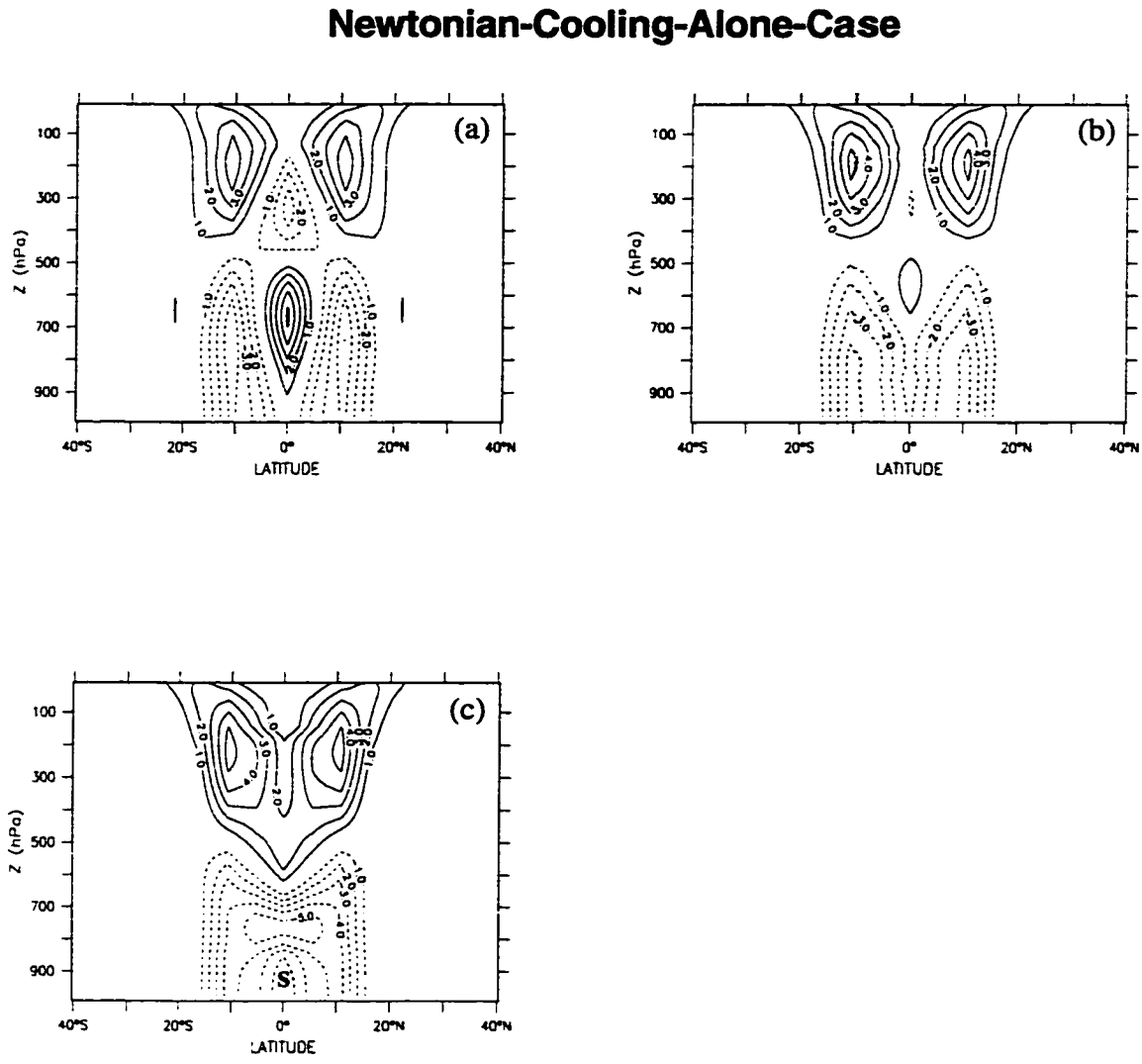

Figure 6.3: Zonal velocities at different longitudes for the Newtonian-cooling-alone-case. Panel a is at $53.4°E$; panel b is at $92.8°E$; panel c is at $132.2°E$. Westerlies are represented by solid lines, and easterlies are represented by dashed lines. Contour interval is 1.0 ms^{-1} in every panel, and the zero contour lines are not shown. The 's' in panel c represents a minimum center.

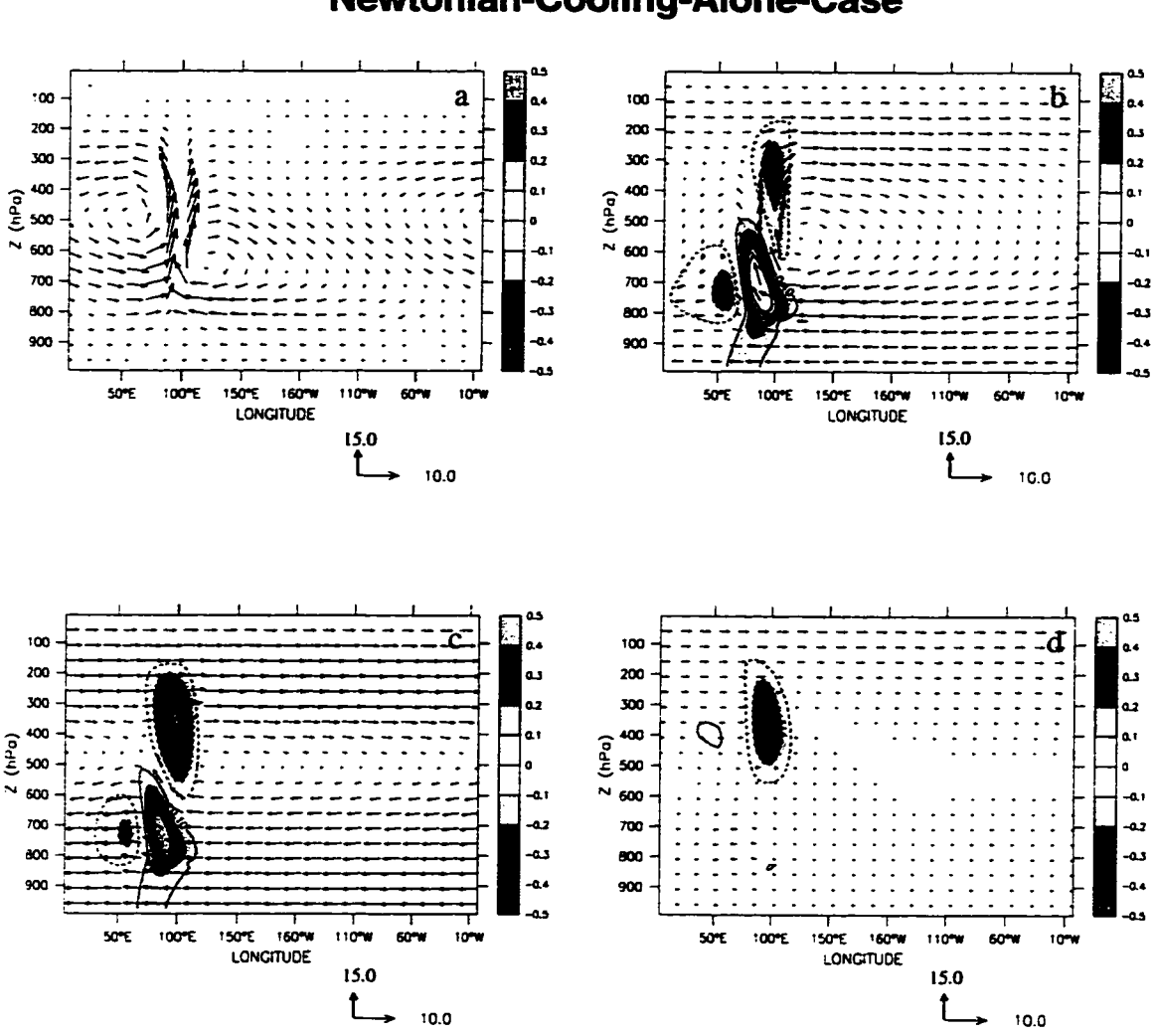

Figure 6.4: The zonal overturning circulations at different latitudes for the Newtonian-cooling-alone-case. The vector field of zonal velocity (with unit ms^{-1}) and vertical velocity ($-dp/dt$ with unit $hPa \cdot day^{-1}$) are superposed on the contoured meridional velocity (with contour interval 0.1 ms^{-1}). The zonal velocity and the vertical velocity are scaled separately, and are shown under each panel, respectively. Panel a is at the Equator; panel b is at $5.4°N$; panel c is at $11.7°N$; panel d is at $16.1°N$.

Newtonian-Cooling-Alone-Case

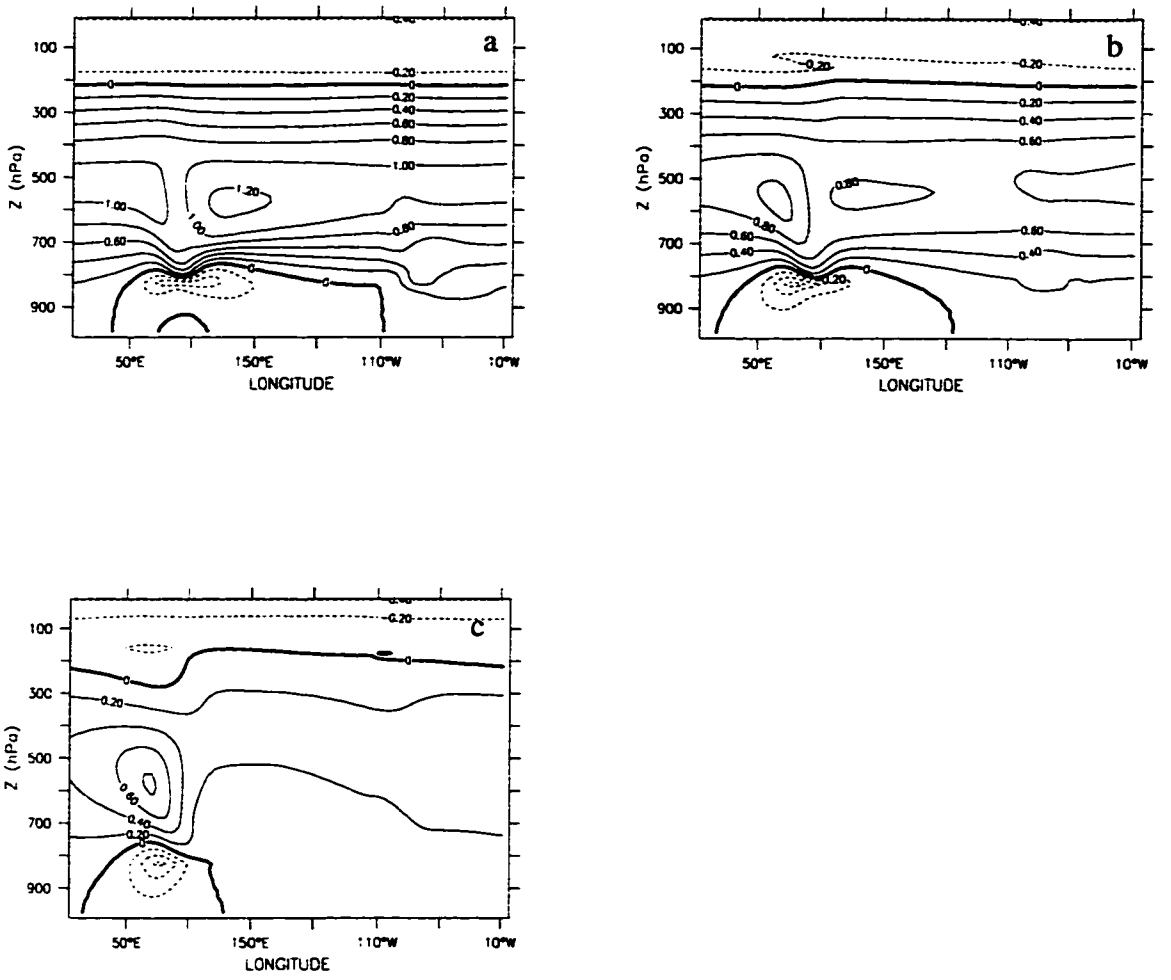

Figure 6.5: Temperature perturbations at different latitudes for the Newtonian-cooling-alone-case. Panel a is at the Equator; panel b is at $5.4°N$; panel c is at $11.7°N$. Contour interval is $0.2°C$ in each panel.

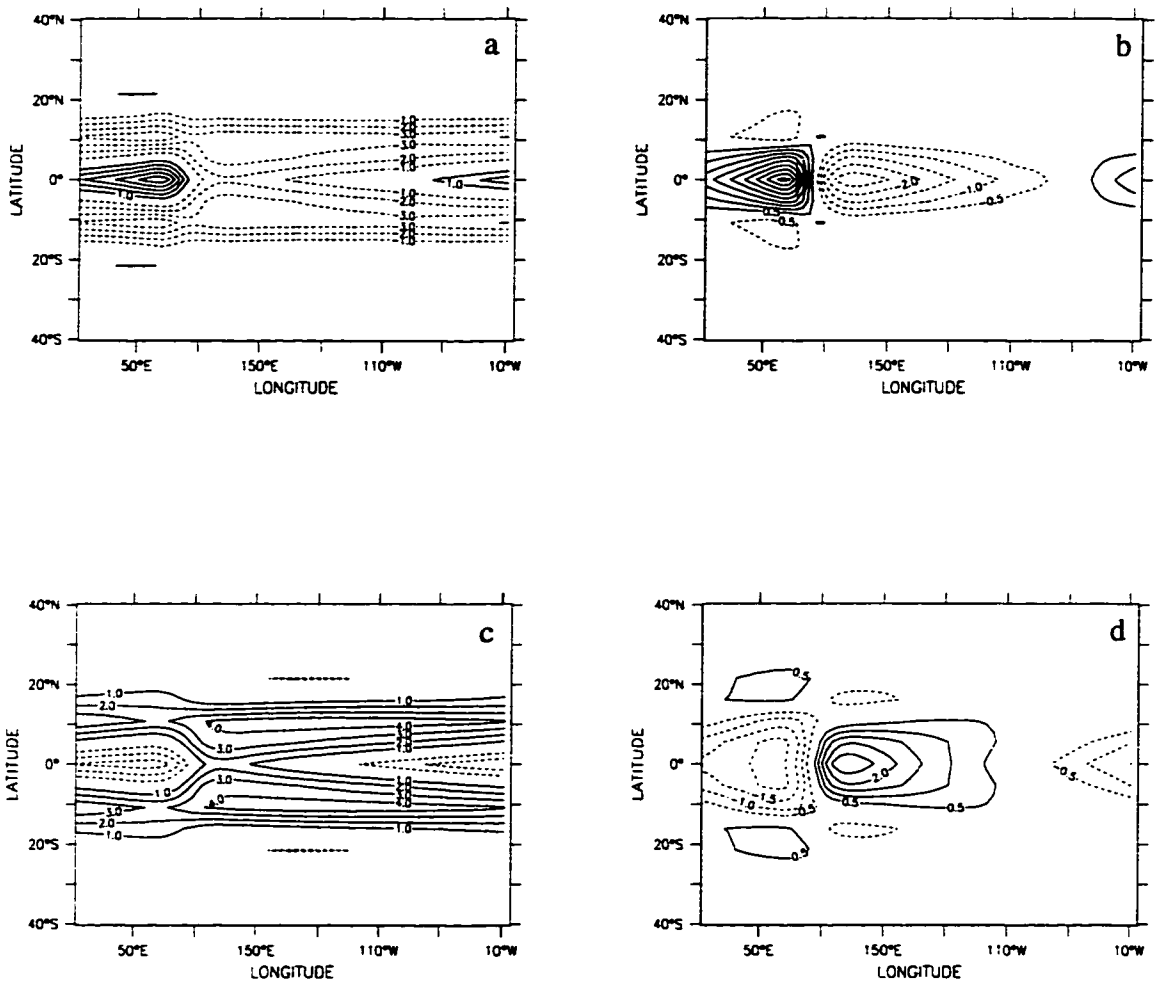

Figure 6.6: Zonal velocities at different altitudes for the Newtonian-cooling-alone-case. Panel a and c are zonal velocities at 675 hPa and 325 hPa, respectively. Panel b and d are the same as panel a and panel c, but with the zonal mean removed. Cotour interval is 1.0 ms^{-1} in panel a and c, and 0.5 ms^{-1} in panel b andl d. The zero contour lines are not shown.

Newtonian-Cooling-Alone-Case

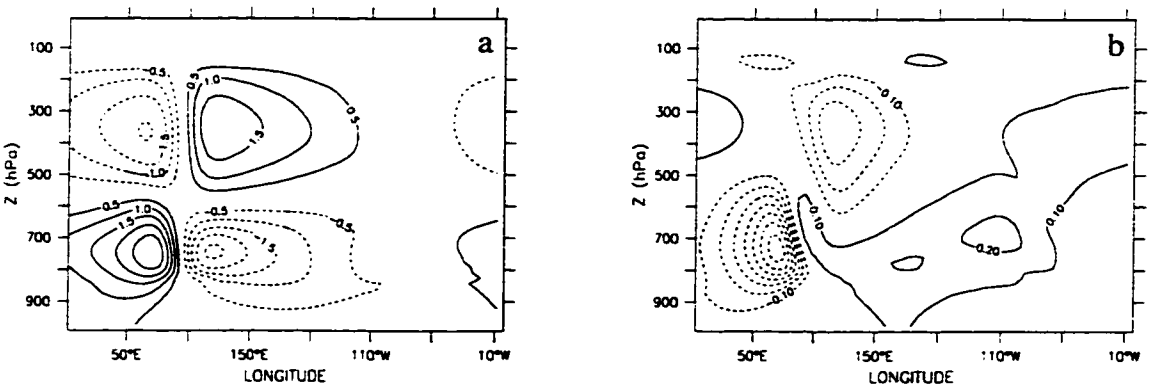

Figure 6.7: Zonal velocity anomalies (i.e., the zonal wind minus the zonal mean zonal wind) at different latitude bands for the Newtonian-cooling-alone-case. Panel a is for the latitude band from the Equator to $10°N$, and panel b is for the latitude band from $10°N$ to $20°N$. Contour interval is 0.5 ms^{-1} in panel a, and 0.1 ms^{-1} in panel b. The zero contour lines are not shown.

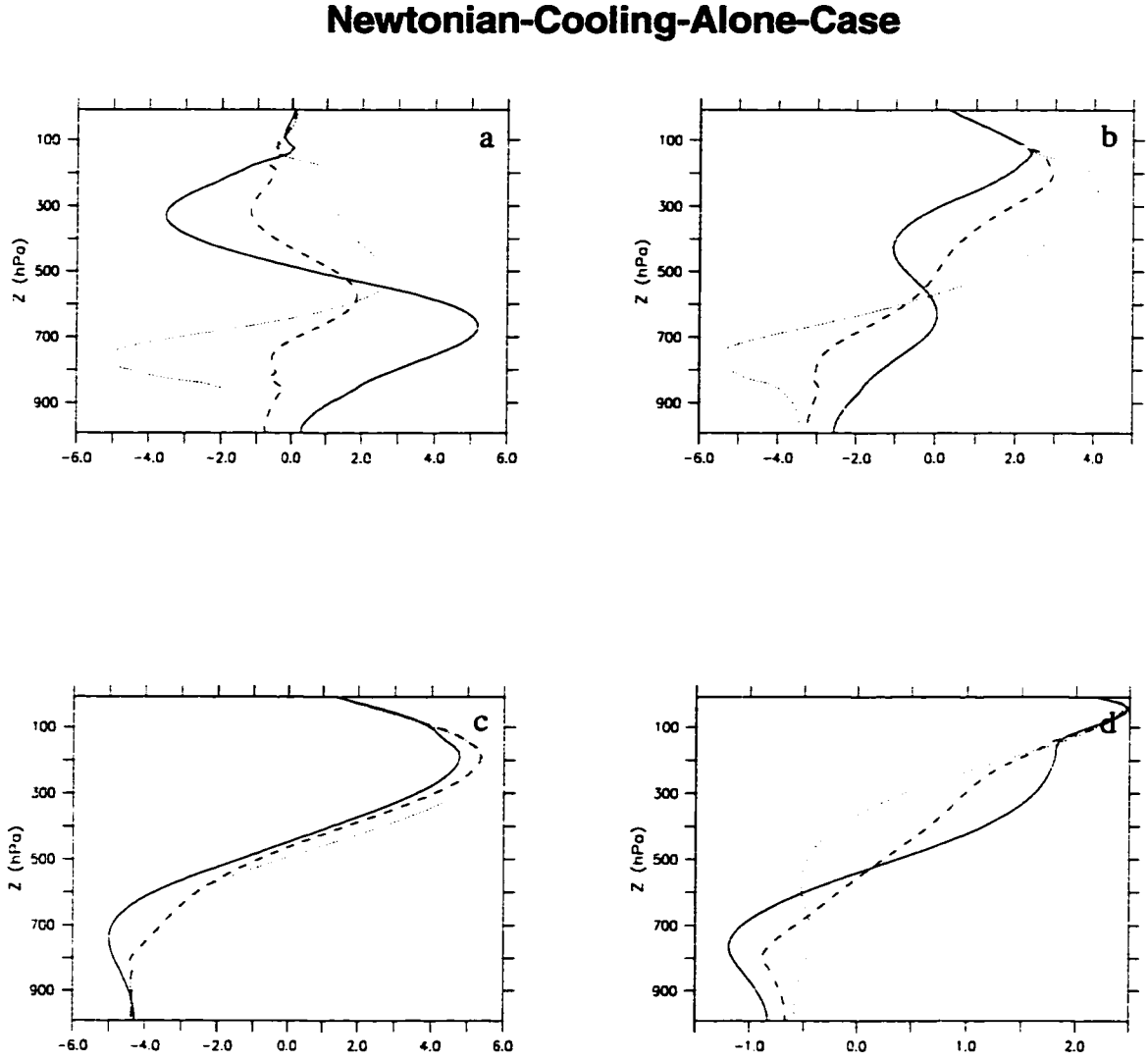

Figure 6.8: Vertical profiles of zonal velocity at different locations for the Newtonian-cooling-alone-case. Panel a is at the Equator; panel b is at $5.4°N$; panel c is at $11.7°N$; panel d is at $16.1°N$. Solid lines are at W; dashed lines are at C; dotted lines are at E. The unit along the abscissa is 1.0 ms^{-1}.

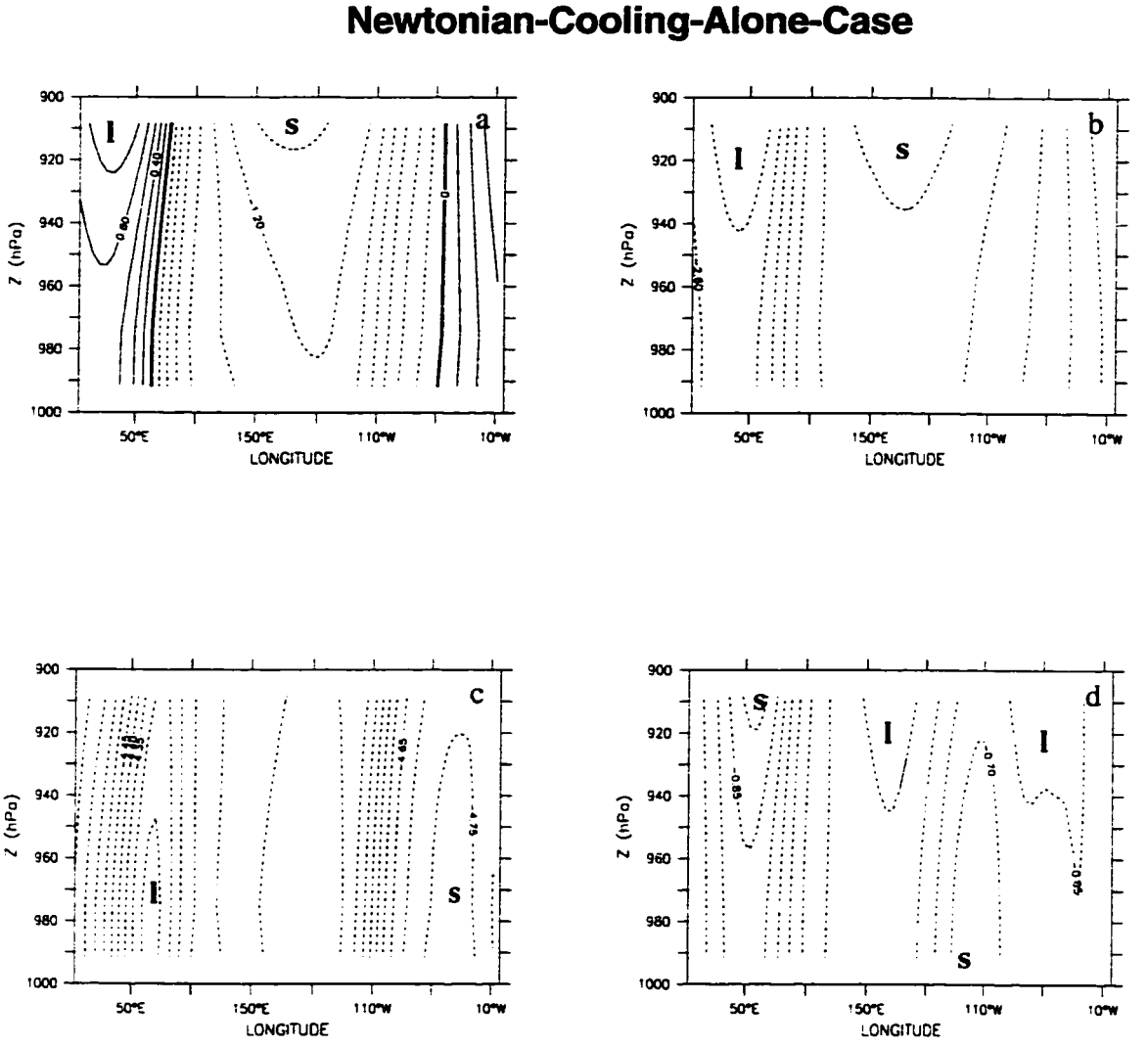

Figure 6.9: Zonal velocities at different latitudes below 900 hPa for the Newtonian-cooling alone-case. Panel a is at the Equator; panel b is at $5°N$; panel c is at $11°N$; panel d is at $16°N$. In each panel, "l" represents a maximum westerly (or minimum easterly) center, and "s" represents a mixiumum easterly (or minimum westerly) center. Contour intervals are 0.2 ms^{-1} in panel a and panel b, and 0.05 ms^{-1} in panel c and panel d.

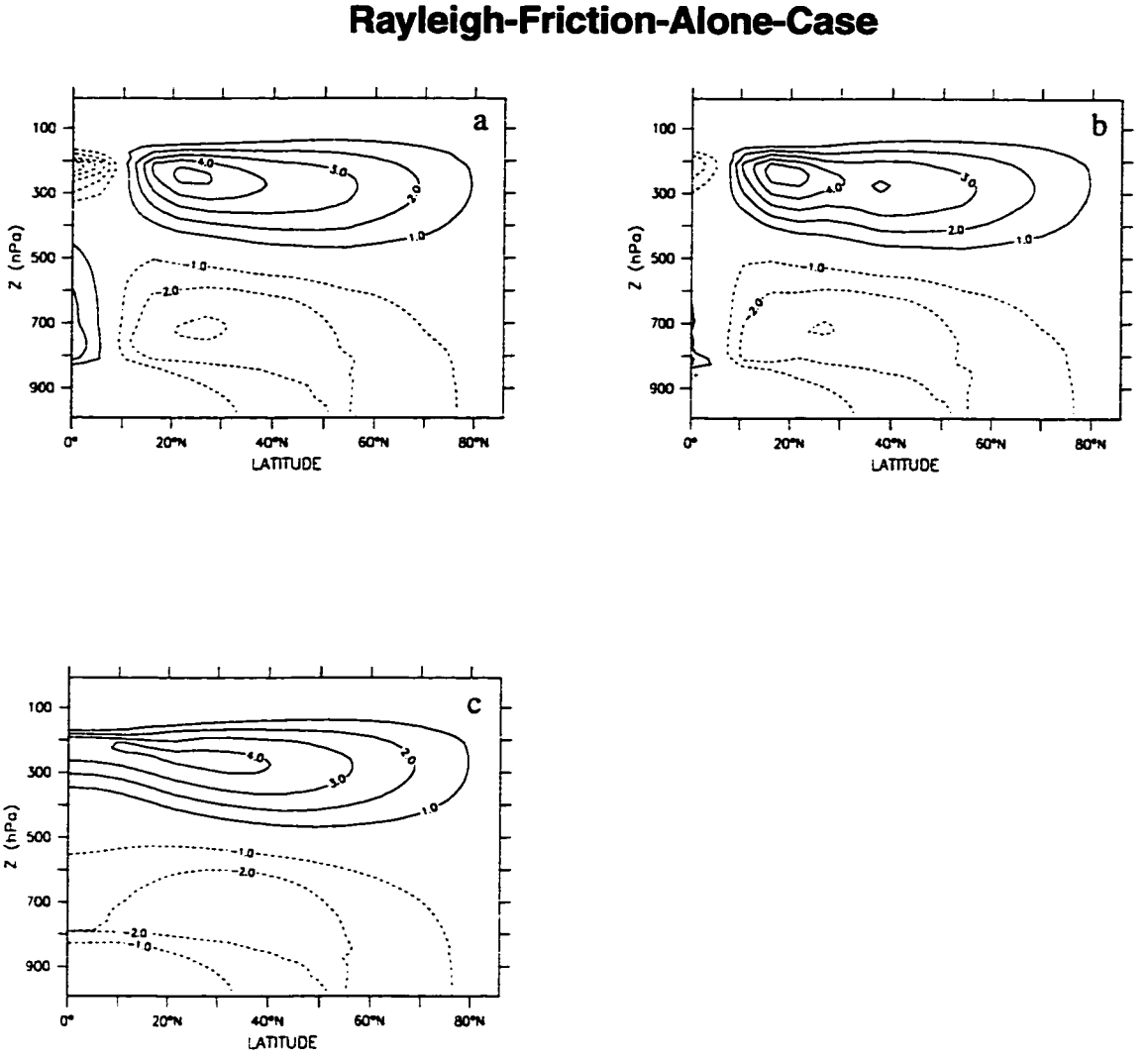

Figure 6.10: Zonal velocities at different longitudes for the Rayleigh-friction-alone-case. Solid lines represent westerlies, and dashed lines represents easterlies. Panel a is at $53.4°E$; panel b is at $92.8°E$; panel c is at $132.2°E$. Contour interval is 1.0 ms^{-1} in every panel. Zero contour lines are not shown.

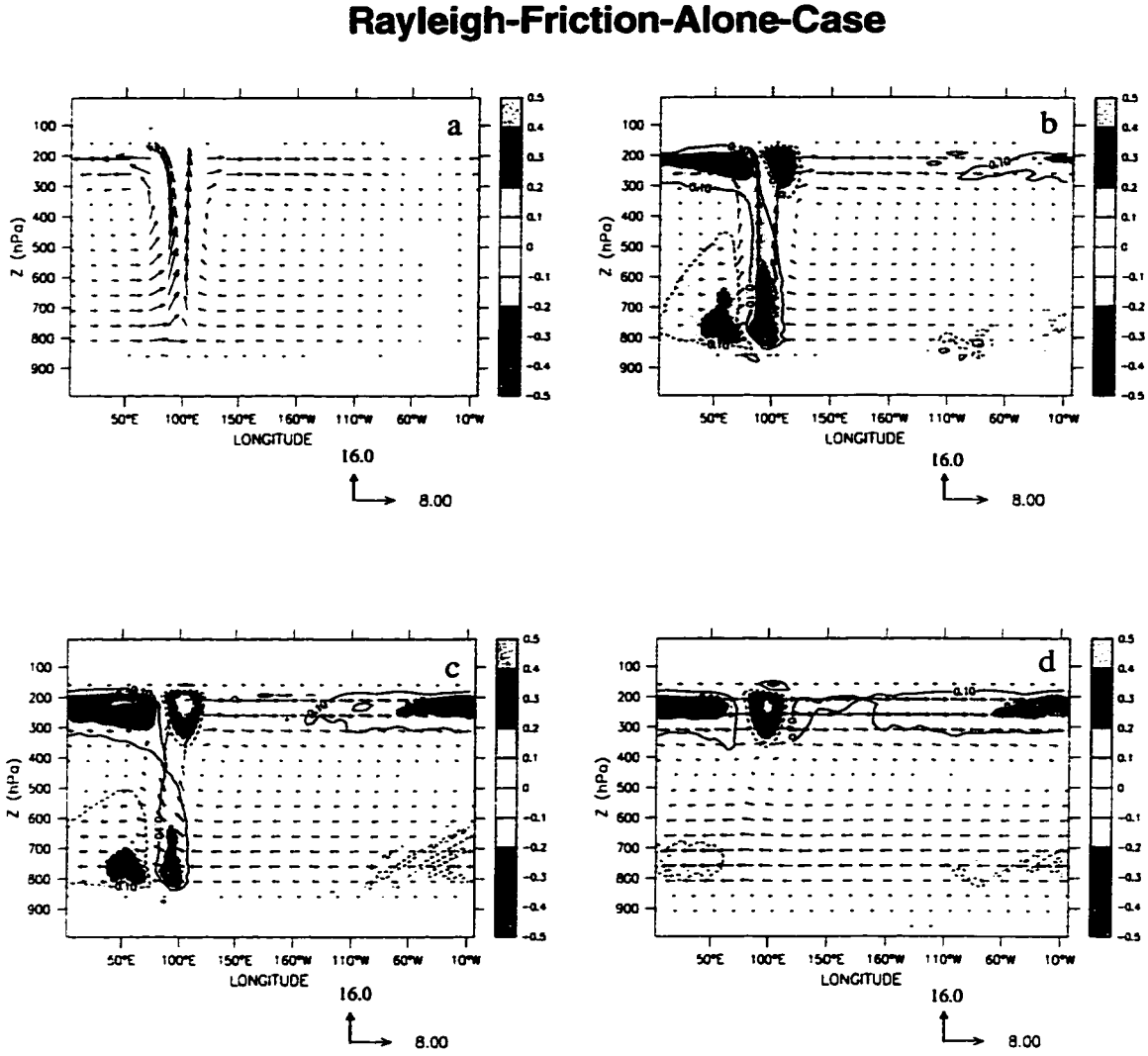

Figure 6.11: The zonal overturning circulations at different latitudes for the Rayleigh-friction-alone-case. The vector field of zonal velocity (with unit ms^{-1}) and vertical velocity ($-dp/dt$ with unit $hPa \cdot day^{-1}$) are superposed on the contoured meridional velocity (with contour interval 0.1 ms^{-1}). The zonal velocity and the vertical velocity are scaled separately, and are shown under each panel, respectively. Panel a is at the Equator; panel b is at $5.4°N$; panel c is at $11.7°N$; panel d is at $16.1°N$.

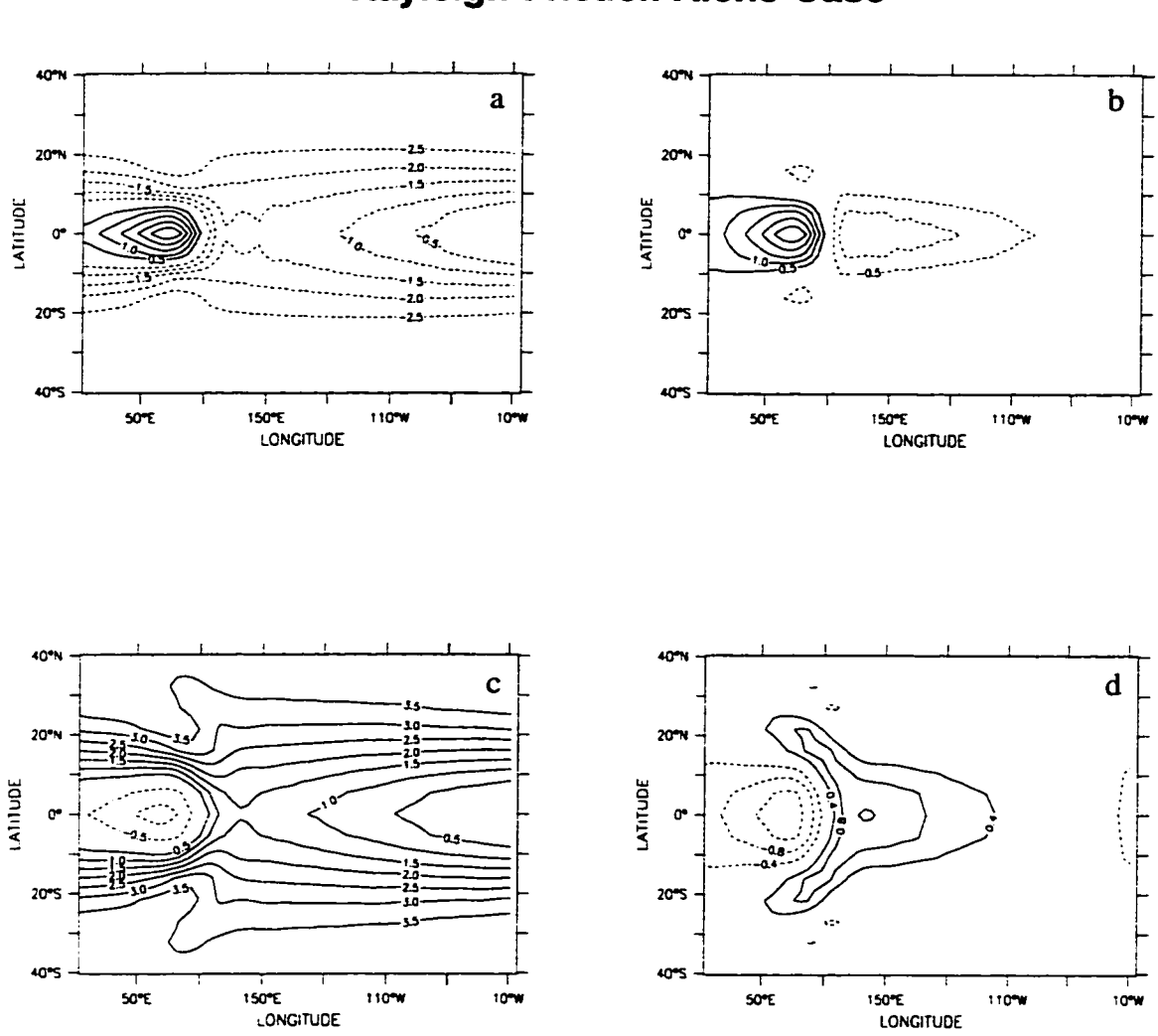

Figure 6.12: Zonal velocities at different altitudes for the Rayleigh-friction-alone-case. Panel a and panel c are zonal velocities at 675 hPa and 325 hPa, respectively. Panel b and panel d are the same as panel a and panel c, respectively, but with the zonal mean removed. Contour intervals are 0.5 ms^{-1} in panel a, panel b, panel c, and 0.4 ms^{-1} in panel d. The zero contour lines are shown.

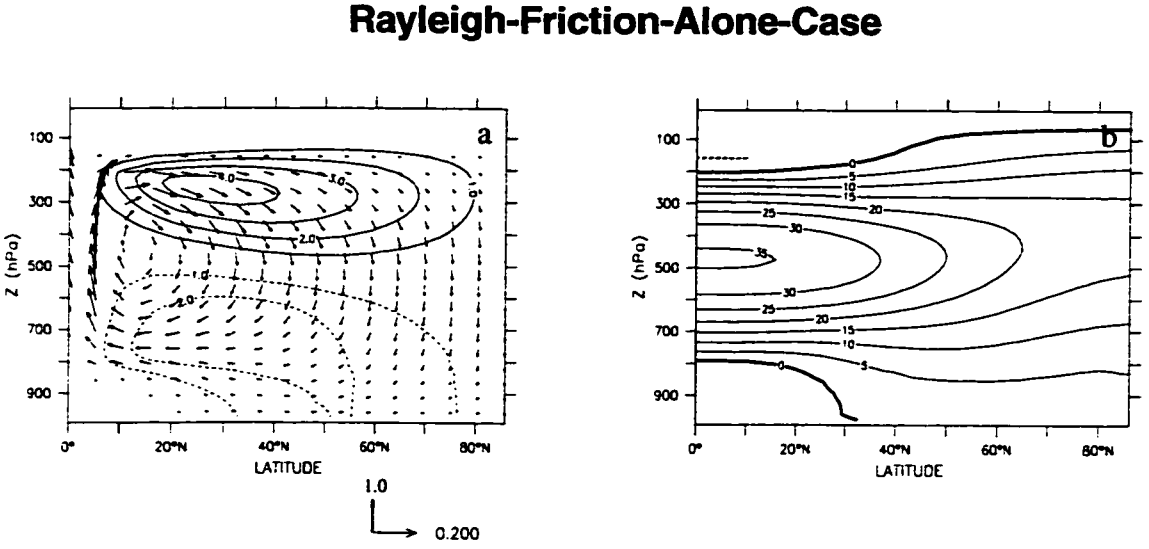

Figure 6.13: Zonally averaged physical fields for the Rayleigh-friction-alone-case. In panel a, the vector field of meridional velocity (with unit ms^{-1}) and vertical velocity ($-dp/dt$ with unit $hPa \cdot day^{-1}$) is superposed on the contoured zonal velocity (with contour interval 1.0 ms^{-1}). The zonal velocities and the vertical velocities are scaled separately, and are shown under each panel, respectively. In panel b, zonally averaged temperature perturbation field is plotted with contour interval of 5 $°C$.

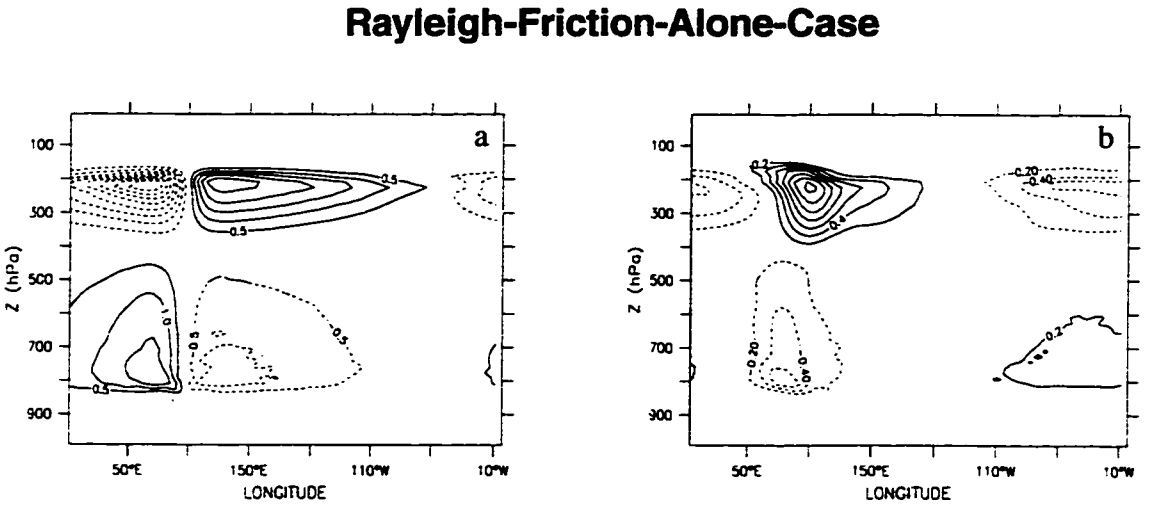

Figure 6.14: Zonal velocity anomalies (i.e., the zonal wind minus the zonal mean zonal wind) at different latitude bands for the Rayleigh-friction-alone-case. Panel a is for the latitude band from $0°$ to $10°N$, and panel b is for the latitude band $10°N$ to $20°N$. Contour intervals are 0.5 ms^{-1} and 0.2 ms^{-1} in panel a and panel b, respectively. The zero contour lines are not shown.

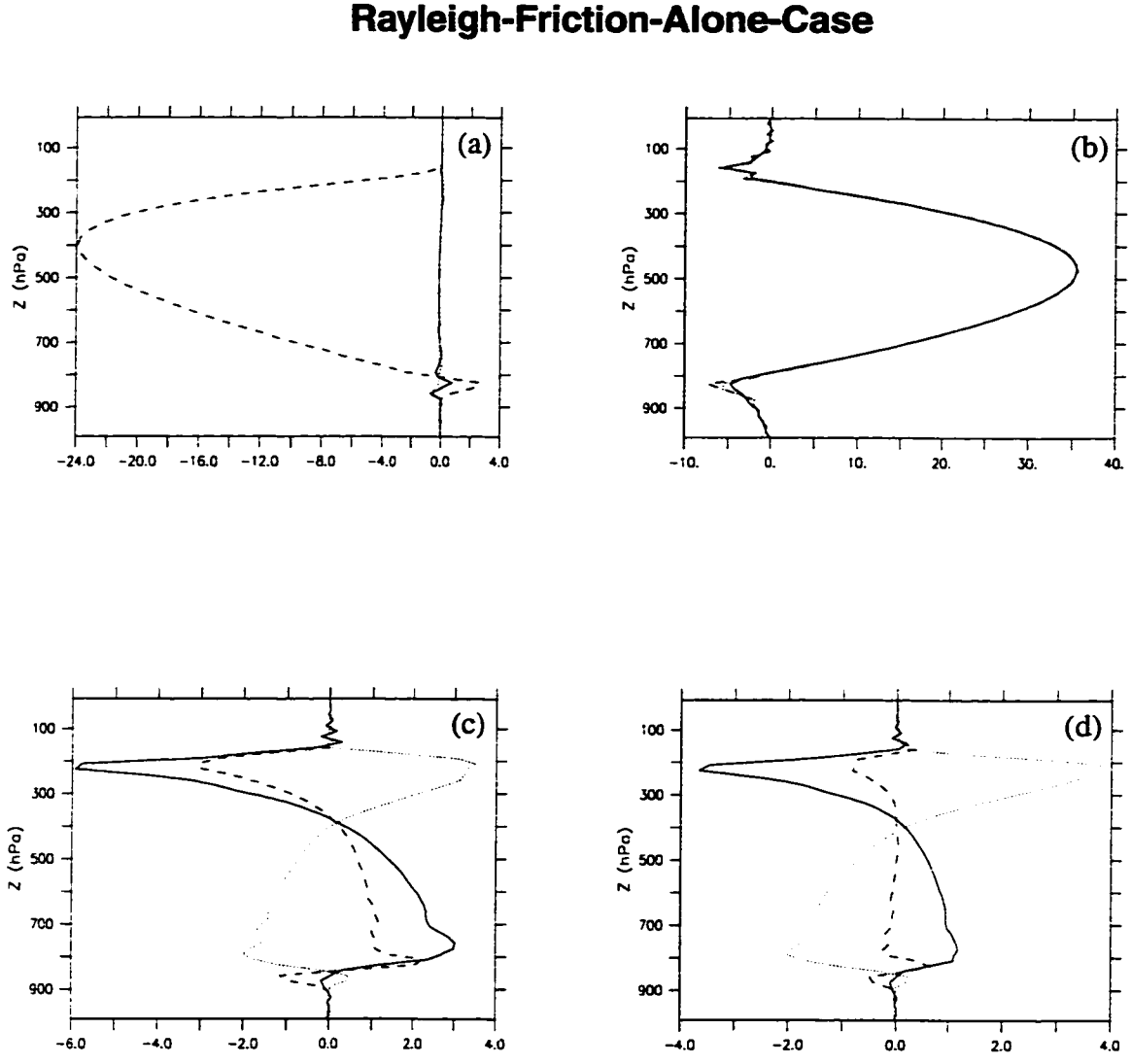

Figure 6.15: Vertical profiles of the vertical velocities (panel a), the temperature perturbations (panel b) at the Equator, and the zonal velocities at different latitudes (panel c is at the Equator; panel d is at $5.4°N$; panel e is at $11.7°N$; panel f is at $16.1°N$) for the Rayleigh-friction-alone-case. Solid lines are at $53.4°E$, dashed lines are at $92.8°E$, and dotted lines are at $132.2°E$. The units along the abscissa are hPa/day, $°C$, and ms^{-1} for the vertical velocity, the temperature perturbation, and the zonal velocity, respectively.

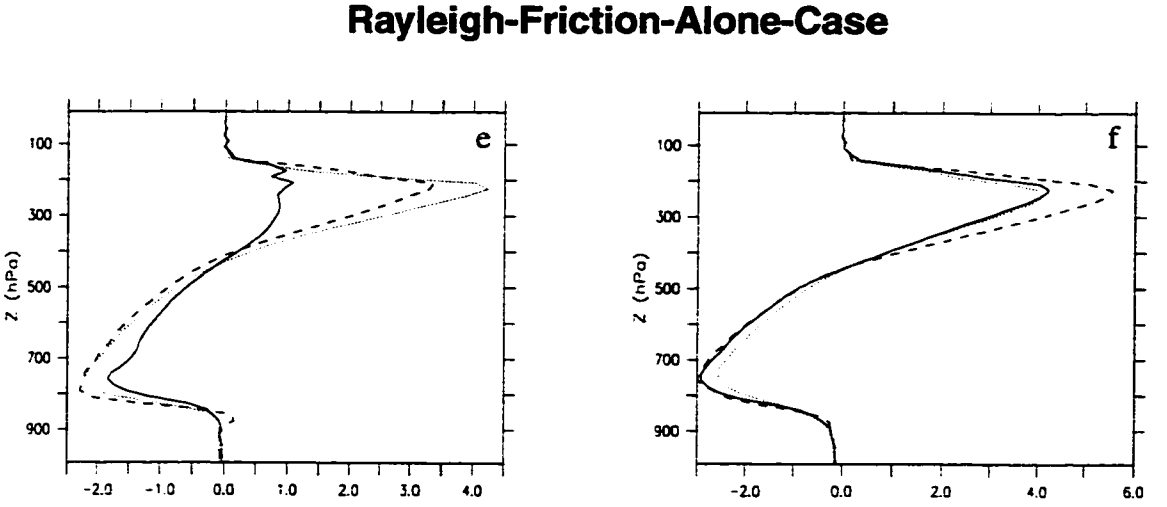

Figure 6.15 (continue)

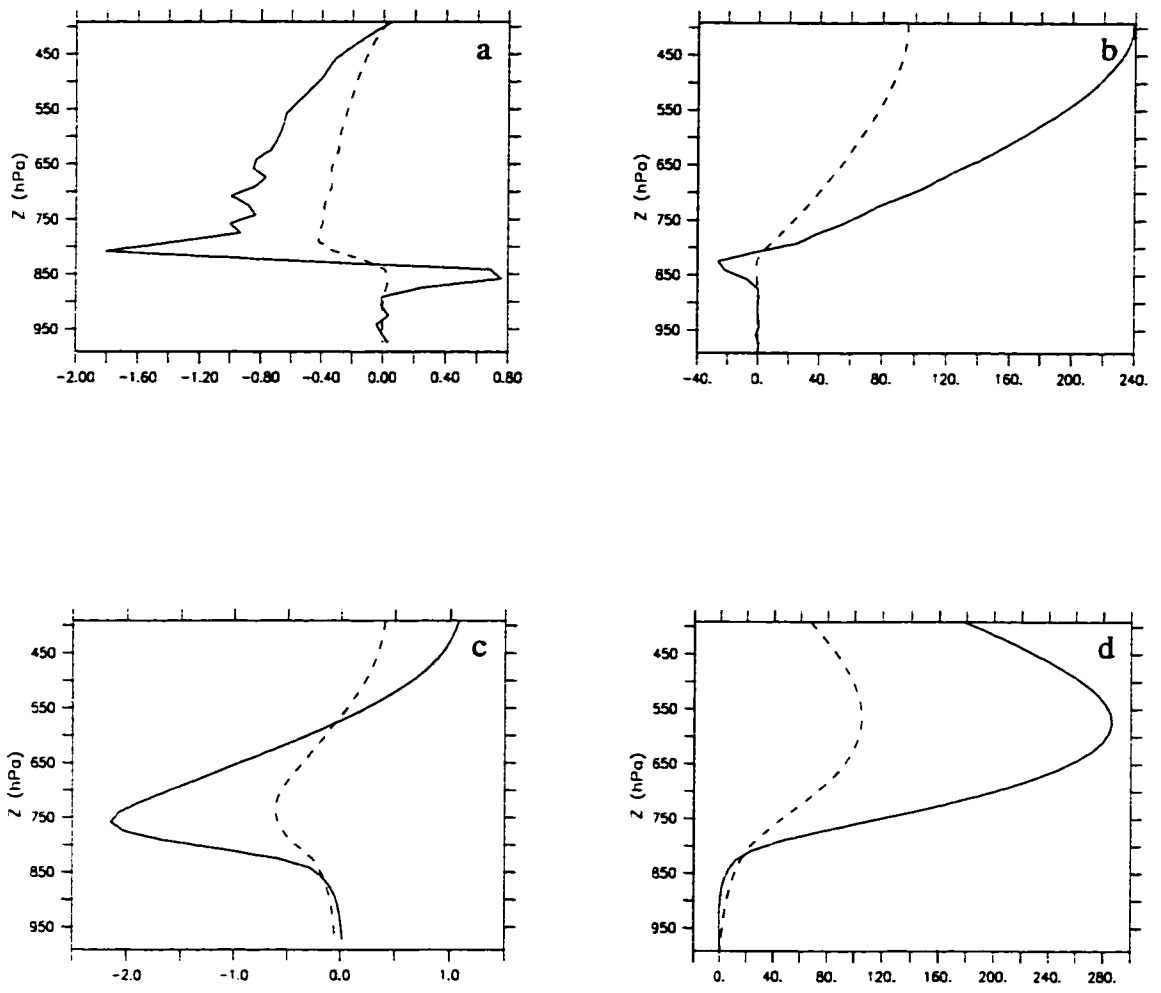

Figure 6.16: The vertical profiles of the divergence ($10^{-6}s^{-1}$) (panels a and c) and the vertically integrated mass convergence ($kg \cdot day^{-1} \cdot m^{-2}$) from the surface to different altitudes (panels b and d) for both the Rayleigh-frinction-alone-case (panels a and b) and the Newtonian-cooling-alone-case (panels c and d). Solid lines represent the quantities at the center of the heat source. Dashed lines represent the quantities averaged over a rectangle area from $70°E$ to $115°E$ and from $11°S$ to $11°N$.

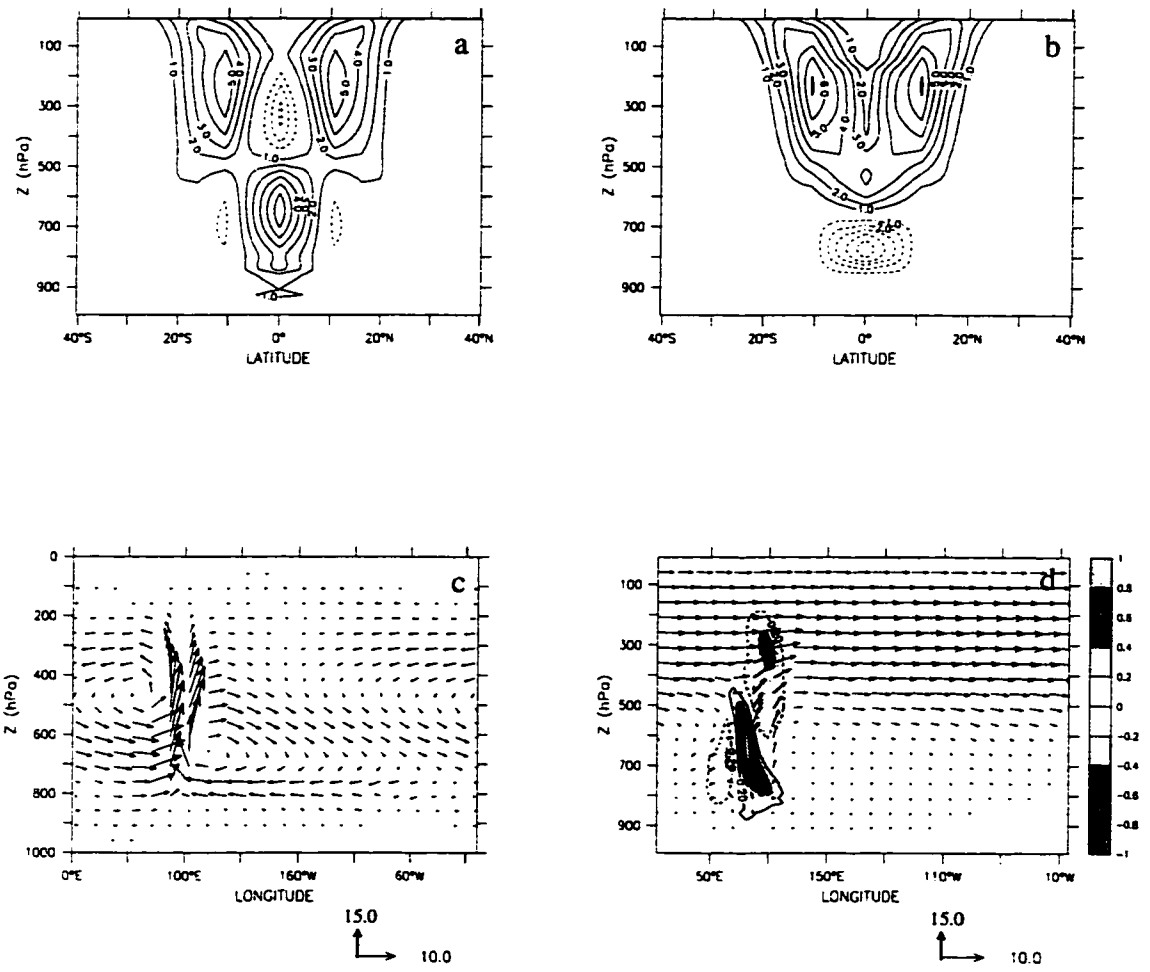

Figure 6.17: Selected results from the case with uniform Newtonian cooling and a simple frictional boundary layer. Panels a and b are the zonal velocities at $53.4°E$ and $132.2°E$, respectively. Westerlies are represented by solid lines, and easterlies are represented by dashed lines. Contour interval is 1.0 ms^{-1} in both panels, and the zero contour lines not shown. Panel c and d show the zonal overturning circulation at $0°$ and $10.7°N$, respectively. The vector field of zonal velocity (with unit ms^{-1}) and vertical velocity ($-dp/dt$ with unit $hPa \cdot day^{-1}$) are superposed on the contoured meridional velocity (with contour interval 0.2 ms^{-1}). The zonal velocities and the vertical velocities are scaled separately, and are shown under each panel.

Chapter 7
CONCLUSIONS

This dissertation is aimed at understanding the circulations driven by thermal sources in the tropical atmosphere and at revealing how and under what conditions strong surface winds can be driven by these thermal sources. We began with the existing theory of thermally driven waves in the tropics to explore the vertical propagation of forced signals. After discussing the problems associated with the tidal approach, we developed a vertical decomposition for the governing equations (linearized on an equatorial beta-plane) in a vertically semi-bounded tropical atmosphere. Various vertical heating profiles were projected onto the vertical eigenfunctions, and the relationship between the vertical structure of the heating and the three-dimensional structure of the forced circulation was investigated. The resulting shallow water equations were then solved in the presence of different combinations of Rayleigh friction and Newtonian cooling. The effect of different zonal domains (cyclic vs. infinite) on the solutions to the shallow-water system was also discussed. Finally, numerical experiments were carried out to verify the analytical results.

We first confirmed the completeness of the eigenfunctions in a meridionally unbounded equatorial beta-plane defined by the meridional eigenvalue-eigenfunction problem. In addition to the eigenfunctions with discrete positive eigenvalue (historically called "the equivalent depth") that had previously been discovered and discussed in many published studies, the eigenfunctions with negative eigenvalue were derived and discussed. The eigenfunctions on an equatorial beta-plane were compared to the corresponding eigenfunctions (Hough functions) defined by the Laplace's tidal equation on a spherical domain. By calculating the projection of a heat source onto the meridional eigenfunctions, we found that the large-scale heating mainly projects onto the meridional

eigenfunctions (modes) with moderately large negative eigenvalue at low frequencies. Hence, only those meridional modes with negative eigenvalue are important to the solutions for the tropical circulations forced by large-scale thermal sources.

The low level circulations, especially the surface winds, that are driven by an elevated large-scale low-frequency heat source, are dramatically affected by the presence of thermal damping. Although our results show that the vertical group velocities associated with the discrete modes with positive equivalent depth are too small to account for the surface winds at low frequencies in a viscous medium, the meridional eigenfunctions with moderately large negative equivalent depth (eigenvalue) do support strong, vertically uniform flows under the heating.

Since the tidal approach can not deal with an atmosphere under both momentum and thermal damping, the shallow water approach is often used to solve the problem of thermally forced tropical atmosphere. However, many previous theoretical studies imposed an artificial rigid lid at the top of the atmosphere to generate the vertically standing modes. Such a lid generally prevents the forced signals from radiating to space and artificially induces the vertical free modes. Furthermore, the horizontal gravity wave speed of each vertically standing mode is quite sensitive to where the lid is located. To overcome these drawbacks, we have found the vertical eigenfunctions in a vertically semi-bounded domain. These eigenfunctions include one discrete mode (Lamb mode) and a continuous spectrum of eigenfunctions. By using these eigenfunctions to decompose the thermally forced linear atmosphere in the tropics, we further found that the three-dimensional structure of the forced circulations is very sensitive to the vertical structure of thermal heating. When the heating is deep, it projects more onto the vertical modes with relatively large equivalent depth (and large horizontal gravity wave speed), and the signals forced by deep heating can propagate farther away from the heating before they are significantly

damped than those forced by shallow heating. Since thermal heating often projects onto a wide spectrum of vertical modes, the forced signals associated with modes with relatively slower propagation speeds are more easily damped than those associated with modes with relatively faster propagation speeds under the same damping. Hence, the effective gravity wave speeds that characterize the horizontal propagation speed of the total forced signals at different locations are different; they increase with distance away from the heating.

In the presence of different Rayleigh friction and Newtonian cooling, it is the effective equatorial radius of deformation, rather than the equatorial radius of deformation, characterize the meridional extent of the forced response in a shallow water system. The effective equatorial radius of deformation of a shallow water system is the equatorial radius of deformation of that shallow water system multiplied by the fourth root of Prandtl number (the ratio between the Rayleigh friction rate and the Newtonian cooling rate). The effective equatorial radius of deformation of a shallow water system is very large when Rayleigh friction dominates and very small when Newtonian cooling dominates. The turning point of any single parabolic cylinder function can be outside the heating latitudes in the Rayleigh-friction-dominant case, and therefore, the total forced response can extend to very high latitude. For the Newtonian-cooling-dominant case, however, almost all the parabolic cylinder functions onto which the forcing has significant projection have their turning points inside the latitudinal boundaries of the heating; and the total response is confined to the heating latitudes.

The zonal decay scale of a shallow water system is characterized by the product of the gravity wave speed of the shallow water system and the damping time scale, which is proportional to the inverse of the square root of the product of the Rayleigh friction rate and the Newtonian cooling rate. In the cases when both Rayleigh friction and Newtonian cooling are quite weak or when either Rayleigh friction or Newtonian cooling is diminish-

ingly small, the zonal decay scale becomes very large. In these cases, a significant amount of the forced signals can propagate a great distance along the equator before being significantly damped and therefore can interfere with the signal coming from the opposite direction. The net results in a zonally cyclic domain are therefore different from those in an zonally unbounded domain in which only the Kelvin signal is seen to the east of the heating and only Rossby signals are seen to the west of the heating. The response to a zonally isolated heating is almost zonally uniform outside the heating longitudes in a zonally cyclic domain, especially in both *the Rayleigh-friction-dominant case* and *the Newtonian-cooling-dominant case.*

Newtonian cooling homogenizes the atmospheric motion in the vertical, and a strong, vertically uniform wind is found below the bottom of the heat source. When Rayleigh friction serves as the only damping in the tropical atmosphere, however, there is not much interaction in the vertical between the forced and unforced atmospheric layers: all the energy put into a layer is dissipated within that layer. Hence, no surface wind is found unless the heat source reaches close to the surface or possibly down to within the planetary boundary layer. It was also shown that only when momentum damping is fairly strong can the signal in the tropics extend to the extratropics and can a strong meridional overturning circulation form and the strong momentum damping also causes the response to be vertically confined to the layer in which the heat source resides. Hence, our results are consistent with those of Schneider and Lindzen (1977) and Battisti and Ovens (1995) in that they imply the low-level flow in the deep tropics (i.e., between 10 and 10) is not associated with a strong Hadley circulation driven by an elevated tropical heat source: it is due to the surface pressure gradients generated by the hydrostatic adjustment to SST gradients. The numerical results in a dry primitive equation GCM confirmed the analytical results.

Finally, a numerical simulation showed that the introduction of a simple boundary

layer with strong momentum damping dramatically reduces the surface circulation that was supported by the elevated heating in the Newtonian-cooling-alone case. However, It remains to be seen to what extent this conclusion is sensitive to the formulations of friction and thermal damping and especially to the location of the base of the heating and its relationship to the top of the boundary layer.

LIST OF REFERENCES

Abramowitz, M. and I. A. Stegun, 1965: *Handbook of mathematical functions.* Dover, 1064pp.

Bantzer, C. H., and J. M. Wallace, 1996: Intraseasonal variability in tropical mean temperature and precipitation and their relation to tropical 40-50 day oscillation. *J. Atmos. Sci.*, **53**, 3032-3045.

Barnett, T. P., 1985: Three-dimensional structure of low-frequency pressure variations in the tropical atmosphere. *J. Atmos. Sci.*, **34**, 901-910.

Battisti, D. S., and D. Ovens, 1995: The dependence of the low-level equatorial easterly jet on Hadley and Walker circulations. *J. Atmos. Sci.*, **52**, 3911-3931.

Cane, M. A., and E. Sarachik, 1993: *Course on ocean-atmosphere interactions in tropics.* International Centre for Science and High Technology.

Chang, C.-P., 1977: Viscous internal gravity waves and low-frequency oscillations in the tropics. *J. Atmos. Sci.*, **42**, 2798-2803.

Charney, J.D., and A. Eliassen, 1964: On the growth of the hurricane depression. *J. Atmos. Sci.*, **21**, 68-75.

DeMaria, M., 1985: Linear response of a stratified tropical atmosphere to convective forcing. *J. Atmos. Sci.*, **42**, 1944-1959.

Deser, C., and J. M. Wallace, 1987: El Niño events and their relationship to Southern Oscillation phenomenon. *J. Geophys. Res.*, **92**, 14 189-14 196.

Deser, C., and J. M. Wallace, 1990: Large-scale atmospheric circulation feature of warm and cold episodes in the tropical Pacific. *J. Climate*, **3**, 1254-1281.

Dickinson, R. E., and M. A. Geller, 1968: A generalization of 'tidal theory with Newtonian cooling'. *J. Atmos. Sci.*, **25**, 932-933.

Eliassen, E., and B. Machenhauer, 1974: On spectral representation of the vertical variation of the meteorological fields in numerical integration of a primitive equation model. GARP WGNE Report No. 7, 83-93.

Flattery, T. W., 1967: Hough-function. *Technical Report No. 21*, Department of Geophysical Sciences, University of Chicago.

Frank, W. M., and J. L. McBride, 1989: The vertical distribution of heating in AMEX and Gate cloud clusters. *J. Atmos. Sci.*, **46**, 3464-3478.

Friedman, B., 1956: *Principles and techniques of applied mathematics*. Jone Wiley & Sons, Inc., 315pp.

Geisler, J. E., 1981: A linear model of the Walker circulation. *J. Atmos. Sci.*, **38**, 1390-1400.

Geisler, J. E., and D. E. Stevens, 1982: On the vertical structure of damped steady circulation in the tropics. *Quart. J. Roy. Meteor. Soc.*, **108**, 87-94.

Gill, A. E., 1980: Some simple solutions for heat induced tropical circulations. *Quart. J. Roy. Meteor. Soc.*, **106**, 447-462.

Gill, A. E., 1982: *Atmosphere-Ocean Dynamics*. Academic Press, Inc., 662pp.

Haltiner, G. J., and R. T. Williams, 1980: *Numerical prediction and dynamic meteorology (2rd edition)*, John Wiley & Sons, 477pp.

Harrasma, R. J., and J. D. Opsteegh, 1989: Nonlinear response to anomalous tropical forcing. *J. Atmos. Sci.*, **46**, 3240-3255.

Hartmann, D. L., H. H. Hendon, and R. A. Houze, Jr., 1984: Some implication of mesoscale circulations in tropical cloud clusters for large-scale dynamics and climate. *J. Atmos. Sci.*, **41**, 113-121.

Hayashi, Y., 1976: Non-singular resonance of equatorial waves under the radiation condition. *J. Atmos. Sci.*, **33**, 183-201.

Held, I. M., R. L. Panetta, and R. T. Pierrehumbert, 1985: Stationary external Rossby waves in vertical shear. *J. Atmos. Sci.*, **42**, 865-883.

Hendon, H. H., and M. L. Salby, 1996: Planetary-scale circulations forced by intraseasonal variations of observed convection. *J. Atmos. Sci.*, **53**, 1751-1758.

Holl, P., 1970: The completeness of the orthogonal system of the Hough functions. *Nachrichten der Akademia der Wissenschaften in Göttingen II. Mathematisch-Physikalische Klasse*, **7**, 159-168.

Holton, J. R., 1975: *The dynamic meteorology of the stratosphere and mesosphere*. Am. Met. Sco., Boston. Mass., 218pp.

Holton, J. R., 1992: *An introduction to dynamic meteorology.* Academic Press, 511pp.

Holton, J. R., and D. E. Cotton, 1972: A diagnostic study of the vorticity balance at 200 bm in the tropics during the northern summer. *J. Atmos. Sci.*, **29**, 1124-1128.

Kasahara, A., 1984: The linear response of a stratified global atmosphere to tropical thermal forcing. *J. Atmos. Sci.*, **41**, 2217-2237.

Kato, S., 1966: Diurnal atmospheric oscillation. I. Eigenvalues and Hough functions. *J. Geophys. Res.*, **71**, 3201-3209.

Kato, T., 1997: The linear response of a global atmosphere to mobile heating, Part 2: Dependency on Rayleigh friction and Newtonian cooling. *J. Meteor. Soc. Japan*, **75**, 867-884.

Kuo, H. L., 1965: On formation and intensification of tropical cyclones through latent heat release by cumulus convection. *J. Atmos. Sci.*, **22**, 40-63.

Lau, K.-M., and H. Lim, 1982: Thermally driven motions in an equatorial β-plane: Hadley and Walker circulations during the winter monsoon. *Mon. Wea. Rev.*, **110**, 336-353.

Lau, K.-M., and L. Peng, 1987: Origin of low-frequency (intraseasonal) oscillations in the tropical atmosphere. Part I: Basic theory. *J. Atmos. Sci.*, **44**, 950-972.

Lindzen, R. S., 1966: On the theory of the diurnal tide. *Mon. Wea. Rev.*, **94**, 295-301.

Lindzen, R. S., 1967: Planetary waves on beta-planes. *Mon. Wea. Rev.*, **95**, 441-451.

Lindzen, R. S., 1968: Vertically propagating waves in an atmosphere with Newtonian cooling inversely proportional to density. *Can. J. Phys.*, **46**, 1835-1840.

Lindzen, R. S., and T. Matusno, 1968: On the nature of large scale wave disturbances in the equatorial lower stratosphere. *J. Meteor. Soc. Japan*, **46**, 215-220.

Lindzen, R. S., and S. Nigam, 1987: On the role of sea surface temperature gradients in forcing low-level winds and convergence in the tropics. *J. Atmos. Sci.*, **44**, 2418-2436.

Lindzen, R. S., E. S. Batten, and J.-W. Kim, 1968: Oscillations in atmosphere with tops. *Mon. Wea. Rev.*, **96**, 133-140.

Longuet-Higgins, M. S., 1968: The eigenfunctions of Laplace's tidal equations over a

sphere. *Phil. Trans. Roy. Soc. London*, **A262**, 511-607.

Machenhauer, B., and R. Daley, 1974: Hemispheric spectral model. GARP Publication Series No. 14, 226-251.

Mapes, B. E., and R. A. Houze, 1995: Diabatic divergence profiles in western Pacific mesoscale convective system. *J. Atmos. Sci.*, **52**, 1807-1828.

Martinsen, E. A., and J. E. Weber, 1981: Frictional influence on internal Kelvin waves. *Tellus*, **33**, 402-410.

Matsuno, T., 1966: Quasi-geostrophic motions in the equatorial area. *J. Meteor. Soc. Japan*, **44**, 25-43.

McCreary, J. P., 1981: A linear stratified ocean model of the equatorial undercurrent. *Philos. Trans. Roy. Soc. London*, **A298**, 603-635.

Mitchell, T. P., and J. M. Wallace, 1996: ENSO Seasonality: 1950–78 versus 1979–92. *J. Climate*, **9**, 3149-3161.

Mizzi, A., and J. Tribbia, 1995: Vertical spectral representation in primitive equation models of the atmosphere. *Mon. Wea. Rev.*, **123**, 2426-2446.

Mofjeld, H. O., 1980: Effects of vertical viscosity on Kelvin waves. *J. Phys. Oceanogr.*, **10**, 1039-1050.

National Physical Laboratory, 1955: *Tables of Weber parabolic cylinder functions*. Her Majesty's Stationery Office, London, 233pp.

National Physical Laboratory, 1960: *Tables of Weber parabolic cylinder functions and other functions for large arguments*. Her Majesty's Stationery Office, London, 40pp.

Neelin, J. D., 1989: On the interpretation of the Gill model. *J. Atmos. Sci.*, **46**, 2466-2468.

Newell, R. E., and Z.-X. Wu, 1992: The interrelationship between temperature changes in the free atmosphere and sea surface temperature changes. *J. Geophys. Res.*, **97**, 3693-2709.

Ooyama, K., 1969: Numerical simulation of life cycle of tropical cyclones. *J. Atmos. Sci.*, **26**, 3-40.

Peixoto, J. P., and A. H. Oort, 1992: *Physics of Climate*. American Institute of Physics,

520pp.

Philander, S. G., 1990: *El Niño, La Niña, and the Southern Oscillation*. Academic Press, Inc., 293pp.

Rasmusson, E. M., and T. H. Carpenter, 1982: Variation in tropical sea surface temperature and surface wind fields associated with the Southern Oscillation / El Niño. *Mon. Wea. Rev.*, **110**, 354-384.

Reed, R.J., and E. E. Recher, 1971: The vorticity budget of synoptic-scale wave disturbances in the equatorial western Pacific. *J. Atmos. Sci.*, **28**, 1117-1133.

Robert, A. E., 1966: The integration of a low order spectral form of the primitive meteorological equations. *J. Meteor. Soc. Japan*, **44**, 237-345.

Saravanan, R., and J. C. McWilliams, 1995: Multiple equilibria, natural variability, and climate transitions in an idealized ocean-atmosphere model. *J. Climate*, **8**, 2296-2323.

Sardeshmukh, P. D., and I. M. Held, 1984: The vorticity balance in the tropical upper troposphere of a general circulation model. *J. Atmos. Sci.*, **41**, 768-778.

Schneider, E. K., and R. S. Lindzen, 1977: Axially symmetric steady-state models of the basic state for instability and climate studies. Part I: linearized circulations. *J. Atmos. Sci.*, **34**, 263-279.

Schneider, E. K., 1977: Axially symmetric steady-state models of the basic state for instability and climate studies. Part II: nonlinear circulations. *J. Atmos. Sci.*, **34**, 280-296.

Shapiro, L. J., 1977: Frictional effects on thermally forced waves. *Tellus*, **29**, 264-271.

Silva Dias, P. L., W. H. Schubert, and M. DeMaria, 1983: Large-scale response of the tropical atmosphere to transient convection. *J. Atmos. Sci.*, **40** 2689-2707.

Silva Dias, P. L., 1986: Vertical mode decomposition and model resolation. *Tellus*, **38A**, 205-214.

Sui, C.-H. and K.-M. Lau, 1989: Origin of low-frequency (intraseasonal) Oscillations in the tropical atmosphere. Part. II: Structure and propagation of mobile wave-CISK modes and their modification by lower boundary forcings. *J. Atmos. Sci.*, **46**, 38-56.

Wallace, J. M., 1971: Spectral studies of tropospheric wave disturbances in the tropical

western Pacific. *Rev. Geophys. Space Phys.*, **9**, 557-612.

Wallace, J. M., E. M. Rasmusson, T. P. Mitchell, V. E. Kousky, E. S. Sarachik, and H. von Storch, 1998: On the structure and evolution of ENSO-related climate variability in the tropical Pacific: Lessons from TOGA. *J. Geophys. Res.*, **103**, 14241-14259.

Wang, T.-A., Y.-L. Lin, H. F. M. Semazzi, and G. S. Janowitz, 1996: Response of a stably stratified atmosphere to large-scale diabatic forcing with applications to wind patters in Brazil and Sahel. *J. Geophys. Res.*, **101**, 7049-7073.

Webster, P. J., 1972: Response of the tropical atmosphere to local steady forcing. *Mon. Wea. Rev.*, **100**, 518-541.

Wu, Z., E. S. Sarachik, and D. S. Battisti, 1997a: Forced planetary waves on an equatorial beta-plane. *11th Conf. on Atmospheric and Oceanic Fluid Dynamics. Tacoma*, WA, Amer. Meteor. Soc., 6-10.

Wu, Z., E. S. Sarachik, D. S. Battisti, 1997b: Thermally driven surface winds on an equatorial beta-plane. *J. Atmos. Sci.*, (accepted).

Wu, Z., D. S. Battisti, and E. S. Sarachik, 1998a: Rayleigh Friction, Newtonian Cooling, and the Linear Response to Steady Tropical Heating. *J. Atmos. Sci.*, (submitted).

Wu, Z., D. S. Battisti, and E. S. Sarachik, 1998b: Vertical structure of convective heating and the three-dimensional structure of the forced circulation in the Tropics. *J. Atmos. Sci.*, (submitted)

Yamagata, T., and S. G. H. Philander, 1985: The role of damped equatorial waves in the oceanic response to winds. *J. Oceanogr. Soc. Japan*, **41**, 345-357.

Yulaeva, E., and J. M. Wallace: The signature of ENSO in global temperature and precipitation fields derived from the microwave sounding unit. *J. Climate*, **7**, 1719-1736.

Zhang, Z., and T. N. Krishnamurti, 1996: A generalization of Gill's heat-induced tropical circulation. *J. Atmos. Sci.*, **53**, 1045-1052.

Zebiak, S. E., 1986: Atmospheric convergence feedback in a simple model for El Niño. *Mon. Wea. Rev.*, **114**, 1263-1271.

Appendix A

SPECTRAL REPRESENTATION OF A DIFFERENTIAL OPERATOR

Let $\mathcal{L}$ be an ordinary self-adjoint differential operator with eigenfunctions $u_1, u_2, \ldots,$ and associated eigenvalues $\lambda_1, \lambda_2, \ldots$. We will assume that the eigenfunctions span the domain of the given operator, and that, in consequence, any square integrable function u can be expanded in the form:

$$u(x) = \sum \alpha_k u_k(x), \tag{A.1}$$

where

$$\alpha_k = (u_k, u), \tag{A.2}$$

i.e., α_k is the projection of u onto u_k.

Now, it follows that

$$\mathcal{L}u(x) = \sum \alpha_k \mathcal{L}u_k(x) = \sum \alpha_k \lambda_k u_k \tag{A.3}$$

and if f denotes a function which is analytic in a region containing the eigenvalues, we define

$$f(\mathcal{L})u(x) = \sum f(\lambda_k)\alpha_k u_k(x). \tag{A.4}$$

For the particular case when $f(t) = (\lambda - t)^{-1}$ we obtain

$$\left(\frac{1}{\lambda - \mathcal{L}}\right)u(x) = \sum \frac{\alpha_k u_k(x)}{\lambda - \lambda_k}. \tag{A.5}$$

The left-hand side of equation (A.5) can be expressed in terms of the Green's function for the differential operator $(\mathcal{L} - \lambda)$. To see this let $w(x) = (\mathcal{L} - \lambda)^{-1} u(x)$; then if $G(x, \xi;\lambda)$ which is defined by $(\mathcal{L} - \lambda)G = \delta(x - \xi)$ is the Green's function for the operator $(\mathcal{L} - \lambda)$ we have

$$w(x) = -\int G(x, \xi;\lambda)u(\xi)d\xi, \tag{A.6a}$$

and consequently

$$\left(\frac{1}{\lambda - \mathcal{L}}\right)u(x) = -\int G(x, \xi;\lambda)u(\xi)d\xi. \tag{A.6b}$$

If now, we integrate equation (A.5) over a large circle of radius R in the complex λ plane, we obtain

$$\frac{1}{2\pi i}\oint_R \frac{u(x)}{\lambda - \mathcal{L}}d\lambda = \sum \frac{1}{2\pi i}\oint_R \frac{\alpha_k u_k(x)}{\lambda - \lambda_k}d\lambda. \tag{A.7}$$

When the radius of the circle increases without bound, the right-hand side includes more and more residues, and we obtain, bearing in mind that necessarily u is also a function of λ,

$$\lim_{R \to \infty} \frac{1}{2\pi i}\oint_R \frac{u(x)}{\mathcal{L} - \lambda}d\lambda = -\sum \alpha_k u_k(x) = -u(x). \tag{A.8}$$

This result, which connects the Green's function with the eigenfunctions, was obtained, as already stressed, using a number of assumptions regarding the existence and completeness of the eigenfunctions. In practice, to overcome these difficulties, the above reasoning is usually followed through in the reverse direction. Starting with a knowledge of the Green's function, $G(x, x_0;\lambda)$, for operator $(\mathcal{L}-\lambda)$ we consider the following integral in the complex λ-plane:

$$\lim_{R\to\infty}\frac{1}{2\pi i}\oint_R \frac{u(x)}{\mathcal{L}-\lambda}d\lambda = \lim_{R\to\infty}\frac{1}{2\pi i}\oint_R\int G(x, \xi;\lambda)u(\xi)d\xi d\lambda, \tag{A.9}$$

and by evaluating this in terms of residues we hope to obtain equation (A.8), this is an expansion of $u(x)$ in terms of the eigenfunctions of $\mathcal{L}$.

When $u(x) = \delta(x-\xi)$, equation (A.9) becomes

$$-\delta(x-\xi) = \lim_{R\to\infty}\frac{1}{2\pi i}\oint_R G(x, \xi;\lambda)d\lambda. \tag{A.10}$$

Appendix B

THE MERIDIONAL EIGENVALUE-EIGENFUNCTION PROBLEM[1]

The *latitudinal structure equation* that, along with its boundary conditions, defines the meridional eigenfunctions that can be written as:

$$\frac{d^2\Psi_\lambda}{dy^2} - \left(k^2 + \beta\frac{k}{\omega}\right)\Psi_\lambda + \lambda(\beta^2 y^2 - \omega^2)\Psi_\lambda = 0, \qquad \text{(B.1)}$$

where λ is an eigenvalue (which is often written as $-1/gh$ with h the equivalent depth), and $\Psi_\lambda(y)$ is the corresponding meridional eigenfunction. Equation (B.1) is identical to equation (3.2). The boundary conditions associated with equation (B.1) are the radiation conditions at infinities. (Equation (B.18) will show that the eigenfunctions resulting from this eigenvalue-eigenfunction problem also satisfy the boundary conditions $\Psi_\lambda \to 0$ as $y \to \pm\infty$, which is commonly used boundary conditions on an equatorial beta-plane.)

The method of spectral representation of a differential operator that is outlined in Appendix A (see Friedman 1956 for details) is used to solve this eigenvalue-eigenfunction problem. The differential operator is therefore

$$\mathcal{L} = \frac{-1}{\beta^2 y^2 - \omega^2}\left[\frac{d^2}{dy^2} - \left(k^2 + \beta\frac{k}{\omega}\right)\right]. \qquad \text{(B.2)}$$

$\omega = \pm\beta y$ are singular points. (Equation (B.18) will show that these singularities are

1. I would like to express my gratitude to Prof. Dennis Moore of NOAA/PMEL for his allowing me to use some of his unpublished results to complete this appendix. It was Prof. Moore who showed me the key steps to obtain equation (B.18), the key result of this appendix.

artificial.) The Green's Function $G(y, y_0;\lambda)$ for the operator $(\mathcal{L}-\lambda)$ satisfies

$$\mathcal{L}G-\lambda G = \delta(y-y_0), \tag{B.3}$$

i.e.,

$$\frac{d^2G}{dy^2}-\left(k^2+\beta\frac{k}{\omega}\right)G+\lambda(\beta^2y^2-\omega^2)G = -(\beta^2y^2-\omega^2)\delta(y-y_0). \tag{B.4}$$

The corresponding boundary conditions for $G(y, y_0;\lambda)$ are that $G(y, y_0;\lambda)$ should be outgoing as $y\to-\infty$ and at $y\to\infty$.

B.1. Weber Functions

By introducing new variables

$$\eta = \lambda^{1/4}\sqrt{2\beta}y, \tag{B.5}$$

and

$$a = \left[\left(k^2+\beta\frac{k}{\omega}\right)\lambda^{-1/2}+\omega^2\lambda^{1/2}\right] = \frac{1}{2\beta\lambda^{1/2}}\left(k^2+\beta\frac{k}{\omega}+\lambda\omega^2\right), \tag{B.6}$$

the homogeneous form of equation (B.4) can be transformed into the standard (Whittaker's) form of the Weber equation

$$\frac{d^2G}{d\eta^2}+\left(\frac{1}{4}\eta^2-a\right)G = 0. \tag{B.7}$$

From Abramowitz and Stegun (1965), it can be shown that the complex forms of Weber function $E(a, \eta)$ and $E(a, -\eta)$ resulting from (B.7) satisfy the outgoing requirement at $y \to \infty$ and at $y \to -\infty$ (assuming that the time dependence is $e^{-i\omega t}$), respectively.

The solutions to equation (B.7) are discussed in detail by Miller in his mathematical introduction in a document on Weber parabolic cylinder functions prepared by National Physical Laboratory (1955). The calculation methods for these solutions can further be found in another document prepared by National Physical Laboratory (1960). Some properties of Weber parabolic cylinder functions $E(a, \eta)$ that are helpful to obtain the Green's function $G(y, y_0;\lambda)$ in equation (B.4) are the following:

B.1.1. The Integral Form of $E(a, \eta)$

The integral form of $E(a, \eta)$ is

$$E(a, x) = \sqrt{2} e^{\pi a/4 + i\pi/8 + i\phi_2/2} U(ia, xe^{-i\pi/4}), \tag{B.8}$$

where

$$\phi_2 = \arg\left[\Gamma\left(\frac{1}{2} + ia\right)\right], \tag{B.9}$$

and

$$U(a, z) = \frac{1}{\sqrt{2\pi i}} e^{z^2/4} \int_{\varepsilon} e^{-zs + s^2/2} s^{-a-1/2} ds. \tag{B.10}$$

In equation (A.10), the contour ε is shown in Fig. B.1

B.1.2. The Wronskian of $E(a, \eta)$ and Other Relations

The Wronskian of $E(a, \eta)$ is

$$\mathcal{W}\{E(a, \eta), E^*(a, \eta)\} = -2i, \tag{B.11}$$

where $E^*(a, \eta)$ is the complex conjugate of $E(a, \eta)$. The relationship between $E(a, \eta)$ and $E^*(a, \eta)$ is

$$\sqrt{1 + e^{2\pi a}} E^*(a, -x) = e^{\pi a} E(a, -x) - iE(a, x). \tag{B.12}$$

Then, from equations (B.11) and (B.12), one obtains

$$E(a, \eta)\frac{dE(a, -\eta)}{d\eta} - E(a, -\eta)\frac{dE(a, \eta)}{d\eta} = 2\sqrt{1 + e^{2\pi a}}. \tag{B.13}$$

B.2. The Green's Function

At $y = y_0$, the Green's function $G(y, y_0;\lambda)$ resulting from equation (B.4) should satisfy two requirements: 1) a derivative jump, i.e.,

$$\left.\frac{dG}{dy}\right|_{y_0^-}^{y_0^+} = -(\beta^2 y^2 - \omega^2), \tag{B.14}$$

and 2) the continuity, i.e.,

$$G(y_0^-, y_0;\lambda) = G(y_0^+, y_0;\lambda). \tag{B.15}$$

From equation (B.15), it is expected that the Green's function $G(y, y_0;\lambda)$ can be expressed as the following:

$$G(y, y_0;\lambda) = \begin{cases} AE(a, \eta_0)E(a, -\eta) \ for \ y < y_0 \\ AE(a, -\eta_0)E(a, \eta) \ for \ y > y_0 \end{cases}, \tag{B.16}$$

Where A is a constant to be determined. From equations (B.13), (B.14), (B.16), one obtains

$$A = \frac{-(\beta^2 y_0^2 - \omega^2)}{2\lambda^{1/4}\sqrt{2\beta}\sqrt{1+e^{2\pi a}}}. \tag{B.17}$$

Hence, the complete form of the Green's Function for the operator $(\mathcal{L} - \lambda)$ is

$$G(y, y_0;\lambda) = \begin{cases} \dfrac{-(\beta^2 y_0^2 - \omega^2)}{2\lambda^{1/4}\sqrt{2\beta}\sqrt{1+e^{2\pi a}}} E(a, \lambda^{1/4}\sqrt{2\beta}y_0)E(a, -\lambda^{1/4}\sqrt{2\beta}y) \ for \ y < y_0 \\ \dfrac{-(\beta^2 y_0^2 - \omega^2)}{2\lambda^{1/4}\sqrt{2\beta}\sqrt{1+e^{2\pi a}}} E(a, -\lambda^{1/4}\sqrt{2\beta}y_0)E(a, \lambda^{1/4}\sqrt{2\beta}y) \ for \ y > y_0 \end{cases}. \tag{B.18}$$

The Green's function $G(y, y_0;\lambda)$ is differentiable at $\omega = \pm\beta y$, hence, the $\omega = \pm\beta y$ are only artificial singular points.

B.3. Spectral Representation of $\mathcal{L}$ and the Eigenfunctions

From Appendix A, we know that the spectral representation of the operator $\mathcal{L}$ is expressed as:

$$-\delta(y-y_0) = \lim_{R\to\infty}\frac{1}{2\pi i}\oint_R G(y, y_0;\lambda)d\lambda. \tag{B.19}$$

Cauchy's theorem can then be used to deform this circle into a contour around the singularities of $G(y, y_0;\lambda)$. Note that $G(y, y_0;\lambda)$ has a branch-point singularity at $\lambda = 0$ and possible poles at $a = i(n + 1/2)$ with n any integer. Hence, one has

$$-\delta(z-\xi) = \frac{1}{2\pi i}\int_{ACB} G d\lambda = \frac{1}{2\pi i}\int_{ACBDA} G d\lambda - \frac{1}{2\pi i}\int_{BDA} G d\lambda, \tag{B.20}$$

where the contour integral is illustrated in Fig. B.2

From equation (B.10), it can be shown that when n is non-negative, $E(a, \eta)$ is zero since the RHS of equation (B.10) does not have a pole inside the integral contour. Hence, *the eigenvalues (λ's) resulting from equation (A.1) and its boundary conditions include continuous values along the whole positive real axis and an infinite number of discrete values corresponding to the poles at which $a = i(n + 1/2)$, with n being any negative integer.* Consequently, *the eigenfunctions include an infinite number of discrete modes and a spectrum of continuous modes.*

For any negative equivalent depth (λ>0) mode, the corresponding eigenfunction does not have any simple analytic form, but its asymptotic form can be obtained using the results in Abramowitz and Stegun (1965). These eigenfunctions are asymptotically decaying as $|y| \to \infty$. For these poles, it can be derived that the corresponding equivalent depths are positive and satisfy the equation

$$\frac{\sqrt{gh_m}}{\beta}\left(\frac{\omega^2}{gh_m}-k^2-\beta\frac{k}{\omega}\right) = 2m+1\,, \tag{B.21}$$

where m is a non-negative integer ($m = -(n+1)$ for any negative n).

Therefore, equation (B.14) can be further simplified to

$$\delta(y-y_0) = \lim_{R\to\infty}\frac{1}{2\pi i}\oint_{ACB} G(y, y_0;\lambda)d\lambda$$

$$= \sum_{n=0}^{\infty}\alpha_m(y_0)\psi_m(y) + \lim_{R\to\infty}\frac{1}{2\pi i}\oint_{BDA} G(y, y_0;\lambda)d\lambda\,, \tag{B.22}$$

where $\psi_m(y)$ are parabolic cylinder functions of order m, and α_m is the projection coefficient. The explicit form of the second term of the RHS of equation (B.22) is not yet clear.

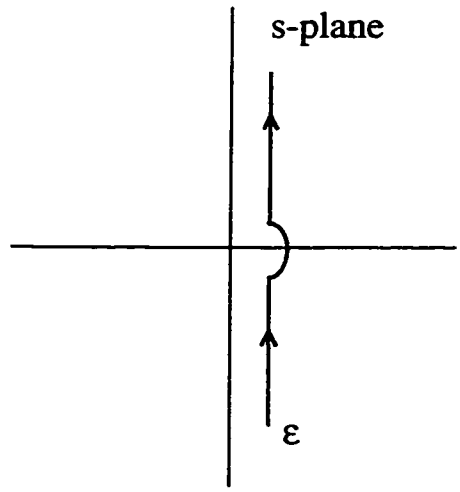

Figure B.1: The contour ε along which the integration (B.10) is performed.

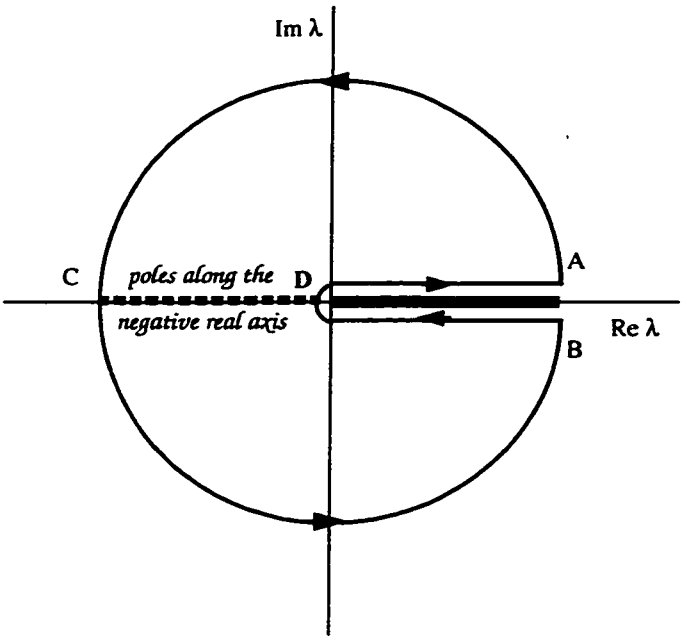

Figure B.2: The contour **C** in the complex λ-domain along which the Green's function **G** should be integrated. Since the Green's function **G** at positive real axis is multi-valued, a branch-cut is performed.

VITA

Zhaohua Wu was born on January 24, 1966 in Fenghua, Zhejiang, P. R. China. He attended Nanjing University in 1988 and graduated with a B. S. in Atmospheric Sciences. In the last year of his undergraduate study, he completed a research project on the surface radiation budget in the Northern Pacific under the guidance of Professor Guodong Gao. In 1988, he became a graduate student in the Institute of Atmospheric Physics, Chinese Academy of Sciences under the guidance of Professor Congbin Fu and worked on the chaotic behavior of climate variation. In 1991, he entered the graduate program at the Department of Atmospheric Sciences, University of Washington, working with Professors E. S. Sarachik and D. S. Battisti. He studied the interaction between monsoon and ENSO, the irregularity of ENSO, and the thermally forced surface winds in the tropics. The excellent training in mathematics and physics he received in his undergraduate and graduate studies made him a theoretician on the fundamental dynamics of the tropical atmosphere. After accomplishing his Ph. D. in 1998, he will pursue an academic career.

Publications:

Chen, X., G. Gao and Z. Wu, 1991: The long wave radiation budget in the atmosphere over the North Pacific. *Journal of Nanjing University (Natural Sciences Edition)*, **27**, 623-629.

Wu, Z., E. S. Sarachik, D. S. Battisti, 1997: Forced planetary waves on an equatorial beta-plane. *11th Conference on Atmospheric and Oceanic Fluid Dynamics*, American Meteorological Society, 6-10.

Wu, Z., E. S. Sarachik, D. S. Battisti, 1997: On the different roles of Rayleigh friction and Newtonian cooling in the linear response to steady tropical heating. Abstract, *1997 AGU Fall meeting*, **78**, A32B-5.

Wu, Z., D.S. Battisti, and E. S. Sarachik, 1998: Rayleigh friction, Newtonian cooling, and the linear response to steady tropical heating. *Journal of the Atmospheric Sciences*, (submitted).

Wu, Z., E. S. Sarachik, and D. S. Battisti, 1998: Vertical structure of convective heating and the three dimensional structure of the forced circulation in the tropics. *Journal of the Atmospheric Sciences*, (submitted).

Wu, Z., E. S. Sarachik, and D. S. Battisti, 1999: Thermally forced Surface winds on an equatorial beta-plane. *Journal of the atmospheric Sciences*, (in press).

Wu, Z., E. S. Sarachik, and D. S. Battisti, 1999: The Thermally forced tropical circulation under Rayleigh friction and Newtonian cooling: an analytical approach. *Journal of the Atmospheric Sciences*, (to be submitted).

IMAGE EVALUATION TEST TARGET (QA-3)

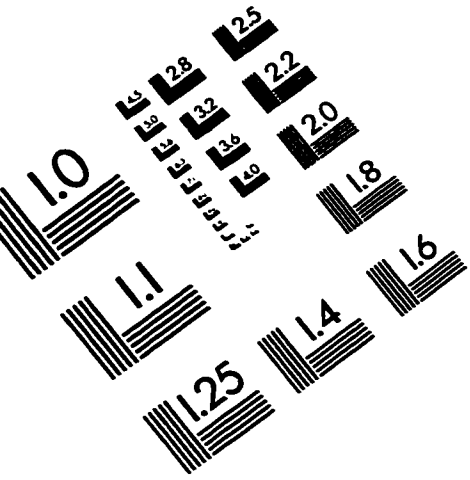

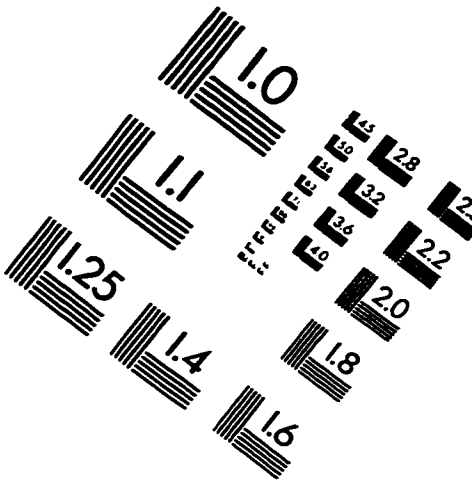

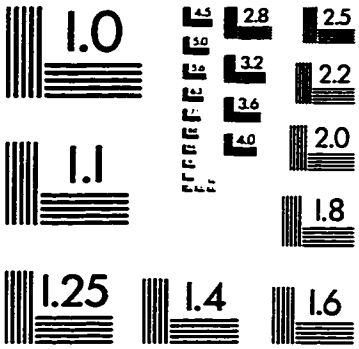

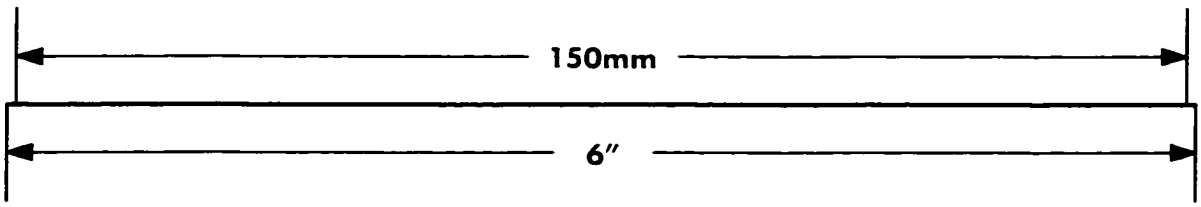

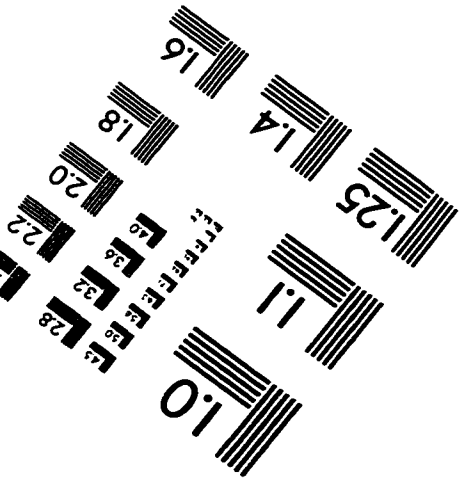

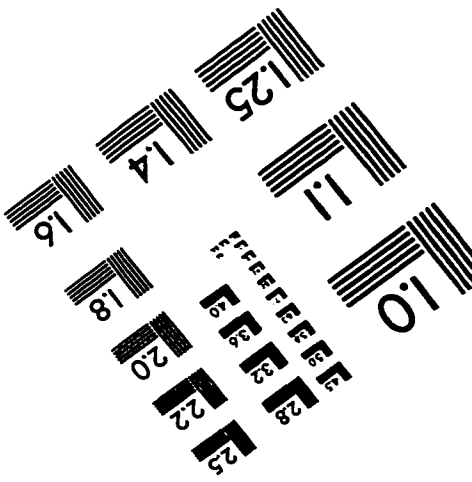

APPLIED IMAGE, Inc
1653 East Main Street
Rochester, NY 14609 USA
Phone: 716/482-0300
Fax: 716/288-5989